Geometry identification and data enhancement for distributed flow measurements

TECHNISCHE
UNIVERSITÄT
DARMSTADT

Vom Fachbereich Mathematik der Technischen Universität Darmstadt
zur Erlangung des Grades
Doktor rerum naturalium
(Dr. rer. nat.)

Dissertation
von
Tobias Seitz, M. Sc.

Erstgutachter: Prof. Dr. Herbert Egger
Zweitgutachter: Prof. Dr.-Ing. Cameron Tropea
Drittgutachter: Assoc. Prof. Hirofumi Notsu, PhD

Darmstadt 2017

Seitz, Tobias:
Geometry identification and data enhancement for distributed flow measurements
Darmstadt, Technische Universität Darmstadt

Jahr der Veröffentlichung der Dissertation auf TUprints: 2018
URN: urn:nbn:de:tuda-tuprints-72540
Tag der mündlichen Prüfung: 19.12.2017

CONTENTS

Acknowledgements

First of all, I would like to thank my supervisor Prof. Dr. Herbert Egger for his constant support. I very much appreciate his constant interest in my work and his direct and honest feedback on mathematical and non-mathematical subjects. His basically constant availability helped me finish this thesis and I am very thankful for that.

My second supervisor in Darmstadt was Prof. Dr. Cameron Tropea and I also want to thank him for the useful discussions we had, even though he usually has a very tight schedule. Talking to him really helped me understand some more practical aspects of fluid dynamics.

Third, I am grateful for the hospitality I experienced during my research stay at Waseda University in Tokyo. Here, I especially thank Prof. Dr. Hirofumi Notsu who shared his office with me and was always interested in my work and also my life as a foreigner in a country I had never visited before.

Last but not least, I want to thank all other people who supported me during this time, including my family, friends, and colleagues. At this point, in order to make mention of her personally, I also thank Lisa, even though she knows that she will always be the person I am most grateful to.

The experimental data used in part IV were provided by the Medical Physics group at the University Medical Center in Freiburg. I am also thankful for the enlightening discussions, where I learned a lot about medical imaging.

This work was supported by the German Research Foundation (DFG) via grants IRTG 1529, GSC 233, and Eg-331/1-1. Part of the work was carried out during a research stay at Waseda University, Tokyo. The hospitality and kind support of Waseda University is gratefully acknowledged.

1 Summary

The measurement of fluid motion is an important tool for researchers in fluid-dynamics. Measurements with increasing precision did expedite the development of fluid-dynamic models and their theoretical understanding. Several well-established experimental techniques provide point-wise information on the flow field, see e.g. [84]. In recent years novel measurement modalities have been investigated which deliver spatially resolved three-dimensional velocity measurements. Note that for methods such as particle tracking and tomographic particle imaging [46, 67] optical access to the flow domain is necessary. For other methods like magnetic resonance velocimetry, CT-angiography, or x-ray velocimetry [25, 28, 29] this is, however, not the case. Such a property and also the fact that those methods are able to provide three-dimensional velocity fields in a rather short acquisition time makes them in particular suited for in-vivo applications.

Our work is motivated by such non-invasive velocity measurement techniques for which no optical access to the interior of the geometry is needed and also not available in many cases. Here, an additional difficulty is that the exact flow geometry is in general not known a priori. The measurement techniques we are interested in, are extensions of already available medical imaging modalities. As a prototypical example, we consider magnetic resonance velocimetry, which is also suited for the measurement of turbulent fluid motion [26]. We will also discuss computational examples using such measurement data.

General purpose. Our main goal is a suitable post-processing of the available velocity data and also to obtain additional information. The measurements available from magnetic resonance velocimetry consist of several components given on a fixed *field of view*. The magnitude of the MRT signal corresponds to a proton density [12] and thus e.g. the density of water molecules. Those data typically give a clear indication of the position and size of the flow geometry. The velocity data, on the other hand, are substantially perturbed outside the flow domain. This is a typical feature of measurements stemming from magnetic resonance velocimetry [12]. Note that the surrounding noise usually has a notably higher magnitude than the actual measurements.

Thus, a first necessary step will be to somehow separate the domain containing valuable velocity data from the noise surrounding it. For this reason, we apply some kind of image segmentation where we make use of the given den-

sity image. Since the velocity values are given on the same field of view the segmentation directly transfers to those data.

Due to the measurement procedure also the segmented velocity data are contaminated by measurement errors. Therefore, besides segmentation, additional post-processing is necessary in order to make the flow measurements available for further usage [59]. In a second step, we propose a problem adapted data enhancement method which is able to provide a smoothed velocity field on the one hand, and also provides additional information on the other hand, like for instance the pressure drop or an estimate for the wall shear stress.

The two main steps will therefore be:

(i) The identification of the flow geometry, where we make use of the available density measurements.

(ii) The denoising and improvement of the segmented velocity data, by using a suitable fluid-dynamical model.

Outline. In part I of this thesis, we introduce our basic approach to the geometry identification and velocity enhancement problems described above. Both problems are formulated as optimal control problems governed by a partial differential equation and we shortly discuss some general aspects of the analysis and the solution of such problems in section 4.

In part II, we thoroughly discuss and analyze the geometry identification problem introduced in section 2. The procedure is formulated as an inverse ill-posed problem and we propose a *Tikhonov regularization* [82] for its stable solution. We show that the resulting optimal control problem has a solution and discuss its numerical treatment with iterative methods. Finally, a systematic discretization can be realized using finite elements, see e.g. [10], which is also demonstrated by numerical tests.

The velocity enhancement problem is introduced in part III. We propose a linearized flow-model which directly incorporates the available measurements. The resulting *modeling error* can be quantified in terms of the *data error*. The reconstruction method is then formulated as an optimal control problem subject to the linearized equations. We show the existence of a unique solution and derive estimates for the reconstruction error. Additionally, a reconstruction for the pressure is obtained for which we derive similar error estimates. We dis-

cuss the systematic discretization using finite elements and show preliminary computational examples for the verification of the derived estimates.

In order to verify the applicability of the proposed methods to realistic data, we consider an application using experimental data in part IV. We use measurements of a human blood vessel stemming from magnetic resonance velocimetry obtained at the University Medical Center in Freiburg. After a suitable pre-processing of the available data, we apply the geometry identification method in order to obtain a discretization of the blood vessel. Using the generated mesh, we reconstruct an enhanced velocity field and the pressure from the available velocity data.

Zusammenfassung in deutscher Sprache

Messungen von Strömungsgeschwindigkeiten sind ein wichtiger Aspekt bei der Untersuchung strömungsmechanischer Vorgänge. Messmethoden mit zunehmender Genauigkeit haben die Entwicklung und das theoretische Verständnis fluiddynamischer Modelle deutlich voran getrieben. Gängige Techniken messen Strömungsgeschwindigkeiten an ausgewählten Punkten im Strömungsfeld, siehe z.B. [84]. In den letzten Jahren wurden neuartige Messmethoden untersucht, die in der Lage sind, räumlich aufgelöste, dreidimensionale Geschwindigkeitsfelder zu messen. Methoden wie *Einzelpartikelverfolgung* oder *Schichtaufnahmen* [46, 67] benötigen dafür einen optischen Zugang zum Messgebiet. Andere Methoden wie *Magnetresonanz Velocimetry*, *CT-Angiographie* oder *Röntgen Velocimetry* [25, 28, 29] brauchen keinen solchen Zugang. Diese Eigenschaft und auch die Tatsache, dass dreidimensionale Geschwindigkeitsfelder in vergleichsweise kurzer Zeit gemessen werden können, machen solche Messverfahren besonders geeignet für Anwendungen im lebenden Organismus.

Wir interessieren uns hier insbesondere für nicht invasive Messtechniken, die keinen optischen Zugang zum Inneren der Geometrie benötigen. Dieser ist in Anwendungen oft nicht verfügbar und die exakte Strömungsgeometrie im Allgemeinen nicht bekannt. Wir betrachten daher spezielle Messtechniken, die von bereits verfügbaren medizinischen Bildgebungsverfahren abgeleitet werden. Als Beispiel nutzen wir hier die *Magnetresonanz Velocimetry*, die sich insbesondere auch für die Messung von turbulenten Strömungen eignet [26]. Wir diskutieren außerdem ein Anwendungsbeispiel für solche Messdaten.

Motivation. Generell sollen die verfügbaren Geschwindigkeitsdaten mit angepassten Methoden nachbearbeitet und zusätzliche Informationen daraus gewonnen werden. Die von der *Magnetresonanz Velocimetry* verfügbaren Messdaten bestehen aus mehreren Komponenten in einem fixierten Bildausschnitt. Die Magnitude des MRT Signals entspricht der Protonendichte [12], und korreliert damit auch mit beispielsweise der Dichte von Wassermolekülen. Typischerweise geben diese Daten eine klare Vorstellung von der Größe und Position der Strömungsgeometrie. Andererseits sind die Geschwindigkeitsdaten außerhalb der Strömungsgeometrie stark verrauscht, wobei die Ungenauigkeit hier typischerweise deutlich größer als das Signal der relevanten Messung ist. Solche Artefakte sind typisch für Daten die mit *Magnetresonanz Velocimetry* erstellt wurden [12].

Der erste Schritt in der Datenverarbeitung ist also, den Bereich, in dem nutzbare Geschwindigkeitsdaten vorhanden sind, von dem Rauschen in der Umgebung zu trennen. Deshalb verwenden wir eine Bildsegmentierung und nutzen dabei die verfügbaren Dichtemessungen. Da alle Komponenten auf demselben Bildausschnitt gegeben sind, kann die Segmentierung direkt auf die Geschwindigkeitsdaten übertragen werden.

Aufgrund des Messvorgangs sind auch die segmentierten Geschwindigkeitsdaten mit Messfehlern versetzt. Deshalb muss neben der Segmentierung noch ein weiteres Verfahren zur Nachbearbeitung der Daten eingesetzt werden. Das ist insbesondere nötig, um die Messdaten für eine weitere Verwendung nutzbar zu machen [59]. Als zweiten Schritt schlagen wir deshalb eine an das Problem angepasste Datenverbesserung vor, die einerseits in der Lage ist, ein verbessertes Geschwindigkeitsfeld zu berechnen, aber auch weitere Informationen, wie zum Beispiel den Druckverlust, zu rekonstruieren.

Wir unterscheiden zwei wichtige Schritte:

(i) Die Identifizierung der Strömungsgeometrie, wobei die verfügbaren Messdaten der Protonendichte verwendet werden.

(ii) Die Aufbereitung und Verbesserung der segmentierten Geschwindigkeitsdaten mit Hilfe strömungsmechanischer Modelle.

Überblick. In Teil I dieser Arbeit werden wir unser grundsätzliches Vorgehen für die Identifizierung der Geometrie und die Aufbereitung der Geschwindigkeitsdaten diskutieren. Beide Probleme werden als optimale Steuerungsprobleme formuliert und wir gehen in Abschnitt 4 auf die allgemeine Behandlung solcher Probleme ein.

In Teil II wird eine Methode zur Identifizierung der Geometrie vorgestellt und analysiert. Wir nutzen eine Formulierung als (schlecht gestelltes) inverses Problem und eine *Tikhonov Regularisierung* [82], um auf stabile Art eine Lösung zu berechnen. Wir zeigen, dass das entstehende optimale Steuerungsproblem eine Lösung hat und besprechen die numerische Lösung mit Hilfe iterativer Verfahren. Zuletzt wird die systematische Diskretisierung mit Finiten Elementen besprochen, und anhand numerischer Beispiele illustriert.

In Teil III diskutieren wir die Nachbearbeitung der Geschwindigkeitsdaten. Wir schlagen dazu ein lineares Strömungsmodell vor, welches direkt die verfügbaren Messungen verwendet. Der daraus resultierende Modellfehler kann

durch den Datenfehler abgeschätzt werden. Die Geschwindigkeitsrekonstruktion kann dann wieder als optimales Steuerungsproblem formuliert werden, wobei die linearisierten Gleichungen als Nebenbedingung auftreten. Wir zeigen, dass das Optimierungsproblem eine eindeutige Lösung besitzt und leiten Fehlerabschätzungen für den Rekonstruktionsfehler her. Des Weiteren erhalten wir eine Rekonstruktion des Drucks, für den wir vergleichbare Fehlerabschätzungen herleiten. Im Anschluss diskutieren wir die systematische Diskretisierung mithilfe von Finiten Elementen und zeigen erste numerische Beispiele für die Verifikation der Fehlerabschätzungen.

Um die Anwendbarkeit unserer Methoden auf realistische Daten zu illustrieren, betrachten wir in Teil IV ein Beispiel mit experimentellen Daten. Wir verwenden hier Messungen einer menschlichen Ader, die mit Hilfe von *Magnetresonanz Velocimetry* am Universitätsklinikum in Freiburg erstellt wurden. Nach entsprechender Vorbereitung der Daten wenden wir die Methode zur Identifizierung der Geometrie an und erhalten eine Diskretisierung der Ader. Das so generierte Gitter nutzen wir, um sowohl ein verbessertes Geschwindigkeitsfeld, als auch den Druck aus den vorhandenen Geschwindigkeitsdaten zu berechnen.

I Introduction and preliminaries

In part I of this thesis, we give an overview of the main problems and applications considered here. Our main interest lies in the appropriate processing of flow measurements stemming from magnetic resonance velocimetry. In order to do so, we will discuss two important steps.

The available data, including the usual MRT signal and the three components of the velocity vector, are given in a usually rectangular field of view. However, the domain of interest is often considerably smaller and completely contained in this field of view. This makes a segmentation necessary and, as a first step, we discuss the identification of the flow geometry in section 2. We use here a formulation which directly incorporates the available MRT density image.

Once the domain of interest is identified, we discuss the appropriate treatment of the flow measurements. Since all available data are given on the same field of view, we may directly use the geometry computed in the first step. We discuss the enhancement of the velocity data using a suitable flow model in section 3, where we use the available data for a linearization.

As we will see below, both problems discussed here can be formulated as optimal control problems governed by partial differential equations. We discuss our general approach for the solution of the resulting problems in section 4.

2 Geometry identification

Let us start with the description of the geometry identification problem. On the left side of Figure 1.1, we show a two-dimensional cross-section of a straight pipe. The measurements obtained with magnetic resonance velocimetry correspond to the density of the water in the pipe and the surrounding air. Such data give a clear indication of the position and size of the pipe, however, the region of interest itself has to be separated in some sense. For that purpose, we may employ an *image segmentation* or *shape identification* technique. For a further processing of the corresponding velocity data, the identified geometry should be available as some kind of numerical grid representing the flow domain after this pre-processing step, like shown on the right side of Figure 1.1.

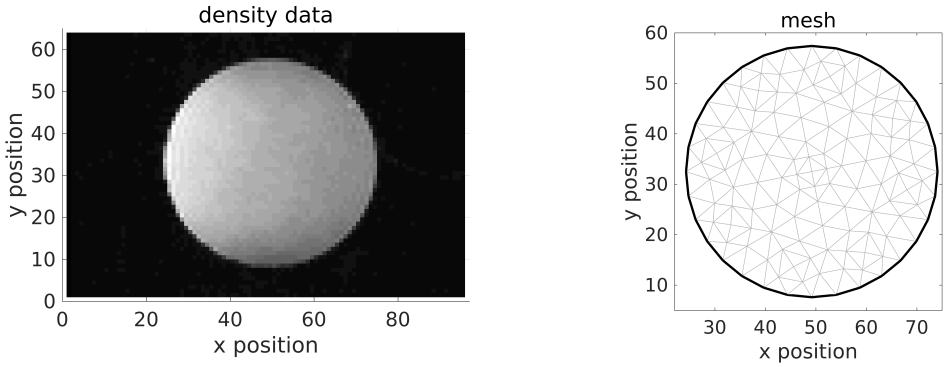

Figure 1.1 The MRT signal of water and the surrounding air in a cross-section of a straight pipe on the left. The segmented geometry with a triangular mesh is shown on the right.

The processing of such image data has been a very active field of research for many years. Several problems are studied in the literature including *image segmentation* and *image registration*, see e.g. [38, 69]. Such problems can also be formulated in the context of *shape identification*, see e.g. [14].

If we keep in mind that the identified geometry shall be used later on for the processing of velocity data, different aspects become important. Here, we will for instance require that a smooth representation is obtained, together with a numerical grid representing the identified domain. Therefore, we propose a method which not only allows to identify the geometry, but at the same time to generate a mesh on the flow region utilizing the available density data. Since the density data are provided by the same imaging modality as the velocity measurements, the corresponding velocity data can directly be used for further computations. Our method will be formulated as an optimal control problem governed by a partial differential equation and its numerical solution can be performed and evaluated by well-established techniques, see e.g. [51, 83, 47].

As a first observation, let us note that for measurements of interest here, see e.g. in Figure 1.1, the flow domain is usually occupied by material of constant density, which is the fluid under investigation. Consequently, after some scaling or using a "cut-off" function, the available density data correspond to an indicator function of the domain of interest. The appropriate processing of such data will serve as a guideline for the design of a shape identification method. Let us denote the a priori unknown geometry by $\Omega \subset \mathbb{R}^d$ with $d = 2$ or $d = 3$. We utilize a suitable parametrization of Ω, where the domain is represented by a function. Note that a description using directly admissible domains is sometimes

employed for instance in shape optimization [76]. Further, an implicit domain representation is realized using a *level-set* function in many cases [75].

Problem formulation. To keep our problem as simple as possible, we utilize an approach which is known as *method of mapping* in shape optimization [68]. Instead of computing Ω directly, we use a reference domain Ω^{ref} and compute a smooth and bijective transformation ϕ such that

$$\phi(\Omega^{\text{ref}}) = \Omega,$$

as illustrated in Figure 1.2.

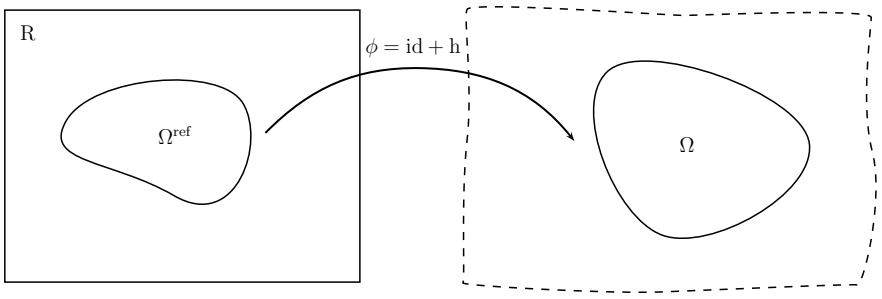

Figure 1.2 The transformation $\phi = \mathrm{id} + \mathrm{h}$ transforms a given reference frame R. We aim to find h such that $\phi(\Omega^{\text{ref}}) = \Omega$.

We will require in the following that enough a priori information on the flow domain are available. Further, we settle the relation

$$\phi = \mathrm{id} + \mathrm{h},$$

where id denotes the identity operator and h a (presumably small) deformation, c.f. Figure 1.2. Note that, due to measurement errors, we have only given approximate information on Ω.

As mentioned before, after some pre-processing, the available data correspond to an approximate indicator function χ_Ω^δ of the domain Ω; see Figure 1.1. The corresponding domain identification problem can then be formulated as follows. Find an admissible deformation $\mathrm{h} \in \mathcal{H}_{\text{ad}}$ such that

$$\chi_\Omega^\delta \circ (\mathrm{id} + \mathrm{h}) = \chi_{\Omega^{\text{ref}}}. \tag{2.1}$$

Unfortunately, the difference of the indicator functions does not yield a suitable measure for the distance of two domains. For such a choice of the distance, small deformations h would not change the value if both domains are e.g. completely disjoint or included in each other.

Remark 2.1. Here, our main interest is to obtain a suitable transformation ϕ and hence, a representation of Ω. The underlying shape identification problem is trivial in the sense that we observe Ω directly with measurements χ_Ω^δ. Even if the transformation $\phi = \mathrm{id} + \mathrm{h}$ is a bijective diffeomorphism the transformed data $\chi_\Omega^\delta \circ (\mathrm{id} + \mathrm{h})$ will not be an indicator function in general. Therefore, problem (2.1) does in general not admit a solution for any given domain Ω^{ref}. Clearly, the uniqueness of a solution cannot be expected since any transformation mapping Ω^{ref} to itself may be applied additionally to ϕ without changing the result.

The formulation using a reference domain has several advantages:

- The transformation ϕ will be a function stemming from a Hilbert space, and is thus easier to handle mathematically than a domain.
- Constraints on admissible deformations h can be directly incorporated to enforce certain properties of the identified domain.
- Additional information, like e.g. a triangulation on the reference domain Ω^{ref}, can then be directly transfered to the identified domain Ω.
- Available a priori information on the shape, size, and topology of Ω can be incorporated in the construction of Ω^{ref}. Typically, this is the case in engineering applications where the experimental setup is known.

Note that also for in-vivo applications the shape of e.g. a blood vessel can be roughly specified by the user. Such an initial configuration may for instance be provided by using certain image registration techniques, see e.g. [42, 64]. For shapes like blood vessels, it is possible to identify a three-dimensional geometry by treating a series of two-dimensional problems for cross-sections of the domain, c.f. section 13 of part IV.

Choice of a distance measure. The second ingredient we need for our reconstruction method is a suitable measure for the distance of two domains. The main idea in our approach is not to compare the indicator functions directly but rather some derived quantity, i.e. some kind of potential. If the data are for in-

stance interpreted as mass density of homogeneous bodies, we may compute the gravitational potential of the corresponding bodies. The difference of the resulting potentials can serve as a distance which is zero if and only if both domains match, see Lemma 2.2. For the convenient computation of the potentials, we introduce a reference frame R with Ω^{ref} compactly contained in it, see Figure 1.2. The complete problem can then be formulated on R which makes the method flexible.

Let us first define a reference potential p^{ref} corresponding to the reference domain Ω^{ref} as the unique solution of

$$-\Delta \mathrm{p}^{\text{ref}} + \mathrm{p}^{\text{ref}} = \chi_{\Omega^{\text{ref}}} \quad \text{in R}, \tag{2.2a}$$

$$\partial_n \mathrm{p}^{\text{ref}} = 0 \qquad \text{on } \partial\mathrm{R}, \tag{2.2b}$$

where homogeneous Neumann boundary conditions are employed for simplicity. Since we utilize an artificial potential, we do not need to take care about physical relevant constants or units. Note that other differential operators could be chosen as well. This particular choice will simplify our presentation later on.

The potential $\mathrm{p} = \mathrm{p}[\mathrm{h}]$ corresponding to the shifted indicator function $\chi_\Omega^\delta \circ (\mathrm{id} + \mathrm{h})$ will be defined as the solution of

$$-\Delta \mathrm{p} + \mathrm{p} = \chi_\Omega^\delta \circ (\mathrm{id} + \mathrm{h}) \quad \text{in R}, \tag{2.3a}$$

$$\partial_n \mathrm{p} = 0 \qquad \text{on } \partial\mathrm{R}. \tag{2.3b}$$

The support of the potentials p and p^{ref} is the complete reference domain R which makes their difference

$$\|\mathrm{p} - \mathrm{p}^{\text{ref}}\|$$

a suitable measure for the deviation of the corresponding domains, which will be zero if and only if the shifted reference domain and Ω have the same shape, i.e. if $\phi(\Omega^{\text{ref}}) = \Omega$ and χ_Ω^δ is indeed an indicator function of the domain Ω.

Lemma 2.2. *Let* p^{ref} *and* p *denote the solution of* (2.2a)–(2.2b) *and* (2.3a)–(2.3b) *respectively. Then* $\|\mathrm{p} - \mathrm{p}^{\text{ref}}\| = 0$ *if and only if* $\chi_\Omega^\delta \circ (\mathrm{id} + \mathrm{h}) = \chi_{\Omega^{\text{ref}}}$.

This is a simple consequence of the following Lemma.

Lemma. *Let* $\Omega_1, \Omega_2 \subset \mathrm{R}$ *be measurable subsets of* R. *Let* p_1 *and* p_2 *be the solution of* (2.2a)–(2.2b) *with the right-hand side substituted by* χ_{Ω_1} *or* χ_{Ω_2}, *respectively, and let* Z *denote a set of measure zero. Then, we have* $\mathrm{p}_1 = \mathrm{p}_2$ *if and only if*

$$\Omega_1 = \Omega_2 \cup Z.$$

Proof. Due to the linearity of (2.2a) the difference $\mathrm{p}_1 - \mathrm{p}_2$ is zero if and only if the right-hand size is zero almost everywhere. □

Formulation as inverse problem. We use the corresponding potentials as measure for comparison. Then, problem (2.1) can be reformulated as follows. For a given set $\mathcal{H}_{\mathrm{ad}}$ of admissible deformations, find $\mathrm{h} \in \mathcal{H}_{\mathrm{ad}}$, such that

$$\mathrm{F}(\mathrm{h}) = \mathrm{p}^{\mathrm{ref}},$$

where $\mathrm{F}(\mathrm{h}) = \mathrm{p}[\mathrm{h}]$ is the solution of (2.3a)–(2.3b).

Remark. Note that the dependence on the noisy data χ_Ω^δ is hidden in the definition of the operator F. This is somewhat non-standard and due to the fact that we choose a formulation on R. A reformulation of the problem in the physical domain would reveal the "noisy potential" on the right-hand side.

As we will see below, the solution h does not depend continuously on the data χ_Ω^δ in general. From this aspect and Remark 2.1, we conclude that problem (2.1) is not well-posed in the sense of Hadamard [41], i.e. at least one of the following conditions for well-posedness is not fulfilled:

- A solution exists for all admissible data.
- The solution is unique.
- The solution depends continuously on the data.

Therefore, a regularization is necessary for a stable solution and we use here *Tikhonov regularization* [82] to determine an approximate solution h of (2.1) by solving a minimization problem of the form

$$\min_{\mathrm{h} \in \mathcal{H}_{\mathrm{ad}}} \|\mathrm{F}(\mathrm{h}) - \mathrm{p}^{\mathrm{ref}}\|_*^2 + \alpha \|\mathrm{h}\|_+^2, \tag{2.4}$$

where $\alpha > 0$ is a regularization parameter. The set $\mathcal{H}_{\text{ad}}$ and the norms $\|\cdot\|_*$ and $\|\cdot\|_+$ have to be defined appropriately to yield a complete description of the problem.

Since $F(h)$ is defined implicitly via the solution of a partial differential equation, the regularized problem can also be written equivalently in the form of an optimal control problem governed by a partial differential equation, i.e.

$$\min_{(h,p)\in\mathcal{H}_{\text{ad}}\times V} \|p - p^{\text{ref}}\|_*^2 + \alpha\|h\|_+^2,$$
$$\text{s.t. (2.3a)} - \text{(2.3b)},$$

for some suitable function space V for the solution of (2.3a)–(2.3b). As we will show below, this problem admits a solution. However, due to the nonlinearity of the forward operator F, the solution will in general not be unique.

The identified domain will then be given as $\Omega_\alpha = \phi_\alpha(\Omega^{\text{ref}})$, where $\phi_\alpha = \text{id} + h_\alpha$ and h_α denotes a minimizer of (2.4).

Related problems. The unknown deformation h in the approach (2.4) corresponds to a transformation of the domain of interest. This problem fits into the framework of *shape optimization*. The particular formulation we use here amounts to the *method of mapping* [68]. Similar problems, where the support of the right-hand side of a partial differential equation was identified, have been studied for elliptic and parabolic equations in [48, 49, 58, 70]. In these works, the change of the solution of the partial differential equation with respect to the support of the right-hand side is given in terms of the *domain derivative*. We will comment on this perspective in more detail in section 5.3.

Outline of part II. A detailed discussion of the proposed domain identification method is given in part II. We will analyze the forward operator F in more detail and establish some important properties which are needed for the analysis of the Tikhonov regularization. This will especially enable us to show that problem (2.4) has a solution, and we derive the corresponding optimality conditions. We will also present some numerical tests to additionally verify the performance of our method. To demonstrate the viability of the method also for real-life applications, we discuss an example with data stemming from magnetic resonance velocimetry in section 13 of part IV.

3 Velocity enhancement

The flow measurement modalities discussed here are, in principle, capable to provide valuable information on fluid velocities. Further, non-invasive measurement techniques like magnetic resonance velocimetry can also be applied to complex flow geometries.

In this section, we assume that measurements of the full velocity field are available in the domain of interest. Such a domain can be available from the identification procedure described in section 2 or from a given experimental setup as shown for instance in Figure 1.3.

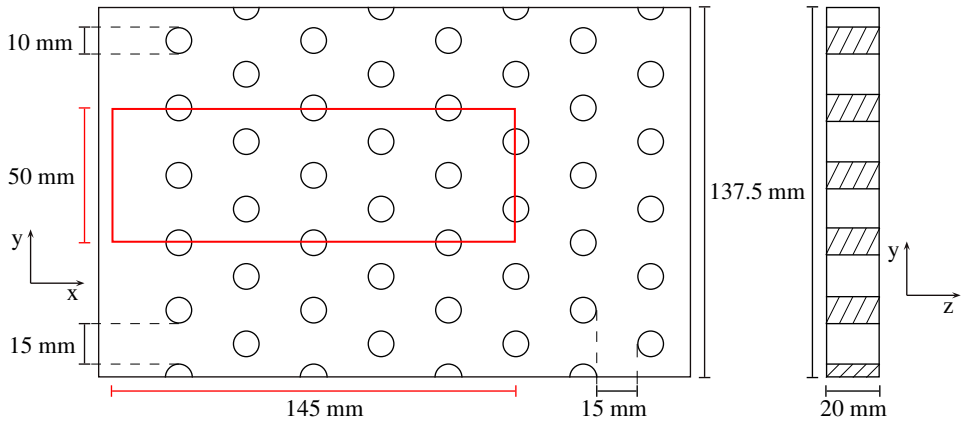

Figure 1.3 Geometry of a pinfin array; see also [87, 24]. Here the domain of interest is depicted as a red rectangle.

However, such data are typically contaminated by distributed measurement errors. This limits their usability to some extent and we discuss here a possible method to use such noisy data to compute an improved approximation of the velocity. These enhanced velocity data can then be used for the analysis of the flow, e.g. for model calibration or for the assessment of physically relevant derived quantities like pressure drop or wall shear stress [85, 22].

For illustration, we show in Figure 1.4 the velocity component in x-direction corresponding to the geometry shown in Figure 1.3. Note that despite the strong noise present in the velocity data, the main flow features, like for instance the stagnation and recirculation zones before and behind the obstacles, are nevertheless present. This motivates us to use some kind of denoising or filtering of the data, see e.g. [55, 72].

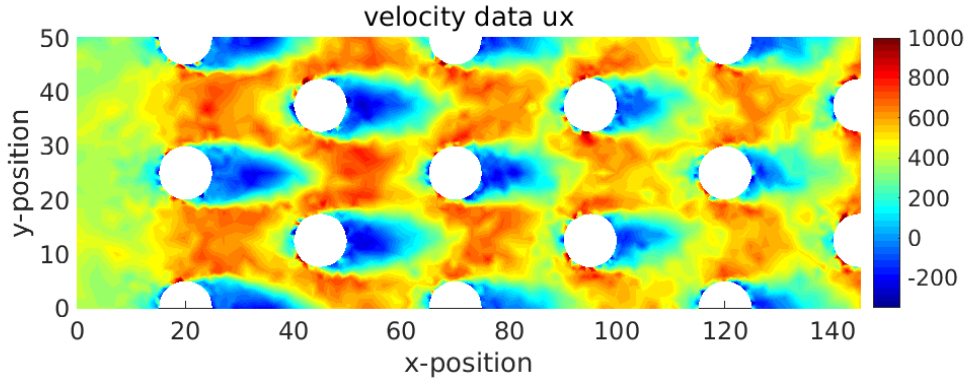

Figure 1.4 Raw velocity data of a flow through a pinfin array [87] as depicted in Figure 1.3; see also [24]. Here a two-dimensional slice of the downstream velocity component is shown. Note that three-dimensional velocity data are available on a volume here.

Following closely the presentation in [24], we now discuss a method which computes in a systematic way an enhanced velocity field from available distributed flow measurements. Since we use a prescribed flow model for the reconstruction, such a method additionally provides a pressure field.

In order to derive a velocity enhancement problem as described above, let us briefly introduce some particular data enhancement procedures. We assume that the flow geometry Ω is known, see section 2, and the noisy flow velocity data u^δ are available in this domain.

Data smoothing. A simple approach to enhance the velocity field is *data smoothing* which can be formulated, for instance, by *Tikhonov regularization*

$$\min_{u \in H^1(\Omega)} \|u - u^\delta\|^2 + \alpha \|\nabla u\|^2. \tag{3.1}$$

For the simple choice of the gradient in the regularization term, problem (3.1) is a quadratic minimization problem. Its minimizer, which corresponds to a smoothed velocity field, is characterized by the elliptic differential equation

$$\begin{aligned} -\alpha \Delta u + u &= u^\delta \quad \text{in } \Omega, \\ \partial_n u &= 0 \quad \text{on } \partial\Omega. \end{aligned}$$

This problem can be solved numerically e.g. by using finite elements [10]. Let us note that the regularization parameter α can be chosen in order to balance the "smoothness" of the reconstructed velocity against the reduction of the

residual $\|u - u^\delta\|$, i.e. the fit to the data. Such kind of filtering methods are well-known in the context of image processing [73].

A major drawback of such methods is, however, that no additional information on the available data are used. Especially in the context of fluid-dynamics, it is possible to incorporate such knowledge about e.g. the underlying physics into the reconstruction. A formulation of the image reconstruction as optimal control problem allows us to incorporate additional a priori information systematically via constraints.

Solenoidal filtering. In many applications, incompressible fluids are used for the experimental setup. In order to make use of this information, we incorporate a corresponding constraint in the smoothing procedure above. The result will be a constrained minimization problem of the form

$$\min_{u \in H^1(\Omega)} \|u - u^\delta\|^2 + \alpha \|\nabla u\|^2 \tag{3.2a}$$

$$\text{s.t. } \nabla \cdot u = 0 \quad \text{in } \Omega. \tag{3.2b}$$

The minimizer of this quadratic optimization problem can, similar as before, be characterized by a saddle-point problem of the form

$$-\alpha \Delta u + u + \nabla p = u^\delta \quad \text{in } \Omega, \tag{3.3a}$$

$$\nabla \cdot u = 0 \quad \text{in } \Omega, \tag{3.3b}$$

$$n \cdot (\nabla u - pI) = 0 \quad \text{on } \partial\Omega, \tag{3.3c}$$

where p denotes the Lagrange multiplier for the divergence constraint (3.2b) here. A solution of problem (3.2a)–(3.2b) or problem (3.3a)–(3.3c) respectively can for instance be computed using finite elements for saddle-point problems, see e.g. [8, 37]. We note that p does not approximate the physical pressure in this case which is also demonstrated by our numerical tests.

Let us note that related reconstruction approaches are available in the literature. Under the name *solenoidal* or *divergence free* filtering several such computational strategies have been investigated [13, 20, 61, 62, 74, 66, 86]. Note that in some cases an additional smoothing as in (3.2a)–(3.2b) is not employed. In this case, i.e. $\alpha = 0$, we may not expect the reconstruction to be smooth in general.

Fluid-dynamically consistent filtering. In a similar procedure as above, we now incorporate further a priori information in the reconstruction approach. While the incompressibility condition is derived from a mass balance, we would like to utilize also another fundamental law of fluid-dynamics, i.e. a momentum balance, for the reconstruction. Since the measurement procedure takes some time, the data u^δ amount to a time averaged velocity field, and we consider the stationary Navier-Stokes equations as a prototype. Thus, we assume steady flow conditions and the resulting data enhancement procedure can then, for instance, be formulated as the constrained optimal control problem

$$\min_{(u,f,g)\in V} \|u - u^\delta\|^2 + \alpha\Big(\|f\|^2 + |g - g^*|^2\Big) \tag{3.4a}$$

$$\text{s.t. } -\nu\Delta u + u\cdot\nabla u + \nabla p = f \qquad \text{in } \Omega, \tag{3.4b}$$

$$\nabla\cdot u = 0 \qquad \text{in } \Omega, \tag{3.4c}$$

$$u = g \qquad \text{on } \partial\Omega, \tag{3.4d}$$

where $\nu > 0$ denotes a viscosity parameter which is assumed to be constant, $V = H^1(\Omega)\times L^2(\Omega)\times H^1(\partial\Omega)$, and p the pressure which appears as additional variable. The penalization of the gradient of u is not necessary here. Instead, the residual f and the deviation from prescribed boundary conditions g^* is penalized. These terms ensure the smoothness of the reconstruction here, due to the differential terms in (3.4b).

Due to the nonlinearity in the momentum equation (3.4b), the analysis and the numerical solution of the system (3.4a)–(3.4d) is a challenging task. First, the stationary Navier-Stokes equations admit a unique solution only for sufficiently small data [34, 80]. Second, the problem is non-convex and may therefore have several local minima. Further, it is well-known that for a numerical solution the number of necessary grid points grows with the Reynolds number if all scales need to be resolved [32, 81] which is especially important for turbulent flows.

System (3.4a)–(3.4d) has the form of an optimal control problem governed by the Navier-Stokes equations. Such problems have been studied extensively and we refer to e.g. [21, 39, 47, 52] for steady and [1, 31, 36, 40, 50] for unsteady flow conditions. Problem (3.4a)–(3.4d) can also be interpreted as a regularization of an inverse source problem for the stationary Navier-Stokes equations [17], i.e. to find f and g such that the solution of (3.4b)–(3.4d) matches u^δ.

Linearization strategy. To overcome the technical problems of the previous formulation, the main idea here is to use a linear flow model as approximation for the stationary Navier-Stokes equations (3.4b)–(3.4d). We use the available distributed velocity measurements to linearize the nonlinear convective term $u \cdot \nabla u$ which then results in an optimal control problem of the form

$$\min_{(u,f,g)\in V} \|u - u^\delta\|^2 + \alpha\Big(\|f\|^2 + |g - g^*|^2\Big) \tag{3.5a}$$

$$\text{s.t. } -\nu\Delta u + u^\delta \cdot \nabla u + \nabla p = f \qquad \text{in } \Omega, \tag{3.5b}$$

$$\nabla \cdot u = 0 \qquad \text{in } \Omega, \tag{3.5c}$$

$$u = g \qquad \text{on } \partial\Omega. \tag{3.5d}$$

Let us note here that the choice $u^\delta \cdot \nabla u$ for the linearization does in general not yield a well-posed problem. This is due to the fact that the measurements are in general neither smooth nor divergence free. Therefore, we discuss a linearization strategy suited for non-smooth data in part III. The result will be a linear quadratic optimal control problem with a unique minimizer which can be solved efficiently. Note that the usage of measurements in the governing equations here is closely related to the *equation error* method [3, 43].

The proposed data filter can be interpreted as follows. From a momentum balance for incompressible fluids, we can assume that the true velocity field satisfies an equation of the form (3.4b), however, the residual f may contain several terms corresponding to unmodeled effects like e.g. time-dependence or some non-Newtonian behavior. As a consequence, the penalization of f is reasonable if the flow model describes the underlying flow suitably well. We will investigate the influence of this *modeling error* in more detail below.

Due to the flow model present in (3.5a)–(3.5d), which is automatically fulfilled by the reconstruction, we call such an approach a *fluid-dynamically consistent* filter. The additional benefit here is that additional information on the pressure is obtained automatically. Such a filtering approach may be interpreted as a calibration of the flow model to measurements, which is known as *data assimilation*, see e.g. [45] for an overview in the context of fluid dynamics.

Outline of part III. In part III, we will discuss and thoroughly analyze a similar linearization approach as discussed above to overcome the technical problems of the nonlinear formulation. Our ansatz maintains the main features of the described problem but with better analytical and computational properties. We will show that the resulting linear quadratic optimal control problem has a unique minimizer.

Further, the linearization procedure introduces an additional error which is of the same size as the measurement error. Using such an estimate, we will show that the reconstructed velocity and pressure fields approximate the real flow conditions except for modeling and measurement errors. The systematic discretization of the discussed filters using a finite element method is introduced and all theoretical results will be verified by numerical tests. To verify the applicability of our approach, we show results for the application to experimental data given by magnetic resonance velocimetry in section 14 of part IV.

4 General methodology

Before we proceed to a detailed description of the shape identification and the flow reconstruction problem outlined in the previous sections, let us comment on our general approach towards their solution. All proposed methods are given in form of *PDE-constrained optimization* problems. The theoretical and numerical treatment of such problems is well-understood, see e.g. [51, 60, 83] for further reference.

In the following let $\mathcal{U}$, $\mathcal{Q}$ be Hilbert spaces and consider a generic optimal control problem of the form

$$\min_{(\mathrm{u},\mathrm{q})\in W_{ad}} \tfrac{1}{2}\|E\mathrm{u} - E\mathrm{u}^{\delta}\|_{\mathcal{U}}^2 + \tfrac{\alpha}{2}\|\mathrm{q}\|_{\mathcal{Q}}^2 =: \mathrm{J}(\mathrm{u},\mathrm{q}) \tag{4.1a}$$

$$\text{s.t. } e(\mathrm{u},\mathrm{q}) = 0, \tag{4.1b}$$

where W_{ad} denotes a closed and convex subset of $\mathcal{U} \times \mathcal{Q}$. As usual, we denote by u the state and by q the control variable. The constraint is given in form of the operator $e : \mathcal{U} \times \mathcal{Q} \to Z$ for some appropriate space Z. The operator E is called *observation operator* and maps the solution u of the equation $e(\mathrm{u},\mathrm{q}) = 0$ and the data u^{δ} to the *observation space* $\tilde{\mathcal{U}}$ which is in general different from $\mathcal{U}$. However, we assume $\tilde{\mathcal{U}} = \mathcal{U}$ in the following for simplicity.

Let us roughly discuss which steps can be undertaken to solve such an optimal control problem. We will then proceed in a similar fashion, for the problems described above, in the subsequent chapters.

Well-posedness of the state equation. As a first step, we need to establish the solvability of the constraint $e(\mathrm{u},\mathrm{q}) = 0$. In our case the constraint has the form of a partial differential equation. The solution can be defined in a weak sense and we will be able to apply some well-known results. We will use the Lax Milgram Lemma [30, 88] to show that problem (2.3a)–(2.3b) has a unique solution. For the solution of the linearized equation (3.5b)–(3.5d) we apply the splitting theorem of Brezzi [8, 37].

Reduced formulation. If the equation $e(u, q) = 0$ has a unique solution for any admissible q, this will enable us to define the solution operator $S : \mathcal{Q} \to \mathcal{U}$ such that $e(S(q), q) = 0$. The constrained optimization problem (4.1a)–(4.1b) can then be transformed into an equivalent reduced problem of the form

$$\min_{q \in \mathcal{H}_{ad}} \tfrac{1}{2}\|F(q) - Eu^{\delta}\|_{\mathcal{U}}^2 + \tfrac{\alpha}{2}\|q\|_{\mathcal{Q}}^2 = \hat{J}(q), \tag{4.2}$$

where $F(q) = ES(q)$ and $\mathcal{H}_{ad} \subset \mathcal{Q}$ denotes a closed and convex subset.

Let us note that problem (4.2) can also be derived as *Tikhonov regularization* of the inverse problem

$$F(q) = Eu^{\delta}.$$

In the context of inverse problems, F is called *forward operator*. We refer to e.g. [27, 54] for further reference.

Existence of a minimizer. To ensure the existence of a minimizer for (4.2), we need to establish that the operator

$$F : \mathcal{H}_{ad} \subset \mathcal{Q} \to \mathcal{U}$$

is weakly closed and continuous. For the definition of these notions, we refer to standard textbooks like e.g. [27, 19]. The corresponding assumptions have to be shown for the particular problems described in sections 2 and 3. Note that for the fluid-dynamically consistent filter described in section 3, F is a linear operator. Therefore, the functional $\hat{J}$ is strictly convex and the minimizer is unique in this case.

Optimality conditions. The existence of a minimizer will be the basic theoretical justification of the proposed methods, but in order to derive a practicable method, we need an algorithm to compute such a solution. Depending on the smoothness of the functional and the constraint, the minimizer can be characterized by certain *optimality conditions* [60, 51]. To derive such a condition, let us assume that the operators F and e as well as the functionals J and $\hat{J}$ are continuously differentiable in the following.

The first-order optimality condition for problem (4.1a)–(4.1b) or equivalently problem (4.2) is given by the *variational inequality* [51, 83, 60]

$$\left\langle \tfrac{d}{dq}\hat{J}(q), q - \tilde{q} \right\rangle_{\mathcal{Q}^* \times \mathcal{Q}} = \left\langle \tfrac{d}{dq} J(u(q), q), q - \tilde{q} \right\rangle_{\mathcal{Q}^* \times \mathcal{Q}} \geq 0 \tag{4.3}$$

for all $\tilde{q} \in \mathcal{H}_{ad}$. We call any point which fulfills such an inequality a *critical point*. Following a standard procedure, see e.g. [51], we can compute the gradient $\nabla\hat{J}$ of the reduced functional and equivalently reformulate (4.3) to the projected equation

$$q - \mathcal{P}_{\mathcal{H}_{ad}}(q - \gamma \nabla \hat{J}(q)) = 0 \tag{4.4}$$

for any $\gamma > 0$. Here, $\mathcal{P}_{\mathcal{H}_{ad}} : \mathcal{Q} \to \mathcal{H}_{ad} \subset \mathcal{Q}$ denotes the projection onto the convex set $\mathcal{H}_{ad}$.

Representation of the gradient. To compute the gradient $\nabla\hat{J}$, we observe from the reduced formulation that the directional derivative of the objective functional $\hat{J}$ is given by

$$\langle \hat{J}'(q), \delta q \rangle_{\mathcal{Q}^* \times \mathcal{Q}} = \big(F(q) - Eu^\delta, F'(q)\delta q\big)_{\mathcal{U}} + \alpha \big(q, \delta q\big)_{\mathcal{Q}}$$

where $(\cdot,\cdot)_{\mathcal{U}}$ and $(\cdot,\cdot)_{\mathcal{Q}}$ denote the scalar products for the spaces $\mathcal{U}$ and $\mathcal{Q}$ respectively, and the operator $F'(h) : \mathcal{Q} \to \mathcal{U}$ denotes the Fréchet-derivative of the forward operator.

Obviously, $\hat{J}'(q) : \mathcal{Q} \to \mathbb{R}$ defines a linear functional and we denote by the gradient $\nabla\hat{J}(q)$ its *Riesz representation* defined by

$$\big(\nabla\hat{J}(q), \delta q\big)_{\mathcal{Q}} := \langle \hat{J}'(q), \delta q \rangle_{\mathcal{Q}^* \times \mathcal{Q}} = \big(F'(q)^*(F(q) - Eu^\delta), \delta q\big)_{\mathcal{Q}} + \alpha \big(q, \delta q\big)_{\mathcal{Q}}$$

for all $\delta q \in \mathcal{Q}$. The *adjoint operator* $F'(q)^* : \mathcal{U} \to \mathcal{Q}$ is defined via

$$\big(F'(q)^* u, q\big)_{\mathcal{Q}} = \big(u, F'(q)q\big)_{\mathcal{U}}.$$

For the problems of interest here, the forward operator is defined implicitly via the solution of a partial differential equation, like for instance (2.3a)–(2.3b) or (3.5b)–(3.5d). Therefore, we will be able to derive an explicit expression for the gradient utilizing an *adjoint equation*.

Numerical solution. If we have for the admissible set that $\mathcal{H}_{\text{ad}} = \mathcal{Q}$, the variational inequality (4.3) becomes an equality. In some cases, especially if the problem is linear, the so-called *KKT system*, see e.g. [51, 60], may be solved directly for a critical point. Note, however, that in this case a coupled system has to be solved, including an equation for the primal state u, an equation for an additional *dual state* p, and the optimality condition (4.3). Such an approach is usually referred to as *all-at-once* method [47].

In general, such an approach may not be feasible and an iterative approximation of the critical point has to be employed. Motivated by the projected equation (4.4), we employ iterative methods of the form

$$\mathrm{q}_{n+1} = \mathcal{P}_{\mathcal{H}_{\text{ad}}}\big(\mathrm{q}_n - \gamma_n C_n \nabla \hat{\mathrm{J}}(\mathrm{q}_n)\big)$$

for some step size $\gamma_n > 0$ and a suitable operator C_n. While several well-known methods can be written in this form, we mention here the *projected gradient* method [5], i.e. $C = I$, and the *iteratively regularized Gauß-Newton* method [56], where

$$C_n = (\mathrm{F}'(\mathrm{q}_n)^* \mathrm{F}'(\mathrm{q}_n) + \alpha I)^{-1}.$$

Under certain regularity assumptions on the forward operator, it can be shown that a step size $\gamma_n > 0$ exists (and can be e.g. computed using Armijo's rule [65]) such that the method converges to a stationary point. Similar methods are also known in the context of inverse problems, see e.g. [27].

Discretization. For the problems of interest here, we are able to apply a systematic discretization using finite elements. As a first step, we need to evaluate the forward operator F, i.e. to solve partial differential equation. For the discretization of problem (2.3a)–(2.3b), we will apply a discretization using finite elements for elliptic problems, see e.g. [10, 18]. Since the linearized equations (3.5b)–(3.5d) take the form of a saddle-point problem, we will apply a finite element discretization suited for such problems, see for instance [37, 8].

Using a suitable basis for the finite dimensional spaces the optimization problems (4.2) or (4.1a)–(4.1b) can be approximated with a finite dimensional optimization problem with algebraic constraints [51, 47]. Further, the iterative methods described above can be employed in a systematic fashion.

II GEOMETRY IDENTIFICATION FROM DENSITY MEASUREMENTS

Let us recall and discuss the geometry identification problem outlined in section 2 in more detail. The basic problem is a in some sense trivial shape identification problem, i.e. to identify a domain Ω from measurements χ_Ω^δ, where χ^δ denotes a perturbed indicator function. For convenience, we denote the available density data by f^δ from now on. The situation where f^δ corresponds to an indicator function will be treated as special case later on. Using such measurements, we want to identify Ω as the transformation of a reference domain Ω^{ref}.

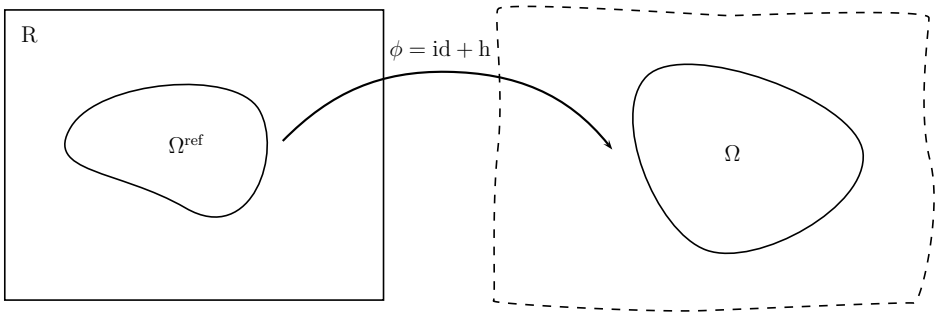

Figure 2.1 The transformation $\phi = \mathrm{id} + \mathrm{h}$ transforms a given reference frame R. We aim to find h such that $\phi(\Omega^{\text{ref}}) = \Omega$.

Let $R \subset \mathbb{R}^d$, for $d = 2, 3$ be a bounded Lipschitz domain, which could e.g. be chosen as the *field of view*, and $\Omega^{\text{ref}} \subset R$ compactly contained in R, c.f. Figure 2.1. Further, we introduce transformations $\phi : R \to \phi(R)$ of the form $\phi(x) = x + h(x)$, where $x \in R$. Let us denote by $\mathcal{H}_{\text{ad}}$ the set of admissible deformations, which we define below. The domain identification problem is then to find a suitable deformation $h \in \mathcal{H}_{\text{ad}}$ such that

$$f^\delta \circ (\mathrm{id} + h) = f^{\text{ref}}, \tag{5.1}$$

where f^{ref} denotes the density function corresponding to Ω^{ref}.

Instead of directly comparing the density functions, we rather measure the distance of the corresponding domains using the artificial potentials p and p^{ref} which are the solution of

$$-\Delta p + p = f^{\delta} \circ (\mathrm{id} + h) \quad \text{in } R, \tag{5.2a}$$
$$\partial_n p = 0 \quad \text{on } \partial R, \tag{5.2b}$$

and

$$-\Delta p^{\mathrm{ref}} + p^{\mathrm{ref}} = f^{\mathrm{ref}} \quad \text{in } R, \tag{5.3a}$$
$$\partial_n p^{\mathrm{ref}} = 0 \quad \text{on } \partial R, \tag{5.3b}$$

respectively. The resulting geometry identification problem derived from (5.1) can then be formulated as the inverse problem to find $h \in \mathcal{H}_{\mathrm{ad}}$ such that

$$F(h) = p^{\mathrm{ref}}, \tag{5.4}$$

where

$$F : \mathcal{H}_{\mathrm{ad}} \to H^1(R),$$
$$h \mapsto p[h]$$

is defined via the solution $p = p[h]$ of (5.2a)–(5.2b).

Outline. The remainder of part II is organized as follows. In section 5, we introduce the forward operator F and establish some important properties. In order to enable a stable numerical solution of the inverse problem (5.4), we propose and analyze a regularization strategy in section 6. Further, we discuss in this section the approximation of minimizers with iterative methods. Finally, we discuss the numerical realization of the identification problem in section 7 and show computational examples in section 8.

5 The forward operator

In this section, we define and analyze the forward operator F in (5.4). We establish its well-posedness and further properties like continuity and differentiability. In particular, we will show that the inverse problem (5.4) is not well-posed in the sense of Hadamard [41].

5.1 Well-posedness

In order to establish the well-posedness of the forward operator F, we define the set $\mathcal{H}_{\mathrm{ad}}$ of admissible variations first. Further, we will show that problem (5.2a)–(5.2b) has a unique weak solution for any admissible deformation.

Auxiliary results. The main requirement for the definition of the admissible set $\mathcal{H}_{\mathrm{ad}}$ will be that ϕ defines a differentiable and invertible mapping. We start with the following simple observation.

Lemma 5.1. *Let* $\phi = \mathrm{id} + \mathrm{h}$, $\mathrm{h} \in H^1(\mathrm{R})$ *and* $\|D\mathrm{h}\|_{L^\infty(\mathrm{R})} \leq 1 - \varepsilon$ *for some* $\varepsilon > 0$. *Then, the mapping* $\phi : \mathrm{R} \to \phi(\mathrm{R})$ *is invertible and there holds*

$$\|D\phi^{-1}\|_{L^\infty(\phi(\mathrm{R}))} \leq \tfrac{1}{\varepsilon}.$$

In particular, the estimate is independent of h.

Proof. Using a fixed point argument, we infer from $\|D\mathrm{h}\|_\infty \leq 1 - \varepsilon$ that the mapping ϕ is injective. The Neumann series

$$D\phi^{-1} = \big(\mathrm{I} + D\mathrm{h}\big)^{-1} = \sum_{k=0}^{\infty} \big(-D\mathrm{h}\big)^k$$

converges and therefore $D\phi$ is invertible with $\|D\phi^{-1}\|_\infty \leq \frac{1}{\varepsilon}$. By the inverse function theorem, ϕ is also invertible and its inverse is a $W^{1,\infty}$-function. □

Lemma 5.1 motivates us to define the set of admissible deformations such that the mapping ϕ is invertible, i.e.

$$\mathcal{H}_{\mathrm{ad}} := \{\mathrm{h} \in H^1(\mathrm{R})^d : \|D\mathrm{h}\|_{L^\infty(\mathrm{R})} \leq 1 - \varepsilon\}. \tag{5.5}$$

From this definition, we directly infer that for every admissible deformation $h \in \mathcal{H}_{ad}$, any L^p-function evaluated in the deformed domain $\phi(\Omega^{ref})$ is again an integrable function.

Lemma 5.2. *Let* $f \in L^p(\mathbb{R}^d)$ *for* $1 \leq p < \infty$ *and* $h \in \mathcal{H}_{ad}$. *Then* $f \circ (id + h)$ *is an* L^p*-function and there holds*

$$\underline{C}\|f \circ (id + h)\|_{L^p(R)} \leq \|f\|_{L^p(\phi(R))} \leq \overline{C}\|f \circ (id + h)\|_{L^p(R)},$$

where the constants $\underline{C}$ *and* $\overline{C}$ *do not depend on* h.

Proof. Using a density argument for L^p-functions, see e.g. [2], it is enough to proof the results for a sufficiently smooth function f. From the transformation formula, we have

$$\int_R |f \circ (id + h)|^p = \int_{\phi(R)} |f|^p |\det D\phi^{-1}| \leq C\|f\|^p_{L^p(\phi(R))}.$$

The second estimate follows with the same argument. Note that $\underline{C}$ and $\overline{C}$ do not depend on h due to Lemma 5.1. □

The operator F**.** We establish the well-posedness of the operator F as a next step. For that, we show that equation (5.2a)–(5.2b) has a unique weak solution for every admissible deformation $h \in \mathcal{H}_{ad}$. As usual, the weak formulation of (5.2a)–(5.2b) is to find $p \in H^1(R)$ such that

$$\int_R \nabla p(x)\nabla v(x) + p(x)v(x)dx = \int_R f(x + h(x))v(x)dx \tag{5.6}$$

for all $v \in H^1(R)$. As a direct consequence of Lemma 5.2, we have:

Lemma 5.3. *Let* $f^\delta \in L^q(\mathbb{R}^d)$ *for* $\frac{2d}{d+2} \leq q \leq \infty$ *and* $h \in \mathcal{H}_{ad}$. *Then, the problem* (5.2a)–(5.2b) *has a unique weak solution* $p = p[h] \in H^1(R)$ *which satisfies*

$$\|p\|_{H^1(R)} \leq C_q\|f^\delta\|_{L^q(\mathbb{R}^d)} \tag{5.7}$$

with a constant C_q *that only depends on the domain* R *and the set* $\mathcal{H}_{ad}$.

Proof. By Lemma 5.2, we have that $f^\delta \circ (id + h) \in L^q(R)$ for $h \in \mathcal{H}_{ad}$. For $\frac{2d}{d+2} \leq q \leq \infty$ there holds $L^q \subset H^{-1}$ and $f^\delta \circ (id + h)$ defines a linear functional on $H^1(R)$. The left-hand side of the weak form (5.6) is coercive with respect to

the H^1-norm, and therefore, problem (5.2a)–(5.2b) admits a unique solution p which satisfies the estimate (5.7) due to the Lax-Milgram Lemma [30]. □

As a consequence of Lemma 5.3, the forward operator

$$\begin{aligned} \mathrm{F} : \mathcal{H}_{\mathrm{ad}} \subset H^1(\mathrm{R})^d &\to H^1(\mathrm{R}), \\ \mathrm{h} &\mapsto \mathrm{p}[\mathrm{h}], \end{aligned} \tag{5.8}$$

is well-defined. Note that F is a nonlinear operator between Hilbert spaces mapping an admissible deformation h to the solution p[h] of problem (5.2a)–(5.2b). We will also need the following property of the admissible set $\mathcal{H}_{\mathrm{ad}}$.

Lemma 5.4. *For any $0 < \varepsilon < 1$ the set $\mathcal{H}_{\mathrm{ad}}$ is closed in $H^1(\mathrm{R})^d$, convex, and therefore also weakly closed, i.e. for every weakly convergent sequence*

$$\mathcal{H}_{\mathrm{ad}} \supset \mathrm{h}_n \rightharpoonup \mathrm{h}, \quad n \to \infty$$

in $H^1(\mathrm{R})^d$, there holds $\mathrm{h} \in \mathcal{H}_{\mathrm{ad}}$.

Proof. Let $(\mathrm{h}_n) \subset \mathcal{H}_{\mathrm{ad}}$ be a sequence with $\mathrm{h}_n \to \mathrm{h}$ in $H^1(\mathrm{R})^d$ for some $\mathrm{h} \in H^1(\mathrm{R})^d$. Then, there holds

$$\|\nabla \mathrm{h}\|_{L^\infty(\mathrm{R})} = \lim_{n\to\infty} \|\nabla \mathrm{h}_n\|_{L^\infty(\mathrm{R})} \leq 1 - \varepsilon.$$

Further, we have for $\mathrm{h}_1, \mathrm{h}_2 \in \mathcal{H}_{\mathrm{ad}}$ and $t \in (0,1)$, that

$$\|t\nabla \mathrm{h}_1 + (1-t)\nabla \mathrm{h}_2\|_{L^\infty(\mathrm{R})} \leq t\|\nabla \mathrm{h}_1\|_{L^\infty(\mathrm{R})} + (1-t)\|\nabla \mathrm{h}_2\|_{L^\infty(\mathrm{R})} \leq 1 - \varepsilon.$$

Therefore, the set $\mathcal{H}_{\mathrm{ad}}$ is closed and convex, and we infer that it is also weakly closed, see e.g. [88, Section V.1]. □

We will now establish further properties of the operator F which will be important for the analysis of the shape identification problem (5.4).

5.2 Continuity and Differentiability

Lemma 5.4 shows that F is defined on a closed and convex subset of the Hilbert space $H^1(\mathrm{R})^d$. Let us note that the set $\mathcal{H}_{\mathrm{ad}} \subset H^1(\mathrm{R})^d$ in (5.5) has no interior point. Therefore, continuity and differentiability have to be understood with respect to the relative topology. We refer to [23], for a similar problem.

Remark 5.5. In the following, we will require a somewhat higher regularity for the density function f^δ, i.e. we assume $f^\delta \in W^{1,\infty}(\mathbb{R}^d)$. This will simplify the analysis and the implementation of numerical methods to some extent. In applications, we typically have that f^δ is an approximation of the indicator function χ_Ω after employing a suitable cut-off function. However, since f^δ is usually given from discrete measurements, we may assume a certain smoothness after interpolation.

Continuity. In order to show that the forward operator F is continuous, we establish that for any convergent sequence h_n of admissible deformations the corresponding potentials p_n also converge.

Theorem 5.6. *Let $f^\delta \in W^{1,\infty}(\mathbb{R}^d)$. Then, the operator $F : \mathcal{H}_{ad} \subset H^1(R)^d \to H^1(R)$ defined in* (5.8) *is Lipschitz-continuous.*

Proof. Let $(h_n) \subset \mathcal{H}_{ad}$, $n \in \mathbb{N}$ be a sequence converging to h in $H^1(R)^d$. Since $\mathcal{H}_{ad}$ is closed, we have $h \in \mathcal{H}_{ad}$. Let us further denote by $p_n = F(h_n)$ and $p = F(h)$ the unique weak solutions of (5.2a)–(5.2b) corresponding to h_n or h, respectively. We have that $h_s = h + s(h_n - h) \in \mathcal{H}_{ad}$ for any $0 \le s \le 1$, by Lemma 5.4, and therefore $\nabla f^\delta \circ (\mathrm{id} + h_s)$ is integrable by Lemma 5.2. Then,

$$\begin{aligned}
&\int_R \nabla(p - p_n)\nabla v + (p - p_n)v \\
&= \int_R \big(f^\delta \circ (\mathrm{id} + h) - f^\delta \circ (\mathrm{id} + h_n)\big)v \\
&= \int_R \Big[\int_0^1 \nabla f^\delta \circ \big(\mathrm{id} + h + s(h_n - h)\big)(h - h_n)v\,ds \Big] \\
&= \int_0^1 \int_R \nabla f^\delta \circ (\mathrm{id} + h_s)(h - h_n)v \\
&\le \|\nabla f^\delta\|_{L^\infty(\mathbb{R}^d)} \|h - h_n\|_{L^2(R)} \|v\|_{L^2(R)},
\end{aligned}$$

where we switched the order of integration using Fubini's theorem. Using $v = p - p_n$ as a test function, we see that

$$\|p - p_n\|_{H^1(R)} \le \|\nabla f^\delta\|_{L^\infty(\mathbb{R}^d)} \|h - h_n\|_{L^2(R)} \le C_f \|h - h_n\|_{H^1(R)}, \tag{5.9}$$

with constant $C_f = \|\nabla f^\delta\|_{L^\infty(\mathbb{R}^d)}$ independent of h. □

Compactness and weak closedness. In Theorem 5.6, we established that the potentials p_n converge if the deformations h_n converge with respect to the H^1-topology. From equation (5.9), however, we observe that p_n converges to p in $H^1(\mathrm{R})$ if h_n converges to h in $L^2(\mathrm{R})$. This enables us to show that the forward operator is *completely continuous*.

Corollary 5.7. *Let* $\mathrm{f}^\delta \in W^{1,\infty}(\mathbb{R}^d)$. *Then, the operator* $\mathrm{F} : \mathcal{H}_{\mathrm{ad}} \subset H^1(\mathrm{R})^d \to H^1(\mathrm{R})$ *defined in* (5.8) *is completely continuous, i.e. for any weakly convergent sequence*

$$\mathcal{H}_{\mathrm{ad}} \supset \mathrm{h}_n \rightharpoonup \mathrm{h} \text{ in } H^1(\mathrm{R})^d$$

it holds that $\mathrm{F}(\mathrm{h}_n) \to \mathrm{F}(\mathrm{h})$ *converges strongly in* $H^1(\mathrm{R})$.

Proof. Let $(\mathrm{h}_n) \subset \mathcal{H}_{\mathrm{ad}}$ be a weakly convergent sequence to some $\mathrm{h} \in H^1(\mathrm{R})$. From Lemma 5.4, we infer that $\mathrm{h} \in \mathcal{H}_{\mathrm{ad}}$. From the Rellich-Kondrachov Theorem, we have that $\|\mathrm{h}_n - \mathrm{h}\|_{L^2} \to 0$, since any weakly convergent subsequence in $H^1(\mathrm{R})$ converges strongly in $L^2(\mathrm{R})$. From the estimate (5.9) with $\mathrm{p} = \mathrm{F}(\mathrm{h})$ and $\mathrm{p}_n = \mathrm{F}(\mathrm{h}_n)$, we can therefore deduce that $\mathrm{F}(\mathrm{h}_n) \to \mathrm{F}(\mathrm{h})$ in $H^1(\mathrm{R})$. □

As a direct consequence, we have that the forward operator is weakly closed.

Corollary 5.8. *The forward operator* F *defined in* (5.8) *is weakly closed, i.e. for any weakly convergent sequence*

$$\mathcal{H}_{\mathrm{ad}} \supset \mathrm{h}_n \rightharpoonup \mathrm{h} \text{ in } H^1(\mathrm{R})^d$$

with $\mathrm{F}(\mathrm{h}_n) \rightharpoonup \mathrm{p}$ *for some* $\mathrm{p} \in H^1(\mathrm{R})$, *we have that* $\mathrm{h} \in \mathcal{H}_{\mathrm{ad}}$ *and* $\mathrm{F}(\mathrm{h}) = \mathrm{p}$.

Proof. From Corollary 5.7, we infer that F is weakly continuous. The set $\mathcal{H}_{\mathrm{ad}}$ is weakly closed by Lemma 5.4 and thus F is weakly closed, see e.g. [88]. □

From the fact that F is completely continuous and weakly closed, we infer that even if the inverse F^{-1} exists, which does not have to be the case, see Remark 2.1, it does not define a continuous operator.

Lemma 5.9. *There exists a sequence* $\mathrm{h}_n \in \mathcal{H}_{\mathrm{ad}}$ *with* $\mathrm{h}_n \not\to \mathrm{h}$ *in* $H^1(\mathrm{R})^d$, *such that we have for the corresponding potentials* $\mathrm{p}_n = \mathrm{F}(\mathrm{h}_n) \subset H^1(\mathrm{R})$ *that*

$$\mathrm{p}_n \to \mathrm{p}^{\mathrm{ref}} \in H^1(\mathrm{R})$$

converges in $H^1(\mathrm{R})$.

Proof. Since $\mathcal{H}_{\mathrm{ad}}$ is infinite dimensional, there exists a weakly convergent sequence in $\mathcal{H}_{\mathrm{ad}}$ with $\mathrm{h}_n \rightharpoonup \mathrm{h}$ but $\mathrm{h}_n \not\to \mathrm{h}$ in $H^1(\mathrm{R})^d$. Take for example the function $g(x) = -\frac{1}{n\sqrt{\pi}} \cos nx$, which has bounded derivative with constant L^2-norm, but the derivative converges weakly to zero.

The operator $\mathrm{F} : \mathcal{H}_{\mathrm{ad}} \subset H^1(\mathrm{R})^d \to H^1(\mathrm{R})$ is completely continuous by Corollary 5.7, and therefore, we have that $\mathrm{F}(\mathrm{h}_n) = \mathrm{p}_n \to \mathrm{p}^{\mathrm{ref}}$ for some $\mathrm{p}^{\mathrm{ref}} \in H^1(\mathrm{R})$. Further, F is weakly closed by Corollary 5.8, which implies $\mathrm{p}^{\mathrm{ref}} = \mathrm{F}(\mathrm{h})$. This concludes the proof, see also [27, Prop. 10.1]. □

Remark. Note that Lemma 5.9 especially implies that the solution of problem (5.4) does not depend continuously on the data. Therefore, the inverse problem (5.4) is not well-posed in this sense.

Differentiability. Besides the continuity of the forward operator, we establish the differentiability of F in a next step. We will need the derivative below for the analysis of the geometry identification method.

Theorem 5.10. *Let* $\mathrm{f}^\delta \in W^{1,\infty}(\mathbb{R}^d)$ *and* $\mathrm{h} \in \mathcal{H}_{\mathrm{ad}}$. *Then, for any* $\delta\mathrm{h} \in W^{1,\infty}(\mathrm{R})^d$ *the derivative of* $\mathrm{F}(\mathrm{h})$ *in direction* $\delta\mathrm{h}$ *is given by the unique solution of the variational problem*

$$\Big(\partial_{\delta\mathrm{h}}\mathrm{F}(\mathrm{h}), \mathrm{v}\Big)_{H^1(\mathrm{R})} = \Big(\delta\mathrm{h} \cdot \Big[\nabla \mathrm{f}^\delta \circ (\mathrm{id} + \mathrm{h})\Big], \mathrm{v}\Big)_{L^2(\mathrm{R})} \tag{5.10}$$

for every $\mathrm{v} \in H^1(\mathrm{R})$.

Proof. We note that for $\mathrm{h} \in \mathcal{H}_{\mathrm{ad}}$, $\delta\mathrm{h} \in W^{1,\infty}(\mathrm{R})^d$, and $|t|$ small enough, we have that $\|\nabla \mathrm{h} + t\nabla\delta\mathrm{h}\|_{L^\infty(\mathrm{R})} \leq 1 - \frac{\varepsilon}{2}$. Therefore, $\mathrm{p}[\mathrm{h} + t\delta\mathrm{h}]$ is well-defined by (5.6) and we set $\delta\tilde{\mathrm{h}} = t\delta\mathrm{h}$. From the weak formulation (5.6) and the definition of $\partial_{\delta\mathrm{h}}\mathrm{F}(\mathrm{h})$, we conclude

$$\begin{aligned}
&\Big(\mathrm{F}(\mathrm{h} + \delta\tilde{\mathrm{h}}) - \mathrm{F}(\mathrm{h}) - \partial_{\delta\mathrm{h}}\mathrm{F}(\mathrm{h}), \mathrm{v}\Big)_{H^1(\mathrm{R})} \\
=& \int_{\mathrm{R}} \Big(\mathrm{f}^\delta \circ (\mathrm{id} + \mathrm{h} + \delta\tilde{\mathrm{h}}) - \mathrm{f}^\delta \circ (\mathrm{id} + \mathrm{h}) - \big[\delta\mathrm{h} \cdot \nabla \mathrm{f}^\delta \circ (\mathrm{id} + \mathrm{h})\big]\Big)\mathrm{v} \\
=& t \int_0^1 \int_{\mathrm{R}} \delta\mathrm{h}\Big(\nabla \mathrm{f}^\delta \circ (\mathrm{id} + \mathrm{h} + s\delta\tilde{\mathrm{h}}) - \nabla \mathrm{f}^\delta \circ (\mathrm{id} + \mathrm{h})\Big)\mathrm{v}\, ds = o(t),
\end{aligned}$$

since $\nabla \mathrm{f}^\delta$ is a bounded function and thus, the term under the integral converges to zero if $t \to 0$. This concludes the proof. □

Note that the directional derivative $\partial_{\delta h} F(h)$ depends linearly on the direction δh which enables us to define a linear operator

$$F'(h) : W^{1,\infty}(R)^d \to H^1(R), \quad \delta h \mapsto \partial_{\delta h} F(h).$$

The directional derivative is defined for all suitable variations $\delta h \in W^{1,\infty}(R)^d$. Using a density argument, we have the following.

Corollary 5.11. *Let* $f^\delta \in W^{1,\infty}(\mathbb{R}^d)$ *and* $h \in \mathcal{H}_{ad}$. *Then, the operator* $F'(h)$ *can be extended to a bounded linear operator*

$$F'(h) : H^1(R)^d \to H^1(R).$$

Proof. The operator $\delta h \mapsto \partial_{\delta h} F(h)$ is linear and defined on $W^{1,\infty}(R)^d$ which is a dense subset of $H^1(R)^d$. Further, we have that $F'(h)$ is uniformly bounded from Theorem 5.10 and since $f^\delta \in W^{1,\infty}(\mathbb{R}^d)$. The existence of a continuous extension now follows by the uniform boundedness principle [88]. □

We call F Fréchet differentiable on $\mathcal{H}_{ad}$. The derivative operator $F'(h) : H^1(R)^d \to H^1(R)$ at point $h \in \mathcal{H}_{ad}$ can be characterized by the sensitivity equation

$$\Big(F'(h)\delta h, v\Big)_{H^1(R)} = \Big(\delta h \cdot \Big[\nabla f^\delta \circ (\mathrm{id} + h)\Big], v\Big)_{L^2(R)} \tag{5.11}$$

for any variation $\delta h \in H^1(R)^d$. For further reference, we define the adjoint operator $F'(h)^* : H^1(R) \to H^1(R)^d$ in the usual way, i.e.

$$\Big(v, F'(h)\delta h\Big)_{H^1(R)} = \Big(F'(h)^* v, \delta h\Big)_{H^1(R)}$$

for all $v \in H^1(R)$ and $\delta h \in H^1(R)^d$. Similar as for the derivative $F'(h)$ we have the following representation:

Lemma 5.12. *Let* $r \in H^1(R)$. *Then* $F'(h)^* r =: z$ *is the solution of the variational problem*

$$(z, v)_{H^1(R)} = \Big(r \nabla f^\delta \circ (\mathrm{id} + h), v\Big)_{L^2(R)} \tag{5.12}$$

for all $v \in H^1(R)^d$.

Proof. From Theorem 5.10, we have that

$$\begin{aligned}\big(\mathrm{F}'(\mathrm{h})\mathrm{v}, r\big)_{H^1(\mathrm{R})} &= \big(\mathrm{v}\cdot\nabla \mathrm{f}^\delta \circ (\mathrm{id}+\mathrm{h}), r\big)_{L^2(\mathrm{R})} \\ &= \Big(r\nabla \mathrm{f}^\delta \circ (\mathrm{id}+\mathrm{h}), \mathrm{v}\Big)_{L^2(\mathrm{R})}\end{aligned}$$

which completes the proof. □

5.3 Remark on non-smooth data

For the analysis of the forward operator F, we utilized the regularity assumption $\mathrm{f}^\delta \in W^{1,\infty}(\mathbb{R}^d)$ for the data. This is not unreasonable since the measurements f^δ are usually given as values on a fixed grid which allows to define the right-hand side in (5.2a) by linear interpolation. However, for exact measurements of Ω, the density function corresponds to an indicator function which is not differentiable across the boundary of Ω. From a theoretical point of view, this limit case causes some technical difficulties but has been investigated e.g. in [48, 49], where similar problems are studied.

Let us return to the proof of Theorem 5.6 and denote $\phi = \mathrm{id}+\mathrm{h}$ and $\phi_n = \mathrm{id}+\mathrm{h}_n$ for some $\mathrm{h}, \mathrm{h}_n \in \mathcal{H}_{\mathrm{ad}}$ with h_n converging to h in $H^1(\mathrm{R})^d$. We assume here that f^δ is bounded but $\mathrm{f}^\delta \notin W^{1,\infty}(\mathrm{R})$, i.e. we can not use estimate (5.9) where the gradient of f^δ occurs. In order to show the convergence of $\mathrm{p}_n \to \mathrm{p}$, it is possible to employ the transformation formula for integrals to obtain

$$\begin{aligned}\int_{\mathrm{R}} (\mathrm{f}\circ\phi_n - \mathrm{f}\circ\phi)\mathrm{v} &= \int_{\phi_n(\mathrm{R})} \mathrm{f}(\mathrm{v}\circ\phi_n^{-1})\,|\det(D\phi_n^{-1})| \\ &\quad - \int_{\phi(\mathrm{R})} \mathrm{f}(\mathrm{v}\circ\phi^{-1})\,|\det(D\phi^{-1})|.\end{aligned}$$

If we assume now, for instance, that $\mathrm{h} \in \mathcal{C}^1(\mathrm{R})$, the potential $\mathrm{p}[\mathrm{h}]$ can be shown to depend continuously on such a deformation.

Lemma. *Let $\mathrm{f}^\delta \in L^\infty(\mathbb{R}^d)$. Then, the operator*

$$\tilde{\mathrm{F}} : \mathcal{H}_{\mathrm{ad}} \subset \mathcal{C}^1(\mathbb{R}^d) \to H^1(\mathrm{R}), \quad \mathrm{h} \mapsto \mathrm{p}[\mathrm{h}]$$

is continuously differentiable.

For a proof of this result, we refer to [48, 49, 58, 70] where similar problems for elliptic and parabolic equations are studied.

6 The domain identification method

In this section, we analyze the domain identification problem outlined in section 2 in more detail. The corresponding inverse problem was formulated as follows. Find an admissible deformation $\mathrm{h} \in \mathcal{H}_{\mathrm{ad}}$ such that

$$\mathrm{F}(\mathrm{h}) = \mathrm{p}^{\mathrm{ref}}, \tag{6.1}$$

where

$$\mathrm{F} : \mathcal{H}_{\mathrm{ad}} \subset H^1(\mathrm{R})^d \to H^1(\mathrm{R}), \quad \mathrm{h} \mapsto \mathrm{p}[\mathrm{h}]$$

is defined via the solution $\mathrm{p} = \mathrm{p}[\mathrm{h}]$ of (5.2a)–(5.2b). Let us note that the dependency on the noisy measurements χ_Ω^δ or the data f^δ respectively is hidden for this formulation in the definition of the forward operator.

In the previous section we studied some important properties of the forward operator F which are required for the analysis of the identification problem. First, we observe that the inverse problem (6.1) is ill-posed.

Lemma 6.1. *Problem* (6.1) *is not well-posed in the sense of Hadamard.*

Proof. As already discussed in Remark 2.1, a solution to problem (6.1) may neither exist in general nor be unique. By Corollary 5.7, the mapping $\mathrm{h} \mapsto \mathrm{F}(\mathrm{h})$ is completely continuous. This makes problem (6.1) ill-posed in the sense that the solution does not depend continuously on the data, see also Lemma 5.9. □

Lemma 6.1 shows that a regularization is necessary for a stable solution, and here, we consider Tikhonov regularization of the form

$$\min_{\mathrm{h}\in\mathcal{H}_{\mathrm{ad}}} \tfrac{1}{2}\|\mathrm{F}(\mathrm{h}) - \mathrm{p}^{\mathrm{ref}}\|^2_{H^1(\mathrm{R})} + \tfrac{\alpha}{2}\|\nabla \mathrm{h}\|^2_{L^2(\mathrm{R})} =: J(\mathrm{h}), \tag{6.2}$$

where $\alpha > 0$ is a regularization parameter and $\mathrm{p}^{\mathrm{ref}}$ is the unique weak solution of problem (5.3a)–(5.3b). Note that due to the definition of F, our identification method can be formulated as the nonlinear optimal control problem

$$\min_{(\mathrm{p},\mathrm{h})\in H^1(\mathrm{R})\times\mathcal{H}_{\mathrm{ad}}} \tfrac{1}{2}\|\mathrm{p}-\mathrm{p}^{\mathrm{ref}}\|^2_{H^1(\mathrm{R})} + \tfrac{\alpha}{2}\|\nabla \mathrm{h}\|^2_{L^2(\mathrm{R})} \tag{6.3a}$$

$$\text{s.t.} \quad -\Delta \mathrm{p} + \mathrm{p} = \mathrm{f}^\delta \circ (\mathrm{id} + \mathrm{h}) \qquad \text{in R}, \tag{6.3b}$$

$$\partial_n \mathrm{p} = 0 \qquad \text{on } \partial\mathrm{R}. \tag{6.3c}$$

We recall that the forward problem has a unique solution and therefore, both formulations are equivalent.

Lemma 6.2. *The problems* (6.2) *and* (6.3a) – (6.3c) *are equivalent.*

Proof. For any $\mathrm{h} \in \mathcal{H}_{\mathrm{ad}}$, problem (6.3b)–(6.3c) has a unique solution p due to Lemma 5.3. Therefore, the reduced minimization problem (6.2) is equivalent to problem (6.3a)–(6.3c). □

6.1 Existence of a minimizer

Before we verify the existence of a solution to the regularized problem (6.2), we establish some properties of the functional $J(\mathrm{h})$.

Lemma 6.3. *The functional* $\mathrm{J} : \mathcal{H}_{\mathrm{ad}} \subset H^1(\mathrm{R})^d \to \mathbb{R}$ *in* (6.2) *is non-negative, continuously differentiable, and weakly lower semi-continuous.*

Proof. By Theorem 5.10 and Corollary 5.7 the operator F is differentiable and weakly continuous. Then, the proof follows by the non-negativity and weakly lower semi-continuity of the norm, see e.g. [51]. □

To show the existence of a solution, we can now use standard arguments from the direct method in the calculus of variations, see e.g. [19, 27, 51].

Theorem 6.4. *Let* $\alpha > 0$*. Then, the minimization problem* (6.2) *has at least one solution* $\mathrm{h}_\alpha \in \mathcal{H}_{\mathrm{ad}}$*. Together with the unique solution* $\mathrm{p}_\alpha = \mathrm{p}[\mathrm{h}_\alpha]$ *of* (6.3b)–(6.3c)*, it is also a minimizer of problem* (6.3a)-(6.3c)*.*

Proof. By Lemma 6.2 the problems (6.3a) – (6.3c) and (6.2) are equivalent and therefore we only treat the latter. The functional in (6.2) is bounded from below and thus the infimum exists, and further, there exists a minimizing sequence $(\mathrm{h}_k) \subset \mathcal{H}_{\mathrm{ad}}$ such that

$$\lim_{k\to\infty} J(\mathrm{h}_k) = \inf_{\mathrm{h}\in\mathcal{H}_{\mathrm{ad}}} J(\mathrm{h}).$$

Since $\mathcal{H}_{\mathrm{ad}}$ is bounded, we have that $(\mathrm{h}_k) \subset \mathcal{H}_{\mathrm{ad}}$ is a bounded sequence in $H^1(\mathrm{R})^d$. This implies the existence of a weakly convergent subsequence [88, Section V.2] which we again denote by (h_k). From Lemma 5.4, we have that $\mathcal{H}_{\mathrm{ad}}$ is weakly closed and therefore the limit $\bar{\mathrm{h}} = \lim_{k\to\infty} \mathrm{h}_k$ also lies in $\mathcal{H}_{\mathrm{ad}}$. From

the weak closedness of F, see Corollary 5.8, and the lower semi-continuity of J, see Lemma 6.3, it then follows that

$$J(\bar{\mathrm{h}}) \leq \liminf_{k\to\infty} J(\mathrm{h}_k) \leq \lim_{k\to\infty} J(\mathrm{h}_k) = \inf_{\mathrm{h}\in\mathcal{H}_{\mathrm{ad}}} J(\mathrm{h}). \qquad \square$$

6.2 Optimality conditions

To compute a solution of problem (6.2), we proceed in a similar fashion as for the generic reduced problem discussed in section 4. The first-order optimality condition for problem (6.2) is given by the variational inequality [51, 83, 60]

$$\left(\nabla J(\mathrm{h}), \mathrm{h} - \tilde{\mathrm{h}}\right)_{H^1(\mathrm{R})} \geq 0 \tag{6.4}$$

for all $\tilde{\mathrm{h}} \in \mathcal{H}_{\mathrm{ad}} \subset H^1(\mathrm{R})^d$. In order to evaluate such a condition, we compute the gradient of the reduced functional $J(\mathrm{h})$ first.

For the directional derivative in a direction $\delta\mathrm{h} \in H^1(\mathrm{R})^d$, we have

$$\left\langle J'(\mathrm{h}), \delta\mathrm{h}\right\rangle_{H^1(\mathrm{R})'\times H^1(\mathrm{R})} = \left(\mathrm{p}[\mathrm{h}] - \mathrm{p}^{\mathrm{ref}}, \mathrm{F}'(\mathrm{h})\delta\mathrm{h}\right)_{H^1(\mathrm{R})} + \alpha \int_{\mathrm{R}} \nabla\mathrm{h}\nabla\delta\mathrm{h}.$$

Note that $J'(\mathrm{h}) : H^1(\mathrm{R})^d \to \mathbb{R}$ defines a linear functional and we compute the gradient $\nabla\mathrm{J}(\mathrm{h}) \in H^1(\mathrm{R})^d$ such that

$$\left\langle J'(\mathrm{h}), \delta\mathrm{h}\right\rangle_{H^1(\mathrm{R})'\times H^1(\mathrm{R})} = \left(\nabla\mathrm{J}(\mathrm{h}), \delta\mathrm{h}\right)_{H^1(\mathrm{R})}$$

for all $\delta\mathrm{h} \in H^1(\mathrm{R})^d$, i.e. the Riesz representation of $J'(\mathrm{h})$.

Let us define the operator $\mathcal{R} : H^1(\mathrm{R})^d \to H^1(\mathrm{R})^d$ such that

$$\left(\mathcal{R}\mathrm{h}, \delta\mathrm{h}\right)_{H^1(\mathrm{R})} = \int_{\mathrm{R}} \nabla\mathrm{h}\nabla\delta\mathrm{h} \tag{6.5}$$

for all $\delta\mathrm{h} \in H^1(\mathrm{R})^d$. Clearly $\mathcal{R} : H^1(\mathrm{R})^d \to H^1(\mathrm{R})^d$ is a bounded linear operator. By formal computation we have the following:

Lemma 6.5. *The gradient of the objective functional $J(\mathrm{h})$ has the form*

$$\nabla\mathrm{J}(\mathrm{h}) = \mathrm{F}'(\mathrm{h})^*(\mathrm{p}[\mathrm{h}] - \mathrm{p}^{\mathrm{ref}}) + \alpha\mathcal{R}\mathrm{h}.$$

Proof. The proof follows from the construction above. $\square$

In order to be able to compute the gradient, we further show the following representation formula.

Lemma 6.6. *The function* $\mathrm{z} = \mathrm{F}'(\mathrm{h})^*(\mathrm{p}[\mathrm{h}] - \mathrm{p}^{\mathrm{ref}})$ *corresponds to the weak solution of the elliptic equation*

$$\begin{aligned} -\Delta \mathrm{z} + \mathrm{z} &= \big(\mathrm{p}[\mathrm{h}] - \mathrm{p}^{\mathrm{ref}}\big)\big[\nabla \mathrm{f}^{\delta} \circ (\mathrm{id} + \mathrm{h})\big] && \text{in } \mathrm{R}, \\ \partial_{\mathrm{n}} \mathrm{z} &= 0 && \text{on } \partial\mathrm{R}, \end{aligned}$$

and the function $\mathrm{w} = \mathcal{R}\mathrm{h}$ *is the weak solution of the problem*

$$\begin{aligned} -\Delta \mathrm{w} + \mathrm{w} &= -\Delta \mathrm{h} && \text{in } \mathrm{R}, \\ \partial_{\mathrm{n}} \mathrm{w} &= \partial_{\mathrm{n}} \mathrm{h} && \text{on } \partial\mathrm{R}. \end{aligned}$$

Proof. The first assertion follows directly form Lemma 5.12. In the same fashion the second assertion follows from (6.5). □

Lemma 6.6 shows that for the evaluation of the gradient $\nabla J(\mathrm{h})$ we need to solve an additional partial differential equation which is coupled to the solution of the constraint (6.3b)–(6.3c).

Remark 6.7. From the above computation, we also see what we can expect for the case that f^{δ} is the indicator function of a domain Ω. The expression

$$\Big((\mathrm{p}[\mathrm{h}] - \mathrm{p}^{\mathrm{ref}})\nabla \mathrm{f}^{\delta} \circ (\mathrm{id} + \mathrm{h}), \delta \mathrm{h}\Big)_{L^2(\mathrm{R})}$$

formally reduces to the integral $\int_{\phi(\partial\Omega)} (\mathrm{p}[\mathrm{h}] - \mathrm{p}^{\mathrm{ref}})\delta \mathrm{h}$ in this case. The variational problem (5.12) then corresponds the problem to find a harmonic extension in $H^1(\mathrm{R})$ of the function $(\mathrm{p}[\mathrm{h}] - \mathrm{p}^{\mathrm{ref}})\delta \mathrm{h}$ defined on the boundary of $\phi(\Omega)$ only. See also section 5.3 or the domain derivative in [48, 49].

6.3 Iterative optimization algorithms

For the numerical solution of the optimization problem (6.2), we employ an iterative method of the form

$$\mathrm{h}_{n+1} = \mathcal{P}_{\mathcal{H}_{\mathrm{ad}}}\Big(\mathrm{h}_n + \gamma_n s_n\Big), \tag{6.6}$$

for $n \geq 0$. Here, we assume that some initial deformation $\mathrm{h}_0 \in \mathcal{H}_{\mathrm{ad}}$ is given.

We denote by $\mathcal{P}_{\mathcal{H}_{\text{ad}}} : H^1(\mathrm{R})^d \to \mathcal{H}_{\text{ad}} \subset H^1(\mathrm{R})^d$ the metric projection onto the closed and convex set $\mathcal{H}_{\text{ad}}$ of admissible deformations. The step size γ_n and the search direction s_n have to be chosen appropriately. Several well-known optimization algorithms, see e.g. [33, 65], can be written in this form and have also been studied for infinite dimensional problems [5, 51, 56].

As a first step, let us recall a well-known result which ensures the convergence to a critical point of the generic algorithm (6.6).

Lemma 6.8 ([51, section 2.2])**.** *Let* $\nabla \mathrm{J}(\mathrm{h}_n) \neq 0$ *and* $s_n \in H^1(\mathrm{R})^d$ *be an admissible descent direction which fulfills the* angle condition

$$\big(\nabla \mathrm{J}(\mathrm{h}_n), s_n\big)_{H^1(\mathrm{R})} \leq -\eta \|\nabla \mathrm{J}(\mathrm{h}_n)\|_{H^1(\mathrm{R})^d} \|s_n\|_{H^1(\mathrm{R})}$$

for some $0 < \eta < 1$*. Then, there exists a step size* $\gamma_n > 0$ *such that for the iterates of* (6.6) *there holds* $\mathrm{J}(\mathrm{h}_{n+1}) < \mathrm{J}(\mathrm{h}_n)$*. If* γ_n *is chosen e.g. using Armijo's rule which ensures a sufficient descent in every step, every accumulation point of the series* (h_n) *constructed by* (6.6) *is a critical point of* (6.2)*.*

Proof. For the proof, we refer to [51, section 2.2]. □

Lemma 6.8 allows for several possible choices for the descent direction s_n in (6.6). Therefore, the choice of the descent direction is another degree of freedom to promote special properties of the solution.

Steepest descent method. The most obvious choice for a search direction, which fulfills the requirements of Lemma 6.8, is the negative gradient, or the direction of *steepest descent*

$$s_{SD} = -\nabla \mathrm{J}(\mathrm{h}_n) = -\big[\mathrm{F}'(\mathrm{h}_n)^* \big(\mathrm{F}(\mathrm{h}_n) - \mathrm{p}^{\text{ref}}\big) + \alpha \mathcal{R}\mathrm{h}_n\big].$$

In this case, (6.6) takes the form of the *projected gradient method* [5, 51]. While this method can be implemented in a straight forward manner, it is well-known to converge slowly in the vicinity of local minima [65].

Gauß-Newton method. To obtain a method with better convergence properties, we use a *preconditioned gradient* of the form

$$C_{\tilde{\alpha}} s_{PG} = -\nabla J(\mathrm{h}_n), \tag{6.7}$$

as descent direction, where we choose

$$C_{\tilde{\alpha}} = \Big(\mathrm{F}'(\mathrm{h}_n)^* \mathrm{F}'(\mathrm{h}_n) + \tilde{\alpha}\mathcal{R}\Big),$$

for some $\tilde{\alpha} > \alpha$. Let us note that the pre-conditioner $C_{\tilde{\alpha}}$ is motivated by the *iteratively regularized Gauß-Newton* method [6, 56], where we have $\tilde{\alpha} = \alpha$. Formally, it may be derived by computing the Hessian of the reduced functional $J(\mathrm{h}_n)$ and dropping the second-order terms. In this sense, the original Gauß-Newton method can be interpreted as a simplified version of Newton's method, see e.g. [65], where the complete Hessian needs to be inverted.

The computation of the Gauß-Newton direction is computationally more expensive than the computation of the gradient alone. However, the main advantage of the Gauß-Newton method over the steepest descent method is that the preconditioner introduces a suitable scaling and leads to much faster convergence in problem (6.6).

Let us recall that the forward operator F was defined via the solution of a partial differential equation. Consequently also the application of the pre-conditioner involves the solution of such an equation. In order to invert $C_{\tilde{\alpha}}$, and to compute the Gauß-Newton direction, we therefore employ a *preconditioned conjugate gradient* method, see e.g. [63], for the solution of (6.7). The advantage here is that $C_{\tilde{\alpha}}$ does not need to be inverted directly.

Remark. In contrast to the Gauß-Newton method, which can be analyzed by Lemma 6.8, for Newton's method a descent of the iterates can not be guaranteed in general.

7 Numerical realization

The geometry identification problem considered here is formulated in an infinite dimensional setting. In order to obtain a computational algorithm, a suitable discretization is necessary. The underlying forward model is a Laplace equation with slightly non-standard right-hand side. For the discretization, we use a finite element method on a triangular mesh. Additionally, we comment on the treatment of the term $\int f^\delta \circ (\mathrm{id} + h)$ which is well-known for Lagrange Galerkin methods [71]. The optimal control problem (6.2) and the iteration (6.6) can then be systematically discretized in a more or less straight forward manner, see e.g. [51, 47].

7.1 The discrete problem

For the discretization of problem (5.2a)–(5.2b), we use a standard Galerkin method with first-order finite element basis functions. The procedure is well-understood and we refer to standard textbooks on the subject like e.g. [10, 18].

Let $(\mathcal{T}_h)_{h>0}$ be a family of uniformly shape regular triangulations of R [8]. The reference domain is represented using an embedded mesh such that the transformation of Ω^{ref} can be computed easily.

We define the finite element spaces

$$U_h = \left[\mathrm{P}_1(\mathcal{T}_h) \cap \mathcal{C}(\mathrm{R})\right] \subset H^1(\mathrm{R}) \quad \text{and}$$
$$Q_h = \left[\mathrm{P}_1(\mathcal{T}_h) \cap \mathcal{C}(\mathrm{R})\right]^d \subset H^1(\mathrm{R})^d$$

in the usual manner, where $\mathrm{P}_1(\mathcal{T}_h)$ denotes the space of piecewise linear polynomials on $\mathcal{T}_h$. The discrete formulation of problem (5.2a)–(5.2b) is then to find $p_h \in U_h$ such that

$$\int_{\mathrm{R}} \nabla p_h \nabla v_h + p_h v_h = \int_{\mathrm{R}} f^\delta \circ (\mathrm{id} + h_h) v_h \tag{7.1}$$

for all $v_h \in U_h$. Here, $h_h \in Q_h$ is a given discrete deformation.

Using this, we can, similar to the infinite dimensional case, define the discrete forward operator

$$\begin{aligned} \mathrm{F}_h : \mathcal{H}_{\mathrm{ad}} \cap Q_h &\to U_h, \\ \mathrm{h}_h &\mapsto \mathrm{p}_h, \end{aligned}$$

where $\mathrm{p}_h \in U_h$ is the unique solution of (7.1). Proceeding as for the infinite dimensional case in section 5, we show that problem (7.1) has a unique solution and that the forward operator is differentiable.

Lemma 7.1. *Let* $\mathrm{f}^\delta \in W^{1,\infty}(\mathbb{R}^d)$. *Then, the discrete forward operator* $\mathrm{F}_h : \mathcal{H}_{\mathrm{ad}} \cap Q_h \to U_h$ *is*

- *well-defined, i.e. problem* (7.1) *has a unique solution for every* $\mathrm{h}_h \in \mathcal{H}_{\mathrm{ad}} \cap Q_h$.
- *Lipschitz-continuous and differentiable.*

Proof. The proof follows using similar arguments as in Lemma 5.3, Theorem 5.6, and Theorem 5.10. □

It is well-known, see e.g. [10], that for first order finite elements we can expect an error estimate of the form $\|\mathrm{p} - \mathrm{p}_h\|_{H^1} = \mathcal{O}(h)$ for the solution of the discrete problem (7.1). Therefore, F_h contains some perturbations inherited from the discretization. Recall that the operator F depends on the data f^δ and is therefore already disturbed by the data error. If we choose the mesh size sufficiently small we may therefore neglect the error induced by discretization.

The discrete identification method. Using the discrete forward operator, we can now formulate the discrete identification method corresponding to (6.2). The discrete optimization problem takes the form

$$\min_{\mathrm{h}_h \in \mathcal{H}_{\mathrm{ad}} \cap Q_h} \tfrac{1}{2}\|\mathrm{F}_h(\mathrm{h}_h) - \mathrm{p}_h^{ref}\|^2_{H^1(\mathrm{R})} + \tfrac{\alpha}{2}\|\nabla \mathrm{h}_h\|^2_{L^2(\mathrm{R})^d} =: \mathrm{J}_h(\mathrm{h}_h) \tag{7.2}$$

where $\mathrm{p}_h^{\mathrm{ref}}$ is the discrete reference potential, i.e. the solution of the problem

$$\int_{\mathrm{R}} \nabla \mathrm{p}_h \nabla \mathrm{v}_h + \mathrm{p}_h \mathrm{v}_h = \int_{\mathrm{R}} \mathrm{f}^{\mathrm{ref}} \mathrm{v}_h$$

for all $v_h \in U_h$. Let us note that $\mathcal{H}_{\text{ad}} \cap Q_h$ is finite dimensional and therefore, we can show the existence of a minimizer using a much simpler argument as in Theorem 6.4.

Lemma 7.2. *Let $f^\delta \in W^{1,\infty}(\mathbb{R}^d)$. Then problem* (7.2) *has at least one minimizer.*

Proof. The finite dimensional set $\mathcal{H}_{\text{ad}} \cap Q_h$ is bounded, closed, and therefore compact. This implies that any minimizing sequence has a limit, which again lies in $\mathcal{H}_{\text{ad}} \cap Q_h$, and is therefore a minimizer. □

As before, the minimizer of (7.2) is characterized by a first-order optimality condition of the form

$$\left(\nabla J_h(h_h), h_h - \tilde{h}_h\right)_{H^1(R)} \geq 0$$

for all $\tilde{h}_h \in Q_h$. Following the same steps as in section 6.3, we compute the gradient of the discrete functional $J_h(h_h)$ as the solution of the variational problem

$$\left(\nabla J_h(h_h), \delta h_h\right)_{H^1(R)} = \left(p_h - p_h^{\text{ref}}, F_h'(h_h)\delta h_h\right)_{H^1(R)} + \alpha\left(\nabla h_h, \nabla \delta h_h\right)_{L^2(R)}$$

for all $\delta h_h \in Q_h$. Similar as before, the derivative of F_h defines an operator $F_h'(h_h) : Q_h \to U_h$ and we have that

$$\begin{aligned}
&\left(p_h - p_h^{\text{ref}}, F_h'(h_h)\delta h_h\right)_{H^1(R)} \\
=&\left(F_h'(h_h)^*(p_h - p_h^{\text{ref}}), \delta h_h\right)_{H^1(R)} \\
=&\left(\delta h_h \cdot \nabla f^\delta \circ (\mathrm{id} + h_h), p_h - p_h^{\text{ref}}\right)_{L^2(R)}
\end{aligned}$$

which also defines the adjoint operator $F_h'(h_h)^* : U_h \to Q_h$. Therefore, the gradient $z_h = \nabla J_h(h_h)$ is a solution to the problem

$$\int_R \nabla z_h \nabla v_h + z_h v_h = \int_R (p_h - p_h^{\text{ref}}) \nabla f^\delta \circ (\mathrm{id} + h_h) v_h + \alpha \int_R \nabla h_h \nabla v_h, \quad (7.3)$$

for all $v_h \in U_h$. Problem (7.3) is again of the same form as the discrete forward problem (7.1).

7.2 Reformulation as an algebraic problem

In order to compute a stationary point of (7.2) we employ an iteration of the form (6.6) as discussed in section 6.3. Here, we will derive an algebraic representation of the necessary terms and discuss the computation of a minimizer.

Following a standard procedure, we choose a piecewise linear finite element basis $\{\varphi_i\}_{i=1,\dots,N}$ of the discrete space U_h, i.e. we use the usual hat functions. Here, $N = \dim(U_h)$ denotes the dimension of U_h and for further reference, we define $\tilde{N} = dN = \dim(Q_h)$. The discrete function $\mathrm{p}_h \in U_h$ and the components $\mathrm{h}_h^k \in U_h$, for $k = 1, \dots, d$ can then be written in the form

$$\mathrm{p}_h = \sum_{i=1}^{N} \mathsf{p}_i \varphi_i \quad \text{and} \quad \mathrm{h}_h^k = \sum_{i=1}^{N} \mathsf{h}_i^k \varphi_i.$$

We define the stiffness matrix K and the mass matrix M by

$$\mathsf{K}_{ij} = (\nabla\varphi_i, \nabla\varphi_j)_{L^2(\mathrm{R})} \quad \text{and} \quad \mathsf{M}_{ij} = (\varphi_i, \varphi_j)_{L^2(\mathrm{R})}.$$

As usual, the matrices will be sparse and can be inverted using efficient techniques, see e.g. [10] for further reference. Let us also note that $(\mathsf{K} + \mathsf{M})$ and M are the gram matrices for the H^1- or L^2- norm on R, respectively.

As a next step, we compute a representation $\mathsf{f}(\mathsf{h})$ of the right-hand side $\mathrm{f}^\delta \circ (\mathrm{id} + \mathrm{h}_h)$. Recall that f^δ is interpolated from given measurements and therefore we may evaluate the term $\mathrm{f}^\delta(\mathrm{x} + \mathrm{h}_h(\mathrm{x}))$ for any given $\mathrm{x} \in \mathrm{R}$. In practice, we use a piecewise linear function f_h^δ which is precomputed. Here, the components of the right-hand side $\mathsf{f}(\mathsf{h})$ are computed via

$$\mathsf{f}(\mathsf{h})_j = \int_{\mathrm{R}} \mathrm{f}_h^\delta \circ (\mathrm{id} + \mathrm{h}_h)\phi_j = \int_{\mathrm{R}} \mathrm{f}_h^\delta(\mathrm{x} + \mathrm{h}_h(\mathrm{x}))\phi_j(\mathrm{x})d\mathrm{x}.$$

Let us note that such terms are rather common when employing Lagrange-Galerkin methods, c.f. [78, 71]. The main problem here is that numerical errors are introduced by the integration over a deformed element. However, if f_h^δ is given as a polynomial and h_h is a piecewise linear function, the integral can be computed exactly [79].

Remark 7.3. Note, that unlike for standard finite elements the function f_h^δ is not necessarily a differentiable function on the deformed triangle. Similar prob-

lems occur if f^δ has discontinuities. Therefore, care has to be taken when using numerical integration rules.

The forward problem (7.1) is then equivalently reformulated as the linear system of equations

$$(K + M)p = f(h). \tag{7.4}$$

Proceeding in the same fashion, we can now also compute the gradient $\nabla J_h(h_h)$ of the discrete functional as the solution of equation (7.3). We denote by

$$\begin{aligned} \tilde{M} &= \operatorname{diag}(M, \dots, M) \in \mathbb{R}^{\tilde{N}\times\tilde{N}} \quad \text{and} \\ \tilde{K} &= \operatorname{diag}(K, \dots, K) \in \mathbb{R}^{\tilde{N}\times\tilde{N}} \end{aligned}$$

the mass and stiffness matrices on Q_h. Let z be the discrete representation of z_h. Then, we have that

$$(\tilde{K} + \tilde{M})z = M_f(p - p^{ref}) + \alpha\tilde{K}h, \tag{7.5}$$

where we define the matrix

$$(M_f)_{ij} = \int_R \phi_i \cdot \nabla f^\delta \circ (\mathrm{id} + h_h)\varphi_j \tag{7.6}$$

which is computed for every given $h_h \in Q_h$. We denote by ϕ_i a basis of Q_h and note that $M_f \in \mathbb{R}^{\tilde{N}\times N}$. In the same fashion, we have for the computation of the preconditioned gradient direction, see (6.7),

$$(\tilde{K} + \tilde{M})^{-1}\left[(M_f(K + M)^{-1}M_f^\top + \tilde{\alpha}\tilde{K})\right]s_{PG} = (\tilde{K} + \tilde{M})^{-1}\left[M_f(p - p^{ref}) + \alpha\tilde{K}h\right]$$

and we employ a preconditioned conjugated gradient method, see e.g. [63], to compute the search direction s_{PG}. Finally, we employ the iteration (6.6) to approximate a critical point of (7.2).

Remark 7.4. Note that we did not discuss so far the projection $\mathcal{P}_{\mathcal{H}_{\mathrm{ad}}}$ onto the admissible set. Recall, that the admissible set was chosen such that every admissible deformation defines a diffeomorphism. As we will see in our numerical examples, such a condition is fulfilled automatically if the regularization parameter is chosen large enough.

7.3 Further comments

Let us make some further comments on the domain identification method. We discuss the choice of the reference mesh and some alternative regularization terms, which can be used to promote certain properties of the result.

Choice of the initial reference mesh. The regularization term $\|\nabla h\|^2$ in (6.2) in some sense promotes "small deformations" for a minimizer. Therefore, we require the initial reference mesh to have a "good mesh quality" and to be topologically close to the domain of interest in order to compute a reasonable domain reconstruction. In this sense the reference mesh can be interpreted as the initial value for the iteration (6.6) if we choose $h_0 = 0$. This is reasonable if the geometry is already known from e.g. CAD data and only scaling and shifting may be necessary.

The main motivation for our approach is, however, that for three-dimensional geometries it is possible treat a series of two-dimensional problems. For fluid-dynamical problems, there usually exists a main flow direction. Along this direction, we can expect the geometry to have approximately the same cross-section. Therefore, we need to provide a good initial mesh for a two-dimensional slice only and the three-dimensional geometry can be identified automatically. We use the same reference mesh for every cross-section which enables us to directly build a three dimensional prism mesh. We show an example for the identification of a human blood vessel in this fashion in section 13.

Alternative regularization terms. Let us comment on different modifications leading to other formulations of the domain identification method (6.2). Recall that the domain identification method was intentionally designed to minimize the residual $\|F(h) - p^{\mathrm{ref}}\|_{H^1(R)}$ under the constraint $h \in \mathcal{H}_{\mathrm{ad}}$. Note that this can be formally realized, e.g. by setting $\alpha = 0$ in (6.7) for fixed $\tilde{\alpha} > 0$, which would yield the *Levenberg-Marquart* method. However, this method can not be analyzed with the results presented here, see [27] for further details.

So far, we implicitly assumed that choosing a large regularization parameter corresponds to a good mesh quality if the initial mesh was chosen correspondingly. Let us note here that the notion of a "suitable" triangulation is not defined uniquely and we refer to e.g. [35, 44] for different mesh quality measures. The semi-norm $\|\nabla h\|^2_{L^2(R)}$ is the classical choice for Tikhonov regularization,

however, from the proof of Theorem 6.4, we see that other regularization terms which are continuously differentiable with respect to the H^1-norm could be used as well. In the following, we motivate that the Tikhonov functional in some sense corresponds to a weighted sum of the residual and some kind of "mesh quality term".

Let us note here, that generating numerical grids as deformation of a reference mesh is subject of an active research area called *variational grid generation*, see e.g. [57, 44]. Similar ideas are employed for the design of certain *moving mesh techniques* [9, 53]. Let us denote by $\xi(x) = x + h(x)$ the node positions of the deformed mesh where x denotes the node position of the reference mesh. A possible variational mesh generation technique is then given as a minimization problem of the form

$$\xi = \operatorname{argmin} \tfrac{1}{2} \int_\Omega \nabla\xi(x)^\top G^{-1}(x) \nabla\xi(x) dx.$$

The *weight function* G is used to control the "node density" in certain areas of the physical domain. Since $\nabla x = I$, the minimizer does not change if only the deformation h is used in the functional. In this sense, we may interpret the regularization term stemming from the Tikhonov regularization as a simple variational grid generation functional with weight function $G(x) \equiv 1$, which corresponds to a uniform distribution of grid points in the physical domain. As discussed before, the regularization term $\mathcal{R}$ in the Tikhonov functional J may be adapted in a suitable way with only minor effect on the theoretical treatment. Using the ideas from variational grid generation, we may therefore also use a regularization term which promotes certain mesh quality measures.

Remark 7.5. A well-known drawback of variational mesh generation techniques is that *mesh folding* can occur [16]. Different strategies exist to avoid such a behaviour, see e.g. [44]. Heuristically speaking, such problems occur if "too strong deformations" are necessary to identify the geometry. In our formulation such behaviour is, however, prevented by the constraint $h \in \mathcal{H}_{ad}$. We will present numerical examples in the next section which show that mesh folding does indeed only occur if $\|\nabla h\|_{L^\infty(R)} > 1$.

8 Computational tests

For the illustration and further support of the viability of the domain identification method, we present some preliminary computational results. For that purpose, we construct a simple reference domain Ω^{ref} which we use to reconstruct different shapes and geometries.

For the ease of presentation, we discuss a two-dimensional example only. Note that the formulation of the method is independent of the dimension. We also show an application to in-vivo data in part IV, where we treat a series of two-dimensional problems to reconstruct a volume.

Let us define the reference configuration which will serve as a basis for the computational examples we show. As reference frame, we use the square $\mathrm{R} = [-L, L]^2$ of size $2L$. The reference domain will be a circle of radius $0 < r < L$, i.e. $\Omega^{\text{ref}} = B_r(0)$, which is compactly contained in R, see Figure 2.2. For the test cases presented here we set $L = 5$ and $r = 1$.

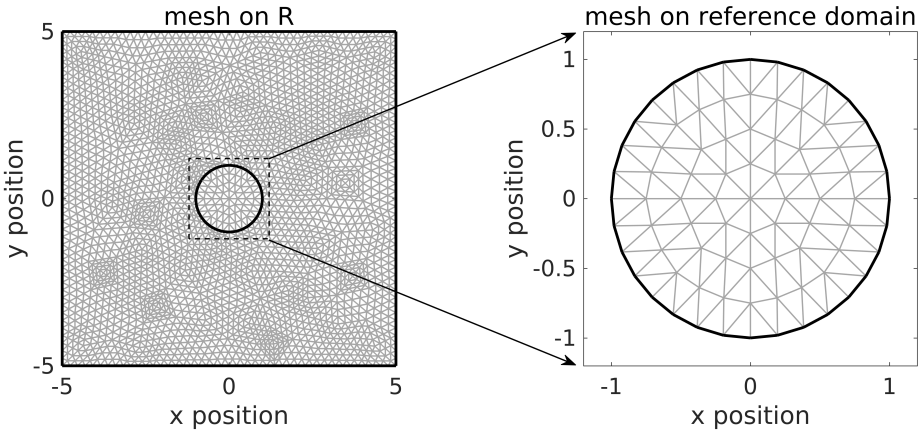

Figure 2.2 The reference configuration used for the domain identification method. We show the complete reference frame R on the left and the embedded mesh Ω^{ref} on the right.

We now construct typical domains $\Omega \subset \mathrm{R}$ and discuss the performance and limitations of our algorithms by numerical tests. For given domain $\Omega \subset \mathrm{R}$, we construct a piecewise linear approximation of the indicator function χ_Ω on a fine, regular grid. This resembles to some extent the data which we can expect from actual measurements.

8.1 Comparison of iterative methods

As discussed before, the minimizer of (6.2), or (7.2) respectively, can in principle be computed using any suitable optimization algorithm. As a first step, we compare the projected gradient method and the iteratively regularized Gauß-Newton method discussed in section 6.3. Let us note that the numerical analysis of these methods is well-understood and we do not present such results here. We refer to standard textbooks on practical optimization [65, 33].

In order to evaluate the influence of the regularization parameter in the iterative optimization algorithm proposed in section 6.3, we discuss a simple example, i.e. the identification of the circle

$$\Omega_c = \{x \in \mathbb{R}^2 : |x_1 - 0.4|^2 + |x_2 - 0.2|^2 \leq 0.9\}.$$

We use the reference domain depicted in Figure 2.2 with a uniformly refined mesh with 44177 nodes and 87648 triangles.

In order to verify that the identified domain $(\mathrm{id} + \mathrm{h})(\Omega^{\mathrm{ref}})$ is a suitable approximation of the domain of interest, we compare different "quality measures" in Table 2.1. The different iterations are stopped if the Tikhonov functional can no longer be sufficiently reduced along the computed descent direction.

Recall that the residual $\|\mathrm{p} - \mathrm{p}^{\mathrm{ref}}\|_{H^1}$ is the natural measure for the overlap of the two domains here. For comparison, we also compute the L^1-norm

$$\|\chi_\Omega^\delta \circ (\mathrm{id} + \mathrm{h}) - \chi_{\Omega^{\mathrm{ref}}}\|_{L^1(\mathrm{R})} \tag{8.1}$$

which measures the area of the domain $(\Omega^{\mathrm{ref}} \cup \Omega^\delta) \setminus (\Omega^{\mathrm{ref}} \cap \Omega^\delta)$. Both values are zero if the domains match exactly and can therefore be used as criterion for the identification.

Under the assumption that the initial mesh was regular, the norm $\|\nabla \mathrm{h}_h\|_{L^\infty(\mathrm{R})}$ corresponds to a mesh quality measure. Note that we need to compute the maximum of $\nabla \mathrm{h}$ for every iterate in order to check if a projection to the admissible domain is necessary. For the results presented here the value of $\|\nabla \mathrm{h}_h\|_{L^\infty(\mathrm{R})}$ was always bounded away from one. We list the values for the optimal deformation, however, during the iteration the value may have been larger.

The results for the identification of the circle Ω_c for different regularization parameters are listed in Table 2.1.

method	α	#it	residual	L^1-norm (8.1)	$\|\nabla h\|_\infty$
Steepest descent	1	250	0.53	0.03	0.027
	0.5	138	0.44	0.02	0.046
	0.1	133	0.16	0.007	0.09
	0.05	155	0.11	0.005	0.13
	0.01	191	0.03	0.0036	0.17
Gauß-Newton	1	4	0.54	0.03	0.026
	0.5	5	0.44	0.02	0.044
	0.1	4	0.15	0.007	0.09
	0.05	4	0.12	0.005	0.11
	0.01	4	0.028	0.0036	0.12

Table 2.1 Comparison of different methods for the identification of a circle. We show the necessary iterations to converge to a critical point as well as several quality measures for the identified domain. The iteration is stopped if the value of the residual stagnates.

As expected, the steepest descent method is outperformed by the preconditioned method in terms of necessary iterations. Further, the steepest descent method and the Gauß-Newton method compute the same critical point in both cases. However, if the regularization parameter is chosen too large the residual and also the L^1-norm indicate that the domain is not identified successfully.

Further, the regularization parameter has an influence on the maximal deformation which is indicated by the maximal value of the gradient of the deformations. This can be explained by the fact, that all norms are equivalent on finite dimensional spaces. Therefore, the penalization of the gradient ∇h_h in the L^2-norm also induces a penalization of its L^∞-norm. This indicates, that if the regularization parameter is chosen large enough the optimal deformation will lie in the admissible set $\mathcal{H}_{\text{ad}}$ automatically. We will discuss this aspect in more detail below.

The results above further indicate that the regularization parameter in the functional $J_h(h_h)$ should be chosen sufficiently small in order to identify the domain in terms of the residual or the L^1-norm. Note that of course the mesh size has an influence on what "sufficiently small" means. On the other hand, the regularization parameter also controls the maximal deformation. As we will show in the next section, we may also increase $\tilde{\alpha}$ for the pre-conditioner $C_{\tilde{\alpha}}$ in (6.7) to obtain a similar effect. Further, the usage of a larger parameter for the preconditioner ensures the mesh quality of the iterates to some extent.

8.2 Identification of irregular and non-convex shapes

Let us discuss two further examples with more complex geometries. While in the previous case only scaling and shifting of the reference domain was necessary, we treat now a convex polygon and a smooth but non-convex shape as depicted in Figure 2.3.

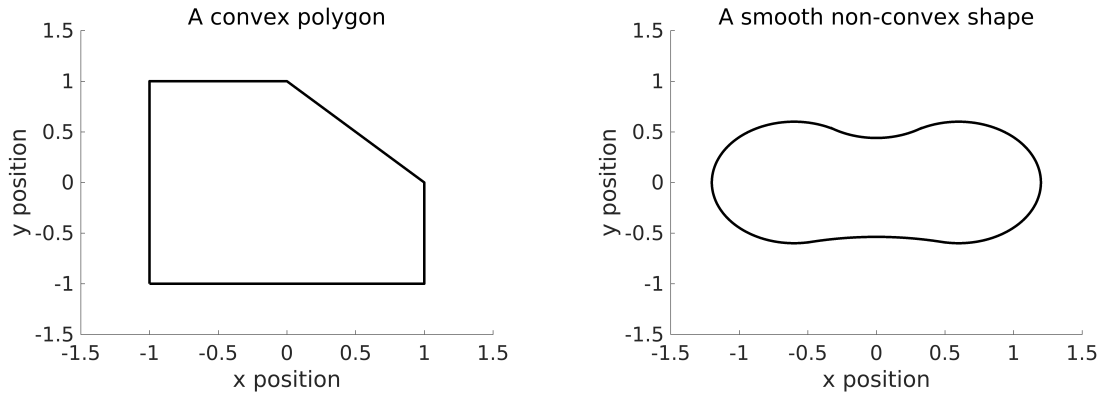

Figure 2.3 Different shapes used as example for the domain identification. We depict a convex polygon on the left and a smooth but non-convex shape on the right.

Identification of a convex polygon. We apply the domain identification method for the identification of a convex polygon depicted on the left side of Figure 2.3. As discussed in the previous section we use a sufficiently small regularization parameter in order to obtain an approximation of the convex polygon. We set $\alpha = 0.001$ here and compute the minimizer of (7.2) using the iteratively regularized Gauß-Newton method, as before, in (6.6). As above, the iteration is stopped if the functional can no longer be sufficiently reduced along the search direction and we depict the deformed reference domain in Figure 2.4

We observe that the polygon is successfully identified except for some smoothing effect at the corners. Note, however, that in context of biological applications we may not expect such corners at all. A closer inspection of the lower right corner of the polygon, see the right picture in Figure 2.4, shows that some mesh elements have been strongly deformed and are close to mesh folding.

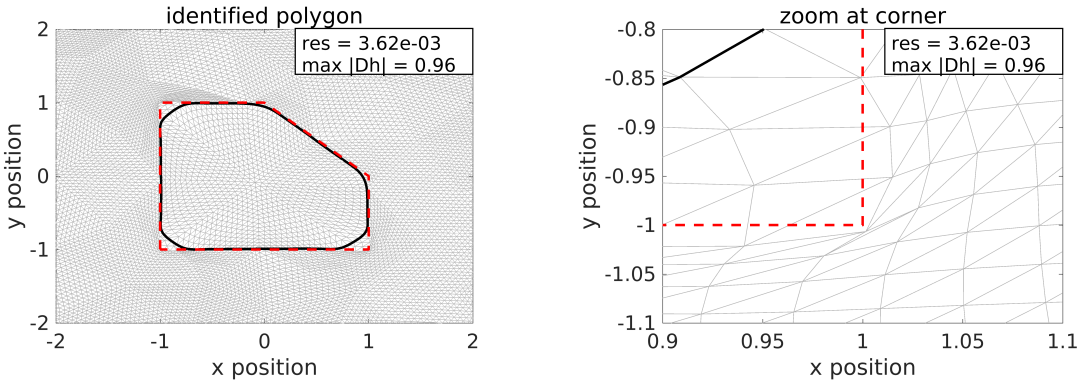

Figure 2.4 The identified polygon after 10 iterations for $\tilde{\alpha} = \alpha$ and the corresponding values of the residual and the maximum of ∇h_h. The right picture shows an enlarged area in the lower right corner of the polygon.

This is also indicated by the maximum value of $|\nabla h_h|$ which is just less than one here. In order to obtain a representation with better mesh quality we increase the parameter $\tilde{\alpha}$ in (6.7). We repeat the identification of the polygon with $\tilde{\alpha} = 0.01$ and the resulting domain is depicted in Figure 2.5.

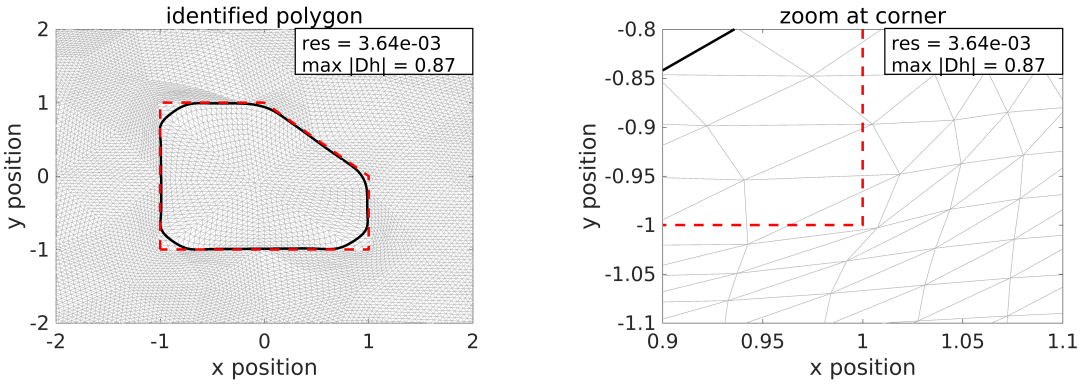

Figure 2.5 The identified polygon after 15 iterations for $\tilde{\alpha} = 0.01$ and the corresponding values of the residual and the maximum of ∇h_h. The right picture shows an enlarged area in the lower right corner of the polygon.

We observe that the increase of $\tilde{\alpha}$ has a similar effect as the increase of α in the example presented in section 8.1. Due to the stronger regularization in the preconditioner, the values of $\|\nabla h_h\|_{L^\infty(R)}$ are smaller and the mesh quality in the lower right corner of the polygon is visibly improved, see the right picture in Figure 2.5.

On the other hand, we observe that more iterations are necessary for the iteration (6.6) to converge. The result is, as expected, comparable to the Gauß-Newton method and the residuals differ only in the order of 10^{-5}.

Mesh dependence. Let us finally comment on the influence of the mesh size on the reconstruction. We depict once more the identified polygon on the left side in Figure 2.6 but computed on a coarse mesh this time. Further, we show the result of the identification for a mesh which is only refined at the boundary of the reference domain on the right side of Figure 2.6.

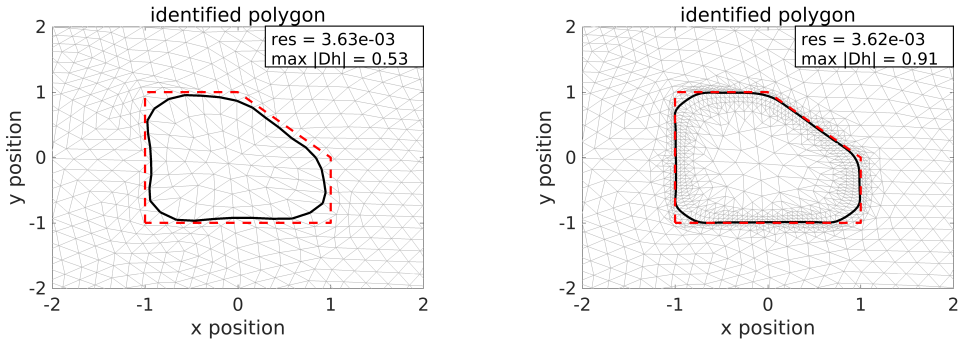

Figure 2.6 The identified polygon after 9 iterations for a coarse mesh (left) and a boundary refined mesh (right) where 15 iterations were necessary.

We observe, that the identification using the coarse mesh results in a mesh with good mesh quality. This can be explained by the fact, that on finite dimensional spaces we have an estimate of the form

$$\|\nabla \mathrm{h}_h\|_{L^\infty(\mathrm{R})} \leq C \|\nabla \mathrm{h}_h\|_{L^2(\mathrm{R})},$$

with a constant $C = C(1/h)$ depending on the mesh size, see e.g. [10]. Consequently, a penalization of $\|\mathrm{h}_h\|_{L^2(\mathrm{R})}$ in (7.2) ensures that $\mathrm{h}_h \in \mathcal{H}_{\mathrm{ad}}$ if the regularization parameter α is chosen large enough. However, on refined meshes, such an α may become arbitrarily large.

As expected, the reconstruction quality decreases for a coarser mesh in the sense that the boundary is not met exactly. For the boundary refined mesh the results are comparable to those obtained with the fine mesh. This indicates that the boundary of the reference domain needs to be sufficiently resolved, however, a coarse mesh on the remaining reference frame can be used.

Identification of a smooth non-convex domain. In comparison to the previous artificial example we show results for a smooth domain which could e.g. mimic the cross-section of a blood vessel. The additional difficulty here is that the convex reference domain has to be transformed to the non-convex shape shown on the right side of Figure 2.3.

For the identification we use again a boundary refined mesh here. For comparison, we depict the result of the identification for two different values of the regularization parameter α in Figure 2.7. In both cases we used $\tilde{\alpha} = 0.02$ for the pre-conditioner in (6.7).

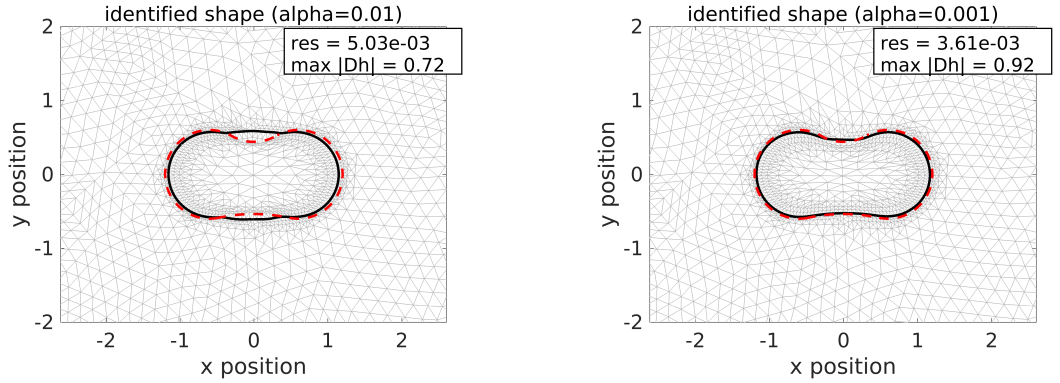

Figure 2.7 Results for the identification of a smooth non-convex shape with $\alpha = 0.01$ (left) and $\alpha = 0.001$ (right). In both cases we use $\tilde{\alpha} = 0.02$.

We observe, that the domain of interest is roughly identified for $\alpha = 0.01$, however, the result is still a nearly convex domain. To finally resolve the non-convex shape we need to further reduce the regularization parameter to $\alpha = 0.001$, see the right picture in Figure 2.7. From the maximal value of ∇h_l we see that the mesh is again a feasible triangulation here, however we expect some strongly deformed triangles.

Mesh dependence. For further comparison and to evaluate the influence of the mesh size to some extent, we repeat the same computations on a uniformly refined mesh and depict the results in Figure 2.8.

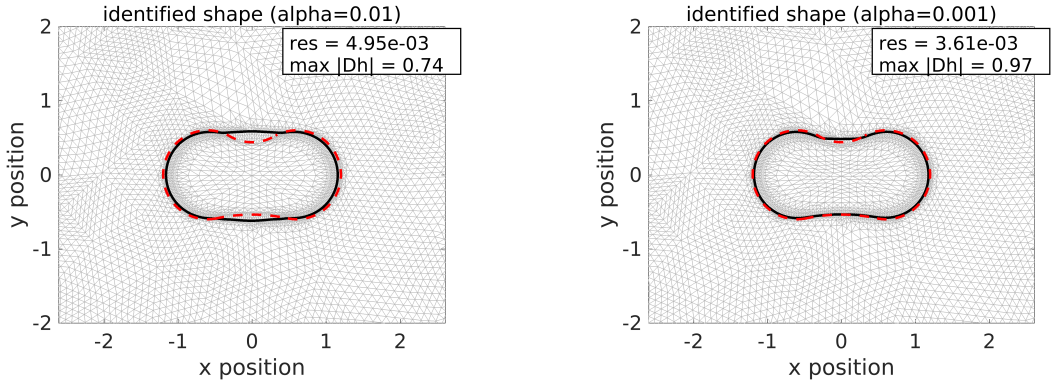

Figure 2.8 Results for the identification of a smooth non-convex shape on a uniformly refined mesh with $\alpha = 0.01$ (left) and $\alpha = 0.001$ (right). In both cases we use $\tilde{\alpha} = 0.02$ for the pre-conditioner.

We observe again the same effect if α is chosen too large. Further, due to the refined mesh, we observe an increase in the maximal deformation in terms of the maximal value of ∇h_l in both cases. If we further refine the mesh we expect to obtain no feasible triangulation for $\alpha = 0.001$ without additionally involving a projection to the admissible set $\mathcal{H}_{\text{ad}}$.

The results show that a non-convex domain can be computed using a convex reference domain. Strong deformations are necessary to resolve the non-convex part and without a projection to the admissible set $\mathcal{H}_{\text{ad}}$, mesh folding can occur for small regularization parameters. The choice of $\tilde{\alpha}$ in the pre-conditioner improves the mesh quality in comparison to the Gauß-Newton method, however more iterations are necessary in (6.6) in this case.

III Fluid-dynamically consistent filtering

As outlined in section 3, distributed flow measurements provide valuable information about simple and complex flows. We propose here a post-processing method which reduces or removes distributed measurement errors to some extent, which are typical for such kind of data. Besides the pure enhancement or smoothing of the available data, we are also interested in additional quantities, like for instance the pressure drop, which can be computed from such kind of measurements [85, 24].

The general approach here is to incorporate a suitable fluid dynamical model into a reconstruction process. As we have seen before, using the stationary Navier-Stokes equations as a physical model in combination with Tikhonov regularization leads to a nonlinear optimal control problem. We therefore introduce a linearized flow model which directly incorporates the available data. Using this model, we formulate the corresponding reconstruction method as a linear optimal control problem which is thoroughly analyzed. For comparison, we also comment on the smoothing and solenoidal filter outlined in section 3. Finally, we show some numerical examples which support our theoretical findings. We proceed here closely along the results presented in [24].

9 Modeling of incompressible flow

In order to find a suitable flow model for the reconstruction process, we discuss to some extent the modeling of incompressible fluid flow. While a complete treatment is clearly out of scope here, we rather refer to various available textbooks, like e.g. [4, 77], on this subject for further reference. Let us fix the geometric setting first. Let $\Omega \subset \mathbb{R}^d$, $d = 2, 3$ be some bounded Lipschitz domain. We assume that the boundary is piecewise smooth and can be split into three distinct parts $\partial\Omega_{in}$, $\partial\Omega_{out}$, and $\partial\Omega_{wall}$, where different boundary conditions will be specified later on.

The equations of motion for an incompressible Newtonian fluid with constant density are given in form of the *Navier-Stokes* equations

$$\begin{aligned} \partial_t u + u \cdot \nabla u - \nu \Delta u + \nabla p &= f \quad \text{in } \Omega, \\ \nabla \cdot u &= 0 \quad \text{in } \Omega, \\ u &= g \quad \text{on } \partial\Omega, \end{aligned}$$

where $\nu > 0$ denotes the viscosity parameter, f an external forcing term, g the boundary data, u the flow velocity and p the pressure field. We use here the usual notation $\mathrm{u} \cdot \nabla \mathrm{u} = \sum_j \mathrm{u}_j \partial_j \mathrm{u}_i$. Note that in the case of pure Dirichlet boundary conditions, the boundary data need to fulfill a compatibility condition due to the divergence constraint, see e.g. [80]. The Navier-Stokes equations are far from being a general model, but are accepted to yield a suitable model in a wide range of applications [4, 77]. Note that the global existence of strong solutions of the Navier-Stokes equations is one of the millennium problems of the Clay Mathematics Institute [15].

Oseen problem. As mentioned before, we employ some problem dependent simplifications. First of all, since distributed measurements usually acquire time averaged quantities, we restrict our self to the stationary case. This does, however, not remove the possible ill-posedness. The opposite is true in some sense, as the stationary Navier-Stokes equations are known to admit bifurcation for large data and consequently, a unique solution does not exist in this case [34].

Let us note that the restriction to two dimensions or a smallness condition on the data does guarantee the existence of a unique solution [80]. Both strategies are rather restrictive and we pursue another strategy to get a well-posed problem, namely a linearization. A well-known linear version of the Navier-Stokes equations are the so called *Oseen equations*. For some given background flow field w the stationary Oseen equations are given as

$$-\nu \Delta \mathrm{u} + (\mathrm{w} \cdot \nabla)\mathrm{u} + \nabla \mathrm{p} = \mathrm{f} \quad \text{in } \Omega, \tag{9.1a}$$

$$\nabla \cdot \mathrm{u} = \mathrm{g} \quad \text{in } \Omega, \tag{9.1b}$$

$$\mathrm{u} = 0 \quad \text{on } \partial\Omega. \tag{9.1c}$$

Note that we already employed a *homogenization of boundary conditions* here which in general results in a non-zero divergence. Clearly the function w has to be a good approximation of the true velocity field in order to guarantee that the solution itself is a good approximation. It is well-known [37, 80], that for homogeneous Dirichlet boundary conditions and suitable functions f, g, and w the Oseen equations have a unique weak solution. A possibility to prove such a result is the famous splitting Lemma by Brezzi [11], which is also useful for the numerical analysis of such problems.

Lemma 9.1. *Let X and M be Hilbert spaces and $\alpha, \beta > 0$ two positive constants. Let $a : X \times X \to \mathbb{R}$ be a continuous and elliptic bilinear form, i.e.*

$$a(\mathrm{u}, \mathrm{u}) \geq \alpha \|\mathrm{u}\|_X^2$$

for all $\mathrm{u} \in X$. Further let $b : X \times M \to \mathbb{R}$ be a continuous bilinear form with satisfies the inf-sup condition

$$\inf_{\mathrm{q} \in M} \sup_{\mathrm{v} \in X} \frac{b(\mathrm{v}, \mathrm{q})}{\|\mathrm{v}\|_X \|\mathrm{q}\|_M} \geq \beta. \tag{9.2}$$

Then, the mixed variational problem to find (u, p) such that

$$\begin{aligned} a(\mathrm{u}, \mathrm{v}) + b(\mathrm{v}, \mathrm{p}) &= \langle l, \mathrm{v} \rangle \,, \\ b(\mathrm{u}, \mathrm{q}) &= \langle r, \mathrm{q} \rangle \,, \end{aligned}$$

for all $\mathrm{v} \in X$ and $\mathrm{q} \in M$ has a unique solution $(\mathrm{u}, \mathrm{p}) \in X \times M$ for any linear functionals $l \in X^*$ and $r \in M^*$. Further, the solution (u, p) satisfies the estimate

$$\|\mathrm{u}\|_X + \|\mathrm{p}\|_M \leq C \Big(\|l\|_{X^*} + \|r\|_{M^*} \Big).$$

Proof. For a proof of this famous result, we refer to e.g. [11, 37, 8]. □

The weak formulation of the Oseen equations (9.1a)–(9.1c) with homogeneous boundary conditions is to find (u, p) which fulfills the weak form

$$\begin{aligned} \nu \int_\Omega \nabla \mathrm{u} \nabla \mathrm{v} + \int_\Omega (\mathrm{w} \cdot \nabla) \mathrm{u} \mathrm{v} - \int_\Omega (\nabla \cdot \mathrm{v}) \mathrm{p} \; &= \int_\Omega \mathrm{f} \mathrm{v}, \\ - \int_\Omega (\nabla \cdot \mathrm{u}) \mathrm{q} &= \int_\Omega \mathrm{g} \mathrm{q}, \end{aligned}$$

for all $\mathrm{v} \in H^1(\Omega)$ and $\mathrm{q} \in L^2(\Omega)$. Note that the weak form of the divergence operator fulfills the required *inf-sup condition* (9.2). In order to show that the bilinear form $\nu \int_\Omega \nabla \mathrm{u} \nabla \mathrm{v} + \int_\Omega \mathrm{w} \cdot \nabla \mathrm{u} \mathrm{v}$ induced by the Laplace operator and the convective term is elliptic, we use the fact that $\nabla \cdot \mathrm{w} = 0$ to compute

$$\int_\Omega \mathrm{w} \cdot \nabla \mathrm{u} \mathrm{u} = 0$$

if $\mathrm{u} \cdot \mathrm{n} = 0$ on $\partial\Omega$. The coercivity then follows from Poincaré's inequality. To show continuity, a certain smoothness of w is also required.

Since we have distributed measurements available, our strategy is to use $w = u^\delta$ as background velocity. However, we may not expect u^δ to be smooth or divergence free in general. Therefore, we propose a slightly different linearization strategy suited for such non-smooth data.

9.1 A linearized flow model

In this section, we replace the nonlinear convective term in the Navier-Stokes equations by a suitable expression involving the measurements u^δ to derive a linear flow model. However, since the data u^δ are obtained by measurements, we generally have to assume that $\nabla \cdot u^\delta \neq 0$. Consequently, we cannot simply substitute $w = u^\delta$ in the momentum equation (9.1a). Let us recall that in a weak formulation this would lead to a bilinear form

$$a(u, v) = \nu \int_\Omega \nabla u \nabla v + \int_\Omega (u^\delta \cdot \nabla) uv$$

which together with the weak form of the divergence operator yields a mixed variational problem, see e.g. [37]. As discussed above, the bilinear form $a(u, v)$ is elliptic if the background velocity $w = u^\delta$ is divergence free. Since this is not true here, ellipticity can in general not be shown. Recall the simple identity

$$(w \cdot \nabla)u = \tfrac{1}{2}(w \cdot \nabla)u + \tfrac{1}{2}\mathrm{div}(u \otimes w) - \tfrac{1}{2}(\nabla \cdot w)u,$$

where $\mathrm{div}(u \otimes w) = \sum_j \partial_j (u_i w_j)$ as usual. For an incompressible fluid, i.e. a divergence free velocity field w, we can rewrite the convective term $(w \cdot \nabla)u$ equivalently as $\frac{1}{2}(w \cdot \nabla)u + \frac{1}{2}\mathrm{div}(u \otimes w)$. If we use this special form of the convective term, a short calculation shows that it gives an anti-symmetric contribution in a weak formulation even if $\nabla \cdot w \neq 0$. Consequently, the negative effect on the a priori estimate, as described above, does not occur. Note that such a form of the convective term is sometimes employed in the design and analysis of numerical methods since the discrete approximations are also not exactly divergence free in many cases [8, 37].

Using the available measurements u^δ for linearization of the Navier-Stokes equations, leads to the linearized flow model

$$-\nu \Delta u + \tfrac{1}{2}(u^\delta \cdot \nabla)u + \tfrac{1}{2}\mathrm{div}(u \otimes u^\delta) + \nabla p = f \qquad \text{in } \Omega, \tag{9.3a}$$

$$\nabla \cdot u = 0 \qquad \text{in } \Omega. \tag{9.3b}$$

For a complete description of the flow model we additionally impose the following boundary conditions

$$\mathrm{u} = \mathrm{g} \qquad \text{on } \partial\Omega_{in}, \tag{9.3c}$$
$$\mathrm{u} = 0 \qquad \text{on } \partial\Omega_{wall}, \tag{9.3d}$$
$$(-\nu\nabla\mathrm{u} + \tfrac{1}{2}\mathrm{u}\otimes\mathrm{u}^{\delta} + \mathrm{pI})\cdot\mathrm{n} = \mathrm{h} \qquad \text{on } \partial\Omega_{out}. \tag{9.3e}$$

Here, I denotes the identity matrix and n the outer normal vector on $\partial\Omega_{out}$. The data f, g and h are assumed to be given functions.

Existence of a unique solution. Using standard results [37, 80] and the special form of the convective term, we can now, as a first step, establish the well-posedness of the linearized flow model.

Theorem 9.2 ([24, Theorem 2.1])**.** *Let* $\mathrm{u}^{\delta} \in L^3(\Omega)$*. Then for any* $\mathrm{f} \in L^2(\Omega)$*,* $\mathrm{g} \in H^1_0(\partial\Omega_{in})$*, and* $\mathrm{h} \in L^2(\partial\Omega_{out})$*, the problem* (9.3a)–(9.3e) *has a unique weak solution* $\mathrm{u} \in H^1(\Omega)$ *and* $\mathrm{p} \in L^2(\Omega)$*. Moreover,*

$$\|\mathrm{u}\|_{H^1(\Omega)} + \|\mathrm{p}\|_{L^2(\Omega)} \leq C\big(\|\mathrm{f}\|_{L^2(\Omega)} + \|\mathrm{g}\|_{H^1(\partial\Omega_{in})} + \|\mathrm{h}\|_{L^2(\partial\Omega_{out})}\big)$$

with C depending only on $\|\mathrm{u}^{\delta}\|_{L^3}$*, on the parameter* ν*, and on the geometry.*

Proof. The result follows from an application of Lemma 9.1 and we verify the assumptions. For a more detailed proof for the standard Oseen equations, we refer to e.g. [80, Ch. II] where similar arguments are used.

The weak solution of problem (9.3a)–(9.3e) is characterized by the mixed variational problem to find $\mathrm{u} \in H^1(\Omega)$ and $\mathrm{p} \in L^2(\Omega)$ with $\mathrm{u} = \mathrm{g}$ on $\partial\Omega_{in}$ and $\mathrm{u} = 0$ on $\partial\Omega_{wall}$ such that

$$\tilde{a}(\mathrm{u},\mathrm{v}) + c(\mathrm{u}^{\delta};\mathrm{u},\mathrm{v}) + b(\mathrm{v},\mathrm{p}) = (\mathrm{f},\mathrm{v})_{\Omega} + (\mathrm{h},\mathrm{v})_{\partial\Omega_{out}} \tag{9.4}$$
$$b(\mathrm{u},\mathrm{q}) = 0 \tag{9.5}$$

for all $\mathrm{v} \in H^1(\Omega)$ and $\mathrm{q} \in L^2(\Omega)$ with $\mathrm{v} = 0$ on $\partial\Omega_{wall} \cup \partial\Omega_{in}$. Here, we denote

$$\begin{aligned} \tilde{a}(\mathrm{u},\mathrm{v}) &= \nu(\nabla\mathrm{u},\nabla\mathrm{v})_{\Omega} \\ b(\mathrm{u},\mathrm{q}) &= -(\nabla\cdot\mathrm{u},\mathrm{q})_{\Omega} \quad \text{and} \\ c(\mathrm{u}^{\delta};\mathrm{u},\mathrm{v}) &= \tfrac{1}{2}(\mathrm{u}^{\delta}\cdot\nabla\mathrm{u},\mathrm{v})_{\Omega} - \tfrac{1}{2}(\mathrm{u},\mathrm{u}^{\delta}\cdot\nabla\mathrm{v})_{\Omega} \end{aligned}$$

the bilinear form for the viscous term, the weak form for the divergence operator, and the convective term, respectively.

To apply Lemma 9.1, we construct a function $u_g \in H^1(\Omega)$ which satisfies the Dirichlet boundary conditions (9.3c)–(9.3d) and $\operatorname{div} u_g = 0$. We set $u = u_0 + u_g$, then u_0 fulfills a problem of the form

$$\begin{aligned} a(u_0, v) + b(v, p) &= \langle \tilde{f}, v \rangle \\ b(u_0, q) &= 0 \end{aligned}$$

with $a(u_0, v) = \tilde{a}(u_0, v) + c(u^\delta; u_0, v)$ and

$$\langle \tilde{f}, v \rangle = (f, v)_\Omega + (h, v)_{\partial\Omega_{out}} - \tilde{a}(u_g, v) - c(u^\delta; u_g, v).$$

Using $v = u_0$ as a test function, we have

$$a(u_0, u_0) = \tilde{a}(u_0, u_0) + c(u^\delta, u_0, u_0) = \tilde{a}(u_0, u_0) \geq \alpha \|u_0\|^2_{H^1(\Omega)}$$

From Lemma 9.1, we infer the existence of a unique solution which satisfies

$$\|u\|_{H^1(\Omega)} + \|p\|_{L^2(\Omega)} \leq C\|\tilde{f}\|_{H^{-1}(\Omega)} \leq C\big(\|f\|_{L^2(\Omega)} + \|g\|_{H^1(\partial\Omega_{in})} + \|h\|_{L^2(\partial\Omega_{out})}\big)$$

with C depending only on $\|u^\delta\|_{L^3}$, on the parameter ν, and on the geometry. Here, we used the assumption $u^\delta \in L^3(\Omega)$ to show that $c(u^\delta; u, v)$ is bounded for $u, v \in H^1(\Omega)$. □

Let us note that in practice the available velocity measurements will be bounded, i.e. $u^\delta \in L^\infty(\Omega)$. Therefore, the technical assumption $u^\delta \in L^3(\Omega)$ is usually fulfilled since Ω is a bounded domain.

9.2 Estimates for the linearization error

As a next step, we estimate the error inferred from the velocity field u^δ in the solution of problem (9.3a)–(9.3e). We will show that this error consists of two contributions, i.e. a *data error* and a *modeling error*.

In the following, we denote by $u^\dagger$ and $p^\dagger$ the true velocity and pressure fields. Further, let us assume that these unknown quantities are sufficiently smooth. Then, there exists a function $f^\dagger$ such that

$$-\nu\Delta u^\dagger + \tfrac{1}{2}u^\dagger \cdot \nabla u^\dagger + \tfrac{1}{2}\mathrm{div}(u^\dagger \otimes u^\dagger) + \nabla p^\dagger = f^\dagger \quad \text{in } \Omega, \tag{9.6a}$$

$$\nabla \cdot u^\dagger = 0 \quad \text{in } \Omega. \tag{9.6b}$$

In a similar way, we can define functions $g^\dagger$ and $h^\dagger$ such that

$$u^\dagger = g^\dagger \quad \text{on } \partial\Omega_{in}, \tag{9.6c}$$

$$u^\dagger = 0 \quad \text{on } \partial\Omega_{wall}, \tag{9.6d}$$

$$(-\nu\nabla u^\dagger + \tfrac{1}{2}u^\dagger \otimes u^\dagger + p^\dagger I) \cdot n = h^\dagger \quad \text{on } \partial\Omega_{out}. \tag{9.6e}$$

Since $u^\dagger$ and $p^\dagger$ are unknown, the exact data $f^\dagger$, $g^\dagger$ and $h^\dagger$ are also not known here and describe unmodeled effects like e.g. a time dependence and non Newtonian or turbulent behavior. Now, this system has the same form as (9.3a)–(9.3e) where the data are replaced appropriately. Consequently, we can simply subtract both quantities and estimate their difference.

Theorem 9.3 ([24, Theorem 2.2]). *Let $u^\delta \in L^3(\Omega)$ and let (u, p) and $(u^\dagger, p^\dagger)$ satisfy* (9.3a)–(9.3e) *and* (9.6a)–(9.6e) *respectively. Then,*

$$\|u - u^\dagger\|_{H^1(\Omega)} + \|p - p^\dagger\|_{L^2(\Omega)} \leq C\|u^\dagger - u^\delta\|_{L^3(\Omega)} \tag{9.7a}$$

$$+ C\big(\|f - f^\dagger\|_{L^2(\Omega)} + \|g - g^\dagger\|_{H^1(\partial\Omega_{in})} + \|h - h^\dagger\|_{L^2(\partial\Omega_{out})}\big) \tag{9.7b}$$

with C depending only on the bounds for the data, the parameter ν, and the geometry.

Proof. Let $(\widetilde{u}, \widetilde{p})$ be the solution of problem (9.3a)–(9.3e) with u^δ replaced by $u^\dagger$. Then, we may write

$$u - u^\dagger = w + z \qquad \text{and} \qquad p - p^\dagger = \pi + \psi,$$

with functions $w = u - \widetilde{u}$, $\pi = p - \widetilde{p}$, $z = \widetilde{u} - u^\dagger$, and $\psi = \widetilde{p} - p^\dagger$ that can be estimated separately. From the definition of w and π, we observe that $w = 0$ on $\partial\Omega_{in} \cup \partial\Omega_{wall}$ and

$$a(w, v) + c(u^\delta; w, v) + b(v, \pi) = c(u^\dagger - u^\delta; \widetilde{u}, v)$$

$$b(w, q) = 0$$

for all $v \in H^1(\Omega)$ and $q \in L^2(\Omega)$ with $v = 0$ on $\partial\Omega_{wall} \cup \partial\Omega_{in}$. Choosing $v = w$ and $q = -\pi$ as test functions and applying the Poincaré-Friedrichs inequality, we have

$$\begin{aligned} c\|w\|^2_{H^1(\Omega)} \leq a(w,w) &= a(w,w) + c(u^\delta; w, w) + b(w,\pi) \\ &= c(u^\dagger - u^\delta; \widetilde{u}, w) \leq C\|u^\dagger - u^\delta\|_{L^3(\Omega)}\|\widetilde{u}\|_{H^1(\Omega)}\|w\|_{H^1(\Omega)}. \end{aligned}$$

Since $\|\widetilde{u}\|_{H^1(\Omega)}$ can be bounded uniformly by Theorem 9.2, we further obtain $\|w\|_{H^1(\Omega)} \leq C'\|u^\dagger - u^\delta\|_{L^3(\Omega)}$ and $\|\pi\|_{L^2(\Omega)}$ can be bounded by $\|w\|_{H^1(\Omega)}$ as well with the usual arguments. Next, we observe that $z = g - g^\dagger$ on $\partial\Omega_{in}$ and $z = 0$ on $\partial\Omega_{wall}$, and that

$$\begin{aligned} a(z,v) + c(u^\dagger; z, v) + b(v,\psi) &= (f - f^\dagger, v)_\Omega + (h - h^\dagger, v)_{\partial\Omega_{out}} \\ b(z,q) &= 0 \end{aligned}$$

for all test functions $q \in L^2(\Omega)$ and $v \in H^1(\Omega)$ with $v = 0$ on $\partial\Omega_{wall} \cup \partial\Omega_{in}$. Using Theorem 9.2 we thus obtain $\|z\|_{H^1(\Omega)} + \|\psi\|_{L^2(\Omega)} \leq C''\big(\|f - f^\dagger\|_{L^2(\Omega)} + \|g - g^\dagger\|_{H^1(\partial\Omega_{in})} + \|h - h^\dagger\|_{L^2(\partial\Omega_{out})}\big)$. The assertion of Theorem 9.3 then follows by a combination of these estimates. □

Remark. The estimate (9.7a)–(9.7b) shows that the reconstruction error is composed of two different error contributions. The *data error* $\|u^\dagger - u^\delta\|_{L^3(\Omega)}$ depends on the given measurements, and the *modeling error*

$$\|f - f^\dagger\|_{L^2(\Omega)} + \|g - g^\dagger\|_{H^1(\partial\Omega_{in})} + \|h - h^\dagger\|_{L^2(\partial\Omega_{out})} \tag{9.8}$$

measures the deviation from the "correct" fluid flow model (9.6a)–(9.6e). Therefore, a suitable model describing the flow situation under investigation is a main ingredient for the design of the reconstruction method. Both error contributions will also be present in the error estimates for the reconstruction method.

10 The reconstruction method

In the previous section, we introduced and analyzed a suitable linearized flow model including the noisy measurement data. This enables us to formulate a reconstruction approach similar to those outlined in section 3. The resulting *fluid-dynamically consistent* filter takes the form of the optimal control problem

$$\min_{(\mathrm{f},\mathrm{g},\mathrm{h},\mathrm{u},\mathrm{p})\in V} \quad \|\mathrm{u}-\mathrm{u}^{\delta}\|^2_{L^2(\Omega)} + \alpha\mathcal{R}(\mathrm{f},\mathrm{g},\mathrm{h}) \tag{10.1a}$$

$$\text{s.t. (9.3a)} - \text{(9.3e)}, \tag{10.1b}$$

where $V = L^2(\Omega)\times H^1(\partial\Omega_{in})\times L^2(\partial\Omega_{out})\times H^1(\Omega)\times L^2(\Omega)$ and

$$\mathcal{R}(\mathrm{f},\mathrm{g},\mathrm{h}) = \|\mathrm{f}-\mathrm{f}^*\|^2_{L^2(\Omega)} + \|\mathrm{g}-\mathrm{g}^*\|^2_{H^1(\partial\Omega_{in})} + \|\mathrm{h}-\mathrm{h}^*\|^2_{L^2(\partial\Omega_{out})}. \tag{10.2}$$

Here, we introduced the additional model parameters f^*, g^*, and h^*, which should approximate the exact model data $\mathrm{f}^\dagger$, $\mathrm{g}^\dagger$, and $\mathrm{h}^\dagger$.

We note that problem (10.1a)–(10.1b) can be considered as a linearization of the nonlinear fluid-dynamically consistent filter outlined in section 3. A further possible interpretation is as follows. Besides a deviation from the given velocity data, also the deviation from a prescribed flow model is penalized in form of a weighted sum. The choice of the regularization parameter α allows us to balance those two error contributions.

10.1 Existence of a unique minimizer

In order to apply standard results, as outlined in section 4, we transform problem (10.1a)–(10.1b) equivalently to a reduced problem. Let us denote by $\mathrm{u} = \mathrm{u}(\mathrm{f},\mathrm{g},\mathrm{h})$ and $\mathrm{p} = \mathrm{p}(\mathrm{f},\mathrm{g},\mathrm{h})$ the unique solution of the linearized flow model (9.3a)–(9.3e). Then, the reduced problem takes the form of the quadratic minimization problem

$$\min_{(\mathrm{f},\mathrm{g},\mathrm{h})\in V_{red}} J_\alpha(\mathrm{f},\mathrm{g},\mathrm{h}), \tag{10.3}$$

where $V_{red} = L^2(\Omega)\times H^1(\partial\Omega_{in})\times L^2(\partial\Omega_{out})$ and

$$J_\alpha(\mathrm{f},\mathrm{g},\mathrm{h}) = \|\mathrm{u}(\mathrm{f},\mathrm{g},\mathrm{h})-\mathrm{u}^{\delta}\|^2_{\mathrm{L}^2(\Omega)} + \alpha\mathcal{R}(\mathrm{f},\mathrm{g},\mathrm{h})$$

denotes the reduced cost functional. The functions u and p have been formally eliminated and the functions f, g, and h are the only remaining unknowns. Using the formulation (10.3), we can show the existence of a unique minimizer along the usual arguments. Due to the equivalence with the problem (10.1a)–(10.1b), the result directly transfers to the original formulation.

Theorem 10.1 ([24, Theorem 3.1])**.** *Let* $u^\delta \in L^3(\Omega)$ *and let* $f^* \in L^2(\Omega)$, $g^* \in H_0^1(\partial\Omega_{in})$ *and* $h^* \in L^2(\partial\Omega_{out})$*. Then, for any regularization parameter* $\alpha > 0$ *the reduced minimization problem* (10.3) *has a unique solution with components* $f_\alpha \in L^2(\Omega)$, $g_\alpha \in H_0^1(\partial\Omega_{in})$*, and* $h_\alpha \in L^2(\partial\Omega_{out})$*. Together with* $u_\alpha = u(f_\alpha, g_\alpha, h_\alpha)$ *and* $p_\alpha = p(f_\alpha, g_\alpha, h_\alpha)$*, this yields the unique solution of problem* (10.1a)–(10.1b)*.*

Proof. For the proof we use the usual arguments for the existence of a minimizer of infinite dimensional optimization problems [51, 60]. The mapping

$$(f, g, h) \mapsto (u(f, g, h), p(f, g, h))$$

is affine linear and continuous. Since the functional J_α is bounded from below, quadratic and strictly convex, the infimum exists together with a bounded minimizing sequence. From its continuity and convexity, we have that J_α is weakly lower semi-continuous. Therefore, we can select a weakly convergent subsequence, and the limit of this sequence is indeed a minimizer. Due to the linearity of the forward mapping, the minimizer is also unique. □

10.2 Estimates for the reconstruction error

It remains to clarify if the velocity and pressure fields (u_α, p_α) computed from the minimizer of (10.3) serve as an approximation of the true quantities $u^\dagger$ and $p^\dagger$. Therefore, we derive some quantitative estimates for this *reconstruction error*. As already discussed, the true velocity and pressure fields $(u^\dagger, p^\dagger)$ satisfy a system of equations similar to the linear flow model (9.3a)–(9.3e). We may therefore utilize the estimates for the linearization error in Theorem 9.3 in the following way.

Theorem 10.2 ([24, Theorem 3.2])**.** *Let* (u_α, p_α) *denote the velocity and pressure components of the unique solution of problem* (10.1a)–(10.1b) *and assume that* $\|u^\dagger - u^\delta\|_{L^3(\Omega)} \leq \delta$*. Then, the following estimates hold true:*

(i) $\|u_\alpha - u^\dagger\|^2_{L^2(\Omega)} \leq C\delta^2 + \alpha\mathcal{R}(f^\dagger, g^\dagger, h^\dagger)$

(ii) $\|u_\alpha - u^\dagger\|^2_{H^1(\Omega)} + \|p_\alpha - p^\dagger\|^2_{L^2(\Omega)} \le C\delta^2 + \delta^2/\alpha + C\mathcal{R}(f^\dagger, g^\dagger, h^\dagger)$

with $\mathcal{R}$ *defined in* (10.2).

Proof. Let $(\widehat{u}, \widehat{p})$ denote the solution of (9.4)–(9.5) with f, g, h replaced by $f^\dagger$, $g^\dagger$, and $h^\dagger$, respectively. Then, following the estimate for the function w in the proof of Theorem 9.3, we have

$$\|\widehat{u} - u^\dagger\|_{H^1(\Omega)} + \|\widehat{p} - p^\dagger\|_{L^2(\Omega)} \le C\|u^\dagger - u^\delta\|_{L^3(\Omega)}.$$

By definition of u_α as a minimizer, we further have

$$\begin{aligned}
&\|u_\alpha - u^\delta\|^2_{L^2(\Omega)} \\
&\le \|u_\alpha - u^\delta\|^2_{L^2(\Omega)} + \alpha\big(\|f_\alpha - f^*\|^2_{L^2(\Omega)} + \|g_\alpha - g^*\|^2_{H^1(\partial\Omega_{in})} + \|h_\alpha - h^*\|^2_{L^2(\partial\Omega_{out})}\big) \\
&\le \|\widehat{u} - u^\delta\|^2_{L^2(\Omega)} + \alpha\big(\|f^\dagger - f^*\|^2_{L^2(\Omega)} + \|g^\dagger - g^*\|^2_{H^1(\partial\Omega_{in})} + \|h^\dagger - h^*\|^2_{L^2(\partial\Omega_{out})}\big).
\end{aligned}$$

The first assertion now follows by combining the two estimates and using the assumption on the data error together with the continuous embedding of $L^3(\Omega)$ into $L^2(\Omega)$ on bounded domains. For the second estimate, we use the triangle inequality to obtain

$$\begin{aligned}
&\|u_\alpha - u^\dagger\|_{H^1(\Omega)} + \|p_\alpha - p^\dagger\|_{L^2(\Omega)} \\
&\le (\|\widehat{u} - u^\dagger\|_{H^1(\Omega)} + \|\widehat{p} - p^\dagger\|_{L^2(\Omega)}) + (\|u_\alpha - \widehat{u}\|_{H^1(\Omega)} + \|p_\alpha - \widehat{p}\|_{L^2(\Omega)}).
\end{aligned}$$

The first term can be estimated by $\|\widehat{u} - u^\dagger\|_{H^1(\Omega)} + \|p_\alpha - \widehat{p}\|_{L^2(\Omega)} \le C\delta$ as above. Proceeding as in the proof of Theorem 9.2, the remaining term can be bounded by

$$\begin{aligned}
&\|u_\alpha - \widehat{u}\|_{H^1(\partial\Omega)} + \|p_\alpha - \widehat{p}\|_{L^2(\Omega)} \\
&\le C\big(\|f_\alpha - f^\dagger\|_{L^2(\Omega)} + \|g_\alpha - g^\dagger\|_{H^1(\partial\Omega_{in})} + \|h_\alpha - h^\dagger\|_{L^2(\partial\Omega_{out})}\big).
\end{aligned}$$

Let us consider the first term on the right-hand side in more detail. Using the triangle inequality, we can see that

$$\|f_\alpha - f^\dagger\|_{L^2(\Omega)} \le \|f_\alpha - f^*\|_{L^2(\Omega)} + \|f^\dagger - f^*\|_{L^2(\Omega)}.$$

Since the second term already appears in the final result, it remains to estimate $\|f_\alpha - f^*\|_{L^2(\Omega)}$. From the definition of the minimizers, we have that

$$\begin{aligned}
&\|f_\alpha - f^*\|^2_{L^2(\Omega)} \\
&\leq \alpha^{-1}\|u_\alpha - u^\delta\|^2_{L^2(\Omega)} + \|f_\alpha - f^*\|^2_{L^2(\Omega)} + \|g_\alpha - g^*\|^2_{H^1(\partial\Omega_{in})} + \|h_\alpha - h^*\|^2_{L^2(\partial\Omega_{out})} \\
&\leq \alpha^{-1}\|\hat{u} - u^\delta\|^2_{L^2(\Omega)} + \|f^\dagger - f^*\|^2_{L^2(\Omega)} + \|g^\dagger - g^*\|^2_{H^1(\partial\Omega_{in})} + \|h^\dagger - h^*\|^2_{L^2(\partial\Omega_{out})}.
\end{aligned}$$

Together with the estimates for $\hat{u} - u^\dagger$ and the bound on the data error, this yields

$$\begin{aligned}
\|f_\alpha - f^*\|^2_{L^2(\Omega)} &\leq C\big(\delta^2/\alpha\big) \\
&\quad + C\big(\|f^\dagger - f^*\|^2_{L^2(\Omega)} + \|g^\dagger - g^*\|^2_{H^1(\partial\Omega_{in})} + \|h^\dagger - h^*\|^2_{L^2(\partial\Omega_{out})}\big).
\end{aligned}$$

The same arguments allow to determine estimates for $\|g_\alpha - g^*\|^2_{H^1(\partial\Omega_{in})}$ and $\|h_\alpha - h^*\|_{L^2(\partial\Omega_{out})}$ which completes the proof. □

The estimates in Theorem 10.2 show that the reconstruction error, similar to the linearization error, is composed of two contributions. The regularization parameter α balances the data error and the modeling error. If it is chosen sufficiently small, a good fit to the measurement data can always be guaranteed. The estimate (ii) in Theorem 10.2 shows a blow-up behavior if α goes to zero. Choosing the regularization parameter in a proper way, we have a $\mathcal{O}(\delta)$ convergence which is optimal compared to the usually expected rates [27].

Remark. If the proposed flow model is a good description of the physical conditions, i.e., if the modeling errors $\|f^\dagger - f^*\|$, $\|g^\dagger - g^*\|$, and $\|h^\dagger - h^*\|$ are sufficiently small, we may choose the regularization parameter in the order of one and still obtain a good fit for the velocity and pressure fields. Therefore, we expect a certain robustness with respect to the regularization parameter, which will also be demonstrated by numerical tests.

Further properties. We note that the functional J and also the data residuals $\|u_\alpha - u^\delta\|_{L^2(\Omega)}$ for the optimal values decrease with the regularization parameter α, which will be useful later for the automated choice of a regularization parameter. Such a result is typical for Tikhonov regularization [27].

Lemma 10.3. *Let J_α be defined as above. Then, whenever $\alpha \leq \beta$,*

$$\min_{f,g,h} J_\alpha(f,g,h) \leq \min_{f,g,h} J_\beta(f,g,h) \quad \textit{and}$$
$$\|u_\alpha - u^\delta\|_{L^2(\Omega)} \leq \|u_\beta - u^\delta\|_{L^2(\Omega)}.$$

Proof. By definition of f_α, g_α and h_α as minimizer, and since $\alpha \leq \beta$ we have

$$J_\alpha(f_\alpha, g_\alpha, h_\alpha) \leq J_\alpha(f_\beta, g_\beta, h_\beta) \leq J_\beta(f_\beta, g_\beta, h_\beta),$$

where we used the positivity of the regularization term for the second inequality. This already shows the first assertion. Similar to the first inequality above, we have

$$J_\beta(f_\beta, g_\beta, h_\beta) \leq J_\beta(f_\alpha, g_\alpha, h_\alpha).$$

Adding both inequalities shows that the regularization terms are monotonically decreasing with α, since after some simple modifications we have

$$\begin{aligned}(\beta-\alpha)\big\{&\|f_\beta - f^*\|^2_{L^2(\Omega)} + \|g_\beta - g^*\|^2_{H^1(\partial\Omega_{in})} + \|h_\beta - h^*\|^2_{L^2(\partial\Omega_{out})}\big\}\\ \leq(\beta-\alpha)\big\{&\|f_\alpha - f^*\|^2_{L^2(\Omega)} + \|g_\alpha - g^*\|^2_{H^1(\partial\Omega_{in})} + \|h_\alpha - h^*\|^2_{L^2(\partial\Omega_{out})}\big\}.\end{aligned}$$

The second assertion then follows from a combination of the previous estimates. □

Remark. Since for $\alpha \to 0$ the data residuals $\|u_\alpha - u^\delta\|_{L^2(\Omega)}$ decrease monotonically, this allows us to choose the regularization parameter α via a *discrepancy principle* [27, 54] in order to obtain the desired rate in the reconstruction error, see also section 12.2.

10.3 Iterated filtering

So far we discussed a fluid-dynamically consistent filtering strategy which computes a smooth and divergence free reconstruction from given measurements. Since those data are not smooth and also not divergence free, we proposed a suitable linearization strategy to incorporate such data. Even though the proposed filter already has some smoothing effect, the noise in the data transfers in some sense to the reconstruction. Proceeding in an iterated manner, we might reuse the smoothed velocity field u^δ_α as a substitute for the measurements.

Let u_α^δ denote the velocity field reconstructed by (10.1a)–(10.1b). Then, an iterated filtering approach has the form

$$\min_{(f,g,h)\in V_{red}} \quad \|u(f,g,h) - u^\delta\|^2_{L^2(\Omega)} + \alpha\mathcal{R}(f,g,h) \tag{10.4a}$$

where $V_{red} = L^2(\Omega) \times H^1(\partial\Omega_{in}) \times L^2(\partial\Omega_{out})$ as before, and $u(f,g,h)$, together with $p(f,g,h)$, denotes the unique solution of

$$\begin{aligned}
-\nu\Delta u + \tfrac{1}{2}(u_\alpha^\delta \cdot \nabla)u + \tfrac{1}{2}\mathrm{div}(u \otimes u_\alpha^\delta) + \nabla p &= f \qquad \text{in } \Omega, && (10.4b)\\
\nabla \cdot u &= 0 \qquad \text{in } \Omega, && (10.4c)\\
u &= g \qquad \text{on } \partial\Omega_{in}, && (10.4d)\\
u &= 0 \qquad \text{on } \partial\Omega_{wall}, && (10.4e)\\
(-\nu\nabla u + \tfrac{1}{2}u \otimes u_\alpha^\delta + pI) \cdot n &= h \qquad \text{on } \partial\Omega_{out}. && (10.4f)
\end{aligned}$$

This has several advantages. First of all, the smoothed velocity field u_α^δ is divergence free due to its construction. This means that the anti-symmetric splitting is exact in the sense that

$$\tfrac{1}{2}(u_\alpha^\delta \cdot \nabla)u + \tfrac{1}{2}\nabla \cdot (u \otimes u_\alpha^\delta) = u_\alpha^\delta \cdot \nabla u,$$

at least for the infinite dimensional formulation. Note that for the discrete reconstruction we merely obtain that the discrete divergence is zero and therefore, the anti-symmetric convection term in (10.4b) is reasonable here.

Further, we have a smooth background velocity, i.e. $u_\alpha^\delta \in H^1(\Omega)$, in this case, which fulfills the no-slip boundary condition on $\partial\Omega_{wall}$, as well as approximately the in- and outflow boundary conditions. Similar as for problem (10.1a)–(10.1b) we obtain the following error estimates.

Corollary 10.4. *Let* (u_α, p_α) *denote the velocity and pressure components of the unique solution of problem* (10.4a) *and let* u_α^δ *denote the solution of* (10.1a)–(10.1b)*. Then, the following estimates hold true:*

(i) $\|u_\alpha - u^\dagger\|^2_{L^2(\Omega)} \leq C\delta^2 + \alpha\mathcal{R}(f^\dagger, g^\dagger, h^\dagger)$

(ii) $\|u_\alpha - u^\dagger\|^2_{H^1(\Omega)} + \|p_\alpha - p^\dagger\|^2_{L^2(\Omega)} \leq C\delta^2 + \delta^2/\alpha + C\mathcal{R}(f^\dagger, g^\dagger, h^\dagger)$

with $\mathcal{R}$ *defined in* (10.2).

Proof. The proof is the same as for Theorem 10.2, where we use

$$\|u_\alpha^\delta - u^\dagger\|_{L^2(\Omega)} \leq C\delta. \quad \square$$

Corollary 10.4 shows that such an iterated filtering approach is at least as good as the fluid-dynamically consistent filter with respect to the reconstruction error. We will, however, present numerical examples below, which indicate that such a strategy results in a considerable improvement of the reconstruction already for the second iteration.

Note that such an iterative strategy can also be interpreted as a first step in direction of an Oseen type iteration for the solution of the nonlinear reconstruction problem using the stationary Navier-Stokes equations outlined in section 3. With respect to such an approach the measurements u^δ are then used initial value which should reduce the necessary number of iterations.

10.4 The smoothing and solenoidal filter

For completeness and for further comparison, we discuss the smoothing and solenoidal filter outlined in section 3. While existence and uniqueness of solutions can be shown using exactly the same arguments as in Theorem 10.1, we derive here shortly the corresponding optimality conditions and show a connection of the fluid-dynamically consistent and solenoidal filter.

The smoothing filter. Proceeding in a similar fashion as above, we define a *smoothing filter*. The smoothed velocity field will be the solution of

$$\min_{u \in H^1(\Omega)} \tfrac{1}{2}\|u - u^\delta\|^2_{L^2(\Omega)} + \tfrac{\alpha}{2}\|\nabla u\|^2_{L^2(\Omega)}. \tag{10.5}$$

We have, that the minimizer u_α^{SmF} of this filter is characterized by the variational problem

$$\int_\Omega \alpha \nabla u_\alpha^{SmF} \nabla v + u_\alpha^{SmF} v = \int_\Omega u^\delta v$$

for all $v \in H^1(\Omega)$. This corresponds to the weak formulation of a Laplace problem similar to those discussed in part II.

The solenoidal filter. In the same fashion, the *solenoidal filter* will be defined to compute the minimizer of the constrained minimization problem

$$\min_{u \in H^1(\Omega)} \tfrac{1}{2}\|u - u^\delta\|^2_{L^2(\Omega)} + \tfrac{\alpha}{2}\|\nabla u\|^2_{L^2(\Omega)} \tag{10.6a}$$

$$\text{s.t. } \nabla \cdot u = 0. \tag{10.6b}$$

Similar as before, the minimizer u_α^{SF} is characterized by the mixed variational problem

$$\int_\Omega \alpha \nabla u_\alpha^{SF} \nabla v + u_\alpha^{SF} v - \int_\Omega (\nabla \cdot v) p = \int_\Omega u^\delta v$$
$$- \int_\Omega (\nabla \cdot u_\alpha^{SF}) q = 0,$$

which corresponds to the weak formulation of a Stokes-type problem. The Lagrange multiplier p takes the role of the pressure, however, as our numerical tests will show, it does not approximate the physical pressure. The existence and uniqueness of a solution follows again by the Brezzi splitting Lemma [11] at least for $\alpha > 0$. For the case $\alpha = 0$, the unique minimizer is just given as the solenoidal part of the Helmholtz decomposition [37] of u^δ.

Relation to the fluid-dynamically consistent filter. Let us comment on a connection of the solenoidal and the fluid-dynamically consistent filter. In contrary to the smoothing filter, the divergence free condition is always enforced for those methods.

Theorem 10.5 ([24, Theorem 3.4])**.** *Let* $u_\alpha = u(f_\alpha, g_\alpha, h_\alpha)$ *and* u^{SF} *be the unique minimizer of* (10.3) *and the unique solution of* (10.6a)–(10.6b) *with* $\alpha = 0$ *respectively. Then*

$$\|u_\alpha - u^{SF}\|_{L^2(\Omega)} \to 0,$$

for $\alpha \to 0$.

Proof. To show the assertion, let us note that for any $\varepsilon > 0$ one can find a smooth divergence free approximation $\widetilde{u}^{SF}$ for the velocity field u^{SF} that is obtained by (10.6a)–(10.6b) with $\alpha = 0$ and such that $\|u^{SF} - \widetilde{u}^{SF}\|_{L^2(\Omega)} \leq \varepsilon$. By plugging $\widetilde{u}^{SF}$

into (9.3a)–(9.3e), we obtain the corresponding residuals $\widetilde{f}$, $\widetilde{g}$, and $\widetilde{h}$. Using the definition of u_α, we further get

$$\begin{aligned}
&\|u_\alpha - u^\delta\|^2_{L^2(\Omega)} \\
&\leq \|u_\alpha - u^\delta\|^2_{L^2(\Omega)} + \alpha\big(\|f_\alpha - f^*\|^2_{L^2(\Omega)} + \|g_\alpha - g^*\|^2_{H^1(\partial\Omega_{in})} + \|h_\alpha - g^*\|^2_{L^2(\partial\Omega_{out})}\big) \\
&\leq \|\widetilde{u}^{SF} - u^\delta\|^2_{L^2(\Omega)} + \alpha\big(\|\widetilde{f} - f^*\|^2_{L^2(\Omega)} + \|\widetilde{g} - g^*\|^2_{H^1(\partial\Omega_{in})} + \|\widetilde{h} - h^*\|^2_{L^2(\partial\Omega_{out})}\big).
\end{aligned}$$

This shows that

$$\limsup_{\alpha\to 0} \|u_\alpha - u^\delta\|_{L^2(\Omega)} \leq \|\widetilde{u}^{SF} - u^\delta\|_{L^2(\Omega)} \leq \|u^{SF} - u^\delta\|_{L^2(\Omega)} + \varepsilon$$

for any $\varepsilon > 0$. We therefore conclude that

$$\limsup_{\alpha\to 0} \|u_\alpha - u^\delta\|_{L^2(\Omega)} \leq \|u^{SF} - u^\delta\|_{L^2(\Omega)}.$$

Since $\|u_\alpha\|_{L^2(\Omega)} \leq C$ for all $\alpha > 0$, we can select a subsequence $\{u_{\alpha'}\}$ converging weakly to some $\bar{u} \in L^2(\Omega)$. By the lower semi-continuity of the norm, we can deduce

$$\begin{aligned}
\|\bar{u} - u^\delta\|_{L^2(\Omega)} &\leq \liminf_{\alpha'\to 0} \|u_{\alpha'} - u^\delta\|_{L^2(\Omega)} \\
&\leq \limsup_{\alpha'\to 0} \|u_{\alpha'} - u^\delta\|_{L^2(\Omega)} \leq \|u^{SF} - u^\delta\|_{L^2(\Omega)}.
\end{aligned}$$

Moreover, since $\operatorname{div} u_\alpha = 0$ for all $\alpha > 0$, we also have $\operatorname{div} \bar{u} = 0$. But since u^{SF} is the unique minimizer of (10.6a)–(10.6b), we may conclude that $\bar{u} = u^{SF}$. □

Remark. This result shows that the reconstruction u_α approaches the result for the solenoidal filter without smoothing for $\alpha \to 0$. In some sense the divergence zero condition is the only remaining constraint if the regularization parameter becomes small enough. With respect to this property our method is indeed an extension of the solenoidal filter (10.6a)–(10.6b).

11 Numerical realization

Similar to section 7, we need to discretize the reconstruction methods discussed here in order to get an implementable algorithm. We use again a conforming Galerkin method with finite element basis functions. However, care needs to be taken due to the saddle point structure of the forward problem. We therefore comment shortly on the discretization of flow problems using finite elements. The proposed data filter and also the solenoidal and smoothing filters discussed above can then be discretized systematically. We will comment on the discrete optimality system for these methods which will be the basis for the solution of the corresponding problems.

11.1 Finite elements for saddle-point problems

As discussed before, the forward problem (9.3a)–(9.3e) has the form of a saddle-point problem. In order to derive a finite element discretization of such a problem we can in principle proceed analogously to the techniques presented in section 7. However, care needs to be taken that a discrete version of the inf-sup condition, see Lemma 9.1, is satisfied also on the discrete spaces. Note that this is well-known and we may use any inf-sup stable pair of finite elements spaces, see e.g. [7, 8, 37], in the following.

Let $(\mathcal{T}_h)_{h>0}$ be a family of uniformly shape regular triangulations of Ω. Here, we use first order finite element basis functions for the discretization of the pressure. In order to obtain an inf-sup stable discretization the ansatz space for the velocity has to be chosen appropriately. Here, we use the Mini element [7, 8], i.e. we use the spaces

$$\begin{aligned} U_h &= \Big[\big(\mathrm{P}_1(\mathcal{T}_h)^d \oplus \mathbb{B}(\mathcal{T}_h)\big) \cap \mathcal{C}(\mathrm{R})\Big] \subset H^1(\mathrm{R})^d \quad \text{and} \\ Q_h &= \Big[\mathrm{P}_1(\mathcal{T}_h) \cap \mathcal{C}(\mathrm{R})\Big] \subset H^1(\mathrm{R}), \end{aligned}$$

where $\mathbb{B}(\mathcal{T}_h)$ denotes the usual bubble space, see e.g. [7].

Similar to the procedure in section 7, we can derive a discrete version of (9.3a)–(9.3e) and show existence of a unique solution again using Lemma 9.1. In order to derive a formulation as algebraic problem, we denote by $(\phi_i)_{i=1,\dots,N}$ and

$(\varphi_i)_{i=1,\dots,\tilde{N}}$ a basis of the spaces U_h and Q_h, respectively. Then, we have for any $\mathrm{u}_h \in U_h$ and $\mathrm{p}_h \in Q_h$, that

$$\mathrm{u}_h = \sum_{i=1}^{N} \mathsf{u}_i \phi_i \quad \text{and} \quad \mathrm{p}_h = \sum_{i=1}^{\tilde{N}} \mathsf{p}_i \varphi_i.$$

As before, we denote by

$$\mathsf{K}_{ij} = (\nabla\phi_i, \nabla\phi_j)_{L^2(\mathrm{R})} \quad \text{and} \quad \mathsf{M}_{ij} = (\phi_i, \phi_j)_{L^2(\mathrm{R})}$$

the mass and stiffness matrices on U_h, respectively. The convective term is represented by

$$\mathsf{C}(\mathsf{u}^\delta)_{ij} = \int_\Omega \tfrac{1}{2}\big((\mathrm{u}^\delta \cdot \nabla\phi_i)\phi_j - (\mathrm{u}^\delta \cdot \nabla\phi_j)\phi_i\big),$$

and the vector u^δ denotes the finite element representation of the velocity measurements. Further, the integrals over the boundaries $\partial\Omega_{in} \cup \partial\Omega_{wall}$ and $\partial\Omega_{out}$ are realized by the matrices

$$\mathsf{R}_{ij} = \int_{\partial\Omega_{in}\cup\partial\Omega_{wall}} \phi_i\phi_j \quad \text{and} \quad \mathsf{N}_{ij} = \int_{\partial\Omega_{out}} \phi_i\phi_j.$$

The discrete divergence operator is represented by

$$\mathsf{B}_{ij} = -\int_\Omega (\nabla \cdot \phi_j)\varphi_i.$$

If we use the abbreviation $\mathsf{A} = \nu\mathsf{K} + \mathsf{C}(\mathsf{u}^\delta) + \frac{1}{\varepsilon}\mathsf{R}$ the discretization of the state system (9.3a)–(9.3e) then leads to an algebraic system of the form

$$\mathsf{A}\mathsf{u} + \mathsf{B}^\top\mathsf{p} = \mathsf{M}\mathsf{f} + \tfrac{1}{\varepsilon}\mathsf{R}\mathsf{E}\mathsf{g} + \mathsf{N}\mathsf{h}, \tag{11.1a}$$

$$\mathsf{B}\mathsf{u} = 0, \tag{11.1b}$$

where the Dirichlet boundary conditions are incorporated here by a penalty approach with $\varepsilon > 0$ being a small parameter. The matrix E realizes an extension of boundary values into the domain by zero. As usual, all matrices can be assembled using standard techniques and the results will be sparse. We refer to standard textbooks on the subject like e.g. [37, 80] for further reference.

Note that due to the discrete inf-sup condition, system (11.1a)–(11.1b) has a unique solution. Further, we obtain a discretization error of the form

$$\|\mathrm{u} - \mathrm{u}_h\|_{H^1} + \|\mathrm{p} - \mathrm{p}_h\|_{L^2} = \mathcal{O}(h),$$

see for instance [8].

11.2 Discretization of the reconstruction approach

Using the notation above, we can now derive a discrete version of the optimal control problem (10.1a)–(10.1b), as a next step. We obtain a finite dimensional optimization problem with linear constraints of the form

$$\min_{(\mathsf{u},\mathsf{p},\mathsf{f},\mathsf{g},\mathsf{h})\in V_h} \|\mathsf{u} - \mathsf{u}^\delta\|_{\mathsf{M}}^2 + \alpha\big(\|\mathsf{f} - \mathsf{f}^*\|_{\mathsf{M}}^2 + \|\mathsf{g} - \mathsf{g}^*\|_{\mathsf{G}}^2 + \|\mathsf{h} - \mathsf{h}^*\|_{\mathsf{H}}^2\big) \tag{11.2a}$$

$$\text{s.t. (11.1a)} - \text{(11.1b)}, \tag{11.2b}$$

with $V_h = U_h \times Q_h \times Q_h \times G_h \times H_h$. The discrete spaces G_h and H_h are used for the discretization of g and h and the Gramian matrices G and H induce the corresponding norms on the boundary. Note that the mass matrix M corresponds to the gram matrix of the L^2-norm, as before. Similar to section 7, we have the following result.

Lemma 11.1. *Let* u^δ, f^*, g^*, *and* h^* *denote the finite element representations of* u^δ, f^*, g^*, *and* h^*, *respectively. Then, problem* (11.2a)–(11.2b) *has a unique solution.*

Proof. Problem (11.2a)–(11.2b) is formulated on a finite dimensional space and the functional in (11.2a) is continuous and strictly convex. Further, the constraint (11.1a)-(11.1b) is a linear system of equations. This implies the existence of a unique solution. □

Optimality condition. In order to compute the minimizer of (11.2a)–(11.2b) we will use a so-called all-at-once method [47] here. Following a standard procedure, we differentiate the associated Lagrangian to derive the first order optimality conditions for (11.2a)–(11.2b). This results in the coupled, symmetric, and linear system of equations

$$\begin{bmatrix} -\mathsf{M} & 0 & \mathsf{A}^\top & \mathsf{B}^\top & 0 & 0 & 0 \\ 0 & 0 & \mathsf{B} & 0 & 0 & 0 & 0 \\ \mathsf{A} & \mathsf{B}^\top & 0 & 0 & -\mathsf{M} & -\frac{1}{\varepsilon}\mathsf{RE} & -\mathsf{N} \\ \mathsf{B} & 0 & 0 & 0 & 0 & 0 & 0 \\ 0 & 0 & -\mathsf{M}^\top & 0 & \alpha\mathsf{M} & 0 & 0 \\ 0 & 0 & -\frac{1}{\varepsilon}(\mathsf{RE})^\top & 0 & 0 & \alpha\mathsf{G} & 0 \\ 0 & 0 & -\mathsf{N}^\top & 0 & 0 & 0 & \alpha\mathsf{H} \end{bmatrix} \begin{bmatrix} \mathsf{u} \\ \mathsf{p} \\ \lambda \\ \mu \\ \mathsf{f} \\ \mathsf{g} \\ \mathsf{h} \end{bmatrix} = \begin{bmatrix} -\mathsf{M}\mathsf{u}^\delta \\ 0 \\ 0 \\ 0 \\ \alpha\mathsf{M}\mathsf{f}^* \\ \alpha\mathsf{G}\mathsf{g}^* \\ \alpha\mathsf{H}\mathsf{h}^* \end{bmatrix},$$

where λ and μ denote the Lagrange multipliers for the momentum equation and the divergence constraint, respectively. Note that the resulting discrete optimality system is sparse symmetric and indefinite due to the use of finite elements. Since the optimal control problem under investigation is quadratic and strictly convex, the first-order optimality conditions are necessary and sufficient [51, 60], and the solution of the KKT system is a minimizer.

Other filtering methods. Let us shortly discuss the implementation of the smoothing and solenoidal filtering approaches. To make comparison possible we use the same finite element spaces for the discretization.

The discrete smoothing filter is given as

$$\min_{\mathsf{u}} \|\mathsf{u} - \mathsf{u}^\delta\|_{\mathsf{M}}^2 + \alpha\|\mathsf{u}\|_{\mathsf{K}}^2, \tag{11.3}$$

where we use the same notation as before. The first order optimality condition takes here the form of the regularized normal equations

$$[\mathsf{M} + \alpha\mathsf{K}]\mathsf{u} = \mathsf{M}\mathsf{u}^\delta. \tag{11.4}$$

This system has the same form as the problems discussed in part II and can be solved using the techniques described there.

The solenoidal filtering approach can be discretized in the same fashion. Using again the same notation as above, we have

$$\min_{\mathsf{u}} \|\mathsf{u} - \mathsf{u}^{\delta}\|_{\mathsf{M}}^2 + \alpha \|\mathsf{u}\|_{\mathsf{K}}^2 \qquad \text{s.t. } \mathsf{B}\mathsf{u} = 0. \tag{11.5}$$

Here, the optimality system which can be derived in a similar fashion as before, has the form

$$\begin{bmatrix} (\mathsf{M} + \alpha\mathsf{K}) & \mathsf{B}^{\top} \\ 0 & \mathsf{B} \end{bmatrix} \begin{bmatrix} \mathsf{u} \\ \mu \end{bmatrix} = \begin{bmatrix} \mathsf{M}\mathsf{u}^{\delta} \\ 0 \end{bmatrix}, \tag{11.6}$$

where μ denotes again the Lagrange multiplier for the divergence constraint. Note that this system has a similar structure as the forward problem for the fluid-dynamically consistent filter (11.1a)–(11.1b). The Lagrange multiplier μ takes the role of the pressure p here. Note that an inf-sup stable pair of finite element spaces is necessary here to ensure the existence and uniqueness of the discrete solution.

12 Computational validation

In order to illustrate the properties of the proposed reconstruction approach, we discuss some preliminary computational results. In all simulations, we use a regular tetrahedral mesh on the computational domain and we assume that the measured velocity field u^δ is given at each vertex of the mesh. For the discretization of the flow equations, we use here the Mini element [7, 8]. Other inf-sup stable pairs of finite elements spaces could be used as well.

In order to verify the quantitative estimates of sections 9.2 and 10.2 we discuss the flow through a simple geometry where the exact solution is known. The laminar flow through a channel of length L with triangular cross-section as depicted in Figure 3.1 is described by the pressure and velocity field

$$p^\dagger(x,y,z) = p_0 + \frac{p_L - p_0}{L}x \qquad \text{and} \tag{12.1}$$

$$u^\dagger(x,y,z) = \left(0, 0, \frac{p_L - p_0}{4\nu L}(y-d)(y-\sqrt{3}x)(y+\sqrt{3}x)\right), \tag{12.2}$$

where p_0, p_L denote the pressure at position $z = 0$ and $z = L$, respectively. As computational domain, we choose here $\Omega = T \times (0, L)$, where

$$T = \{(x,y) \in \mathbb{R}^2 : x < h\,, \quad y > \sqrt{3}x\,, \text{ and } y > -\sqrt{3}x\}$$

with boundaries $\partial\Omega_{in} = T \times \{0\}$, $\partial\Omega_{out} = T \times \{L\}$, and $\partial\Omega_{wall} = \partial T \times (0, L)$. Similar formulas are available for channels with various geometries [4].

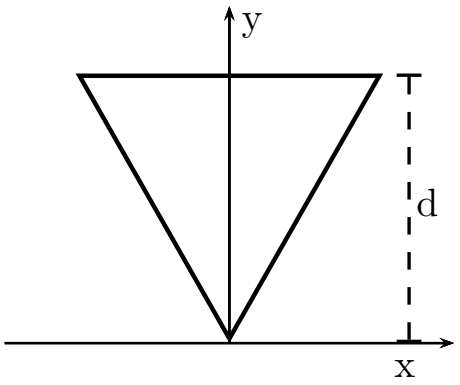

Figure 3.1 The schematic cross-section of a triangular channel.

Note that the solution $(u^\dagger, p^\dagger)$ given by (12.1)–(12.2) satisfies the system (9.6a)–(9.6e) with $f^\dagger = 0$ and functions $g^\dagger = \big(0, 0, u^\dagger(\cdot,\cdot,0)\big)$ and

$$h^\dagger = \Big(0, 0, \tfrac{1}{2}u_3^\dagger(\cdot,\cdot,L)^2 + p^\dagger(\cdot,\cdot,L)\Big).$$

For our simulations, we set $d = 1$ and $L = 1$. The model parameters are set to $\nu = 0.1$, $p_0 = 1$, and $p_L = 0$. The exact solution of (9.6a)–(9.6b) is then given by

$$\begin{aligned} p^\dagger(x,y,z) &= 1 - z \qquad \text{and} \\ u^\dagger(x,y,z) &= (0, 0, 2.5(y-1)(y-\sqrt{3}x)(y+\sqrt{3}x)). \end{aligned}$$

The corresponding right-hand side and boundary data are given by

$$\begin{aligned} f^\dagger(x,y,z) &= (0,0,0), \\ g^\dagger(x,y,0) &= \Big(0, 0, 2.5(y-1)(y-\sqrt{3}x)(y+\sqrt{3}x)\Big), \quad \text{and} \\ h^\dagger(x,y,1) &= (0, 0, -3.125(y-1)^2(y-\sqrt{3}x)^2(y+\sqrt{3}x)^2). \end{aligned}$$

These functions will serve as the reference solution and as the model data for our computational tests.

12.1 The linearization error

For the verification of the estimates for the linearization error given in Theorem 9.3, we construct perturbed data u^δ by adding random noise to $u^\dagger$ such that $\|u^\delta - u^\dagger\|_{L^3(\Omega)} = \delta$.

To observe the error induced by the data misspecification only we compute the solution (u, p) of the linearized problem (9.3a)–(9.3e) with data $f = f^\dagger$, $g = g^\dagger$, and $h = h^\dagger$ by the finite element method discussed in section 11. The resulting errors for different values of the noise level δ and various mesh sizes are displayed in Figure 3.2. Here, the first refinement level corresponds to a mesh with 192 elements and 75 vertices. All further refinement levels are obtained by a uniform refinement.

Theorem 9.3 predicts an error estimate of the form

$$\|u - u^\dagger\|_{H^1} + \|p - p^\dagger\|_{L^2} \leq C(\delta + \text{modeling errors}).$$

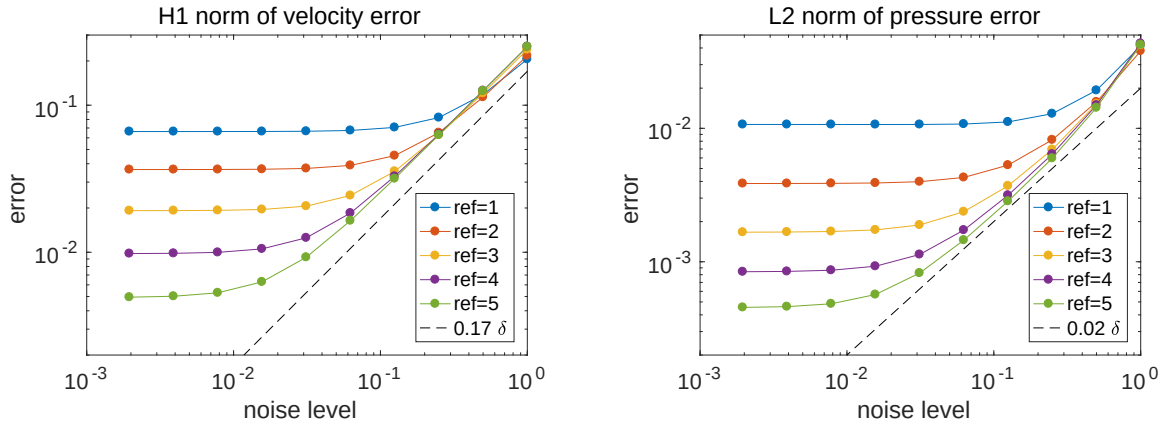

Figure 3.2 Linearization errors $\|u - u^\dagger\|_{H^1(\Omega)}$ (left) and $\|p - p^\dagger\|_{L^2(\Omega)}$ (right) for different values of the noise level δ and various refinement levels.

Note that no modeling errors are present in the example shown here and we obtain the expected $\mathcal{O}(\delta)$ convergence for both the error in the velocity and in the pressure on a refined mesh. For large mesh sizes, we observe, however, a saturation effect if δ goes to zero. This is due to the fact that the discretization error also contributes to the total error.

We observe qualitatively the same results, if we repeat the same computations for a fixed mesh size but now with randomly misspecified right-hand side f. In this case the saturation effect, also on refined meshes, is due to the misspecification of the right-hand side.

12.2 The reconstruction error

Let us discuss the estimates for the reconstruction error in Theorem 10.2. We use again the flow through the triangular channel described above and construct perturbed data u^δ by adding random noise to $u^\dagger$. We solve the discretized optimal control problem (11.2a)–(11.2b) in order to compute an approximation to the minimizer of (10.1a)–(10.1b). As a first test, we set again $f^* = f^\dagger$, $g^* = g^\dagger$, and $h^* = h^\dagger$.

From Theorem 10.2, we infer in this case that $\|u_\alpha - u^\dagger\|_{L^2(\Omega)} \leq C\delta$ and

$$\|u_\alpha - u^\dagger\|_{H^1(\Omega)} + \|p_\alpha - p^\dagger\|_{L^2(\Omega)} \leq C(\delta + \delta/\sqrt{\alpha}).$$

In the case of data misspecification this is no longer the case and the *modeling error* also contributes to the estimates. Therefore, we repeat the test, this time with perturbed model data $f^* \neq f^\dagger$ such that $\|f^\dagger - f^*\|_{L^2(\Omega)} = 2$.

For the computations, we use a refined mesh with 1377 nodes and 6144 triangles here. We show the results for different values of the noise level δ and regularization parameter α with and without modeling error in Figure 3.3.

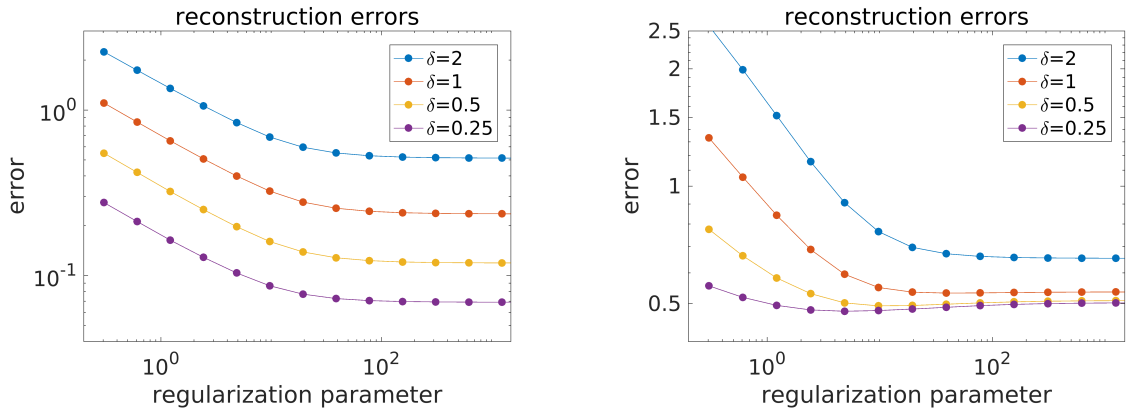

Figure 3.3 The dependence of the reconstruction errors $\|u_\alpha - u^\dagger\|_{H^1(\Omega)} + \|p_\alpha - p^\dagger\|_{L^2(\Omega)}$ on the regularization parameter α for exact model data $\|f^\dagger - f^*\|_{L^2(\Omega)} = 0$ (left) and for perturbed model data $\|f^\dagger - f^*\|_{L^2(\Omega)} = 2$ (right).

For large regularization parameters, we expect to obtain the forward solution of problem (11.2a)–(11.2b) with $f = f^*$. The results show that a constant error is reached where the constant depends on the data noise δ. For exact model data, we observe again the $\mathcal{O}(\delta)$ convergence of the forward solution.

On the other hand, for $\alpha \to 0$ the ill-posedness of the underlying approximation problem causes a blow-up as predicted by Theorem 10.2. We observe a semi-convergence behaviour for every curve depicted in Figure 3.3. For perturbed model data, we observe that an optimal value of α exists, resulting in the best approximation. Note that for correct model data this value is nearly constant, while for perturbed model data we observe an influence of the data error δ.

In all tests shown here, the residuals $\|u_\alpha - u^\delta\|_{L^2(\Omega)}$ were monotonically decreasing as predicted by Lemma 10.3. This enables us to employ an automated choice of the regularization parameter α using a *discrepancy principle*, see e.g. [27]. Following a standard procedure, we automatically select a regularization parameter for the reconstruction. For this, we define

$$\alpha_{dis}(\delta) = \max\{\alpha = \alpha_0 2^{-k} : \|u_\alpha - u^\delta\|_{L^2(\Omega)} \leq \tau\delta, \quad k \in \mathbb{N}\},$$

where $\alpha_0 > 0$ and $\tau > 1$ are given. This allows us to compute the minimizer of (11.2a)–(11.2b) for e.g. $\alpha = \alpha_0 2^{-k}$ and then automatically select α_{dis} as the value where the minimizer satisfies the inequality $\|u_\alpha - u^\delta\|_{L^2(\Omega)} \leq \tau\delta$ for the first time.

12.3 Comparison with other filters

For further evaluation of the performance of the proposed fluid-dynamically consistent filter (10.1a)–(10.1b), we also show a comparison to the smoothing filter (10.5) and solenoidal filtering approaches (10.6a)–(10.6b) with and without smoothing. Since all methods were implemented in a similar fashion, a fair comparison is possible. Additionally, we show here results for the iterated filtering approach (10.4a) introduced in section 10.3. For the choice of the regularization parameter, we employed a discrepancy principle with $\tau = 1.2$ for all methods if necessary.

We list the results for those different methods in Table 3.1. We compare the error of the velocity reconstruction in the L^2- and H^1-norm respectively, and the error for the pressure in the L^2-norm, if available. For all reconstructions we also show the discrete divergence $\nabla_h \cdot u$, which corresponds to the projection of $\nabla \cdot u$ onto the discrete pressure space.

filtering method	$\|u - u^\dagger\|_{L^2}$	$\|u - u^\dagger\|_{H^1}$	$\|p - p^\dagger\|_{L^2}$	$\|\nabla_h \cdot u\|_{L^2}$
smoothing	0.083147	0.866226	*.******	0.00105
solenoidal ($\alpha = 0$)	0.080510	5.850591	0.548718	0.00000
solenoidal w. smoothing	0.083147	0.866224	0.548396	0.00000
fluid-dyn. consistent	0.011437	0.195073	0.056044	0.00000
iterated filter	0.007484	0.103961	0.015309	0.00000

Table 3.1 Reconstruction errors for velocity and pressure and discrete divergence of the reconstructed velocity field for different filter strategies at noise level $\delta = 0.1875$ on a mesh with 1377 vertices and 6144 tetrahedral elements.

For all presented filters, the norm $\|u - u^\dagger\|_{L^2}$ is penalized. As a direct consequence, the performance of all methods is comparable with respect to this error measure. Note that for the iterated filter the data error can be even further reduced in this example.

Further, we observe a sufficient reconstruction in terms of the H^1-norm for all methods where some sort of smoothing is applied. For the solenoidal filter without smoothing, the H^1-norm increases for a smaller mesh size which we expected due to the underlying ill-posed approximation problem.

The pure smoothing filter does not enforce the discrete divergence to be zero. Therefore, in contrary to all other methods, also no reconstruction of the pressure is obtained. For both solenoidal filters, the error in the pressure reconstruction is, however, about an order of magnitude higher than for the fluid-dynamically consistent methods. This implies, that for those methods no approximation on the physical pressure is obtained. Also with respect to this measure, the iterated filtering approach brings a noticeable improvement. This can be explained by the fact, that the background velocity in the used fluid model strongly influences the reconstruction. The usage of a pre-filtered velocity field can reduce this error drastically.

In summary, the fluid-dynamically consistent filters show the best performance with respect to the error measures presented here. We observe here also, that the iterated filtering approach brings an additional improvement of the error.

IV Application to experimental data

In order to verify the applicability of our approach in a more realistic setting, we apply the proposed domain identification and velocity filtering techniques to experimental data. We use measurements obtained by magnetic resonance velocimetry at the University Medical Center in Freiburg and the support of the Medical Physics group is gratefully acknowledged.

The object under investigation in this study was a blood vessel inside the human head, or more precisely the *common carotid artery* which plays an important role in the supply of the brain with oxygenated blood. The available data provide a three-dimensional picture of a human head roughly between chin and mouth. We show the magnitude of the available data in the axial plane at different heights in Figure 4.1.

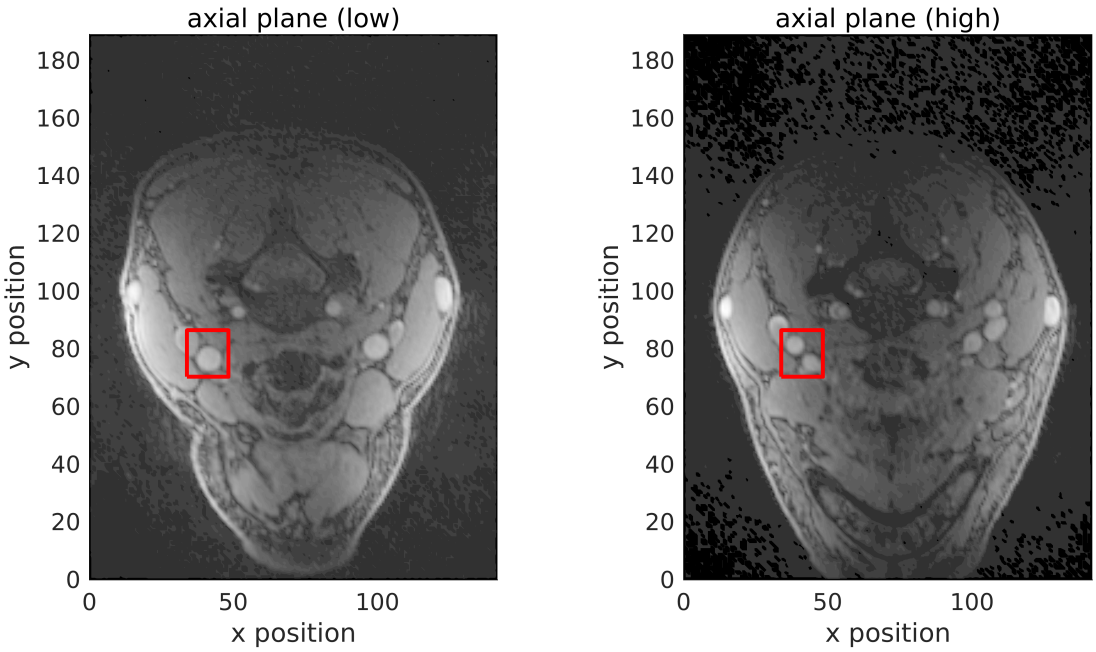

Figure 4.1 The axial plane taken from the available MRT signal at different heights; approximately at the chin (left) and the mouth (right). The region containing one of carotid arteries is marked with a red rectangle.

The shape of the head is clearly visible in the data and typical features are present, like for instance the cervical spine on both pictures, or the teeth in the lower part of the right picture. The domain of interest, i.e. one of the carotid

arteries, is marked with a red rectangle in both pictures in Figure 4.1. We show a cross-section before (left) and after (right) the so-called *bifurcation*. At this bifurcation, the blood vessel splits into two distinct arcs.

The available data consist of $224 \times 168 \times 48$ voxels of size $0.8482 \times 0.8482 \times 0.85\text{mm}^3$ for the magnitude of the MRT signal and the three velocity components. Additionally, the measurements are time-dependent and data are available at 12 different time steps equally distributed over the time of one heart beat. Note that even though the measurements are resolved in time, the data for each single time step are nevertheless time-averaged over several heart beats. For our purpose, we select a single time-point for each example presented here.

While the possible change of the geometry during the Systole and Diastole is not resolved in the measurements, the difference in the blood velocity is clearly visible in the data. For comparison, we show the reconstruction of the velocity and pressure at two different time points in section 14.

The area of interest, i.e. the bifurcation of the *common carotid artery*, is considerably smaller than the available domain. As a first step, we select a suitable volume containing one of the arteries, marked as red rectangle in Figure 4.1. For all further computations, we use this smaller data set containing $20 \times 18 \times 28$ voxels.

13 Geometry identification

Let us discuss the geometry identification for the blood vessel. We compute an approximate indicator function of the domain of interest as a pre-processing step, where we use the available MRT signal depicted in Figure 4.1. Let us note that in this section we use the data from a fixed time point only. As mentioned above, the change of geometry over the available time slot is negligible here and the results show no significant differences.

In a second step, we apply the domain identification method discussed in part II to compute a mesh representing the three-dimensional geometry. Due to the complex structure of the blood vessel, we divide the problem into several two-dimensional sub-problems which makes an efficient computation possible.

13.1 Data pre-processing

The basis for the geometry identification will be an indicator function of the vessel geometry computed from the magnitude of the MRT signal. We depict again the cross-sections shown in Figure 4.1 for the smaller data set which was marked as red rectangle.

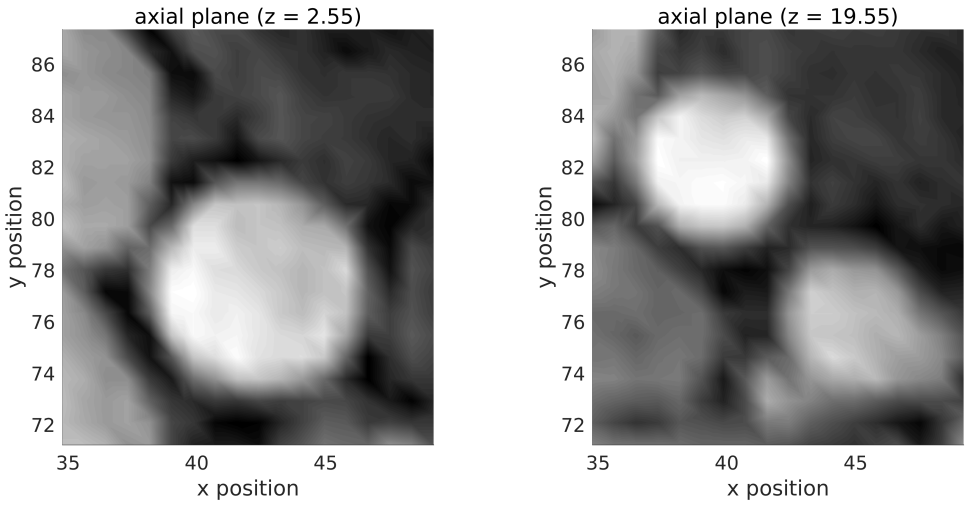

Figure 4.2 The MRT signal in vicinity of a common carotid artery. The pictures correspond to the area marked in Figure 4.1 and show a cross-section of the the carotid artery before and after the bifurcation.

A closer inspection reveals that the data are not homogeneous across the blood vessel due to measurement errors. Additional, further tissue surrounding the vessel is also present which has to be removed to some extent. Let us note that due to the small size of the domain of interest the data have a rather low resolution.

For the available cross-sections, we roughly select the area containing the carotid artery and apply a suitable cut-off function in order to derive an approximate indicator function of the blood vessel. The result for four exemplaric cross-sections is depicted in Figure 4.3.

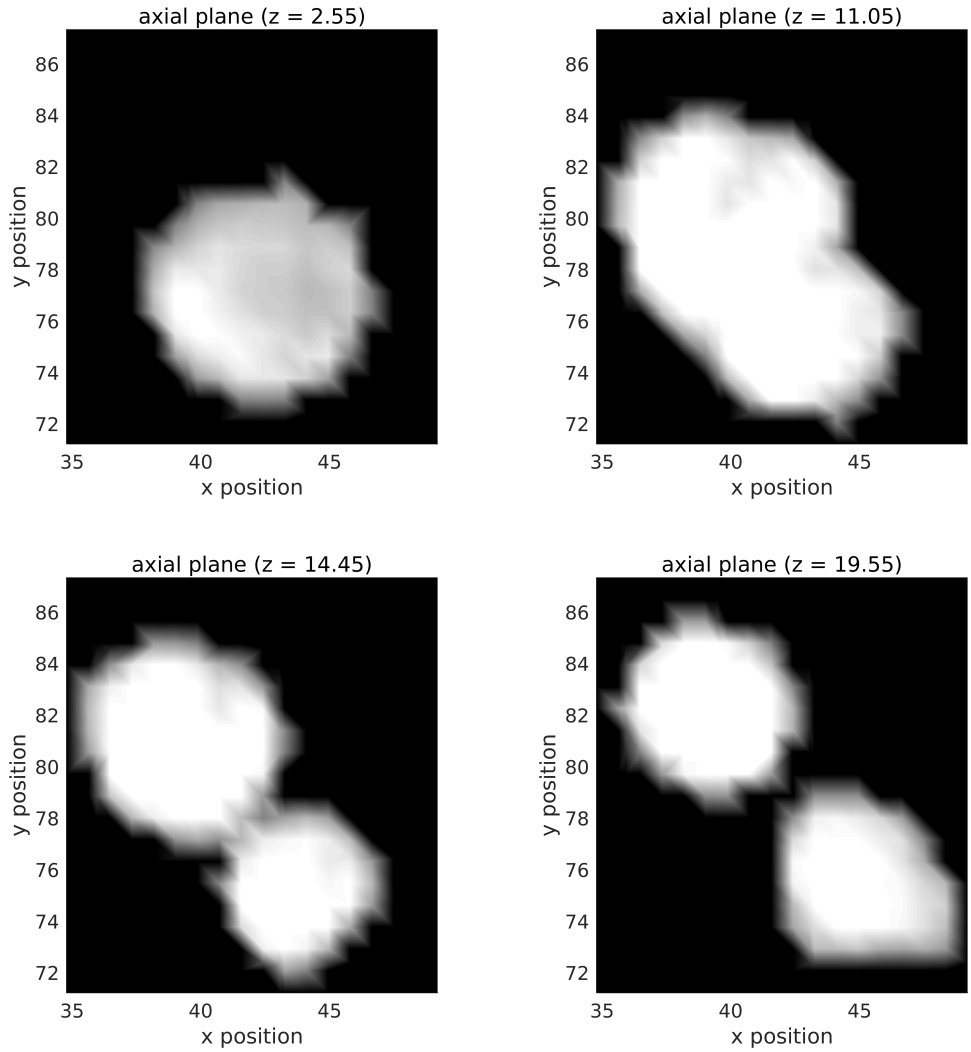

Figure 4.3 The approximate indicator function for the blood vessel. We show several cross-sections at different heights to illustrate the bifurcation into two distinct arcs.

After this pre-processing step, we obtain an approximate indicator function of the three-dimensional vessel geometry given on the same voxel grid as the original data. From the cross-sections depicted in Figure 4.3, we can see the rather sharp transition from a single arc to two distinct blood vessels. Those data will be the basis for the application of the proposed domain identification method in the next step.

13.2 Identification of the vessel geometry

Let us discuss the identification of the vessel geometry. We recall from section 6 that for the identification, we solve an optimization problem of the form

$$\min_{\mathrm{h}\in\mathcal{H}_{\mathrm{ad}}} \tfrac{1}{2}\|\mathrm{F}(\mathrm{h}) - \mathrm{p}^{\mathrm{ref}}\|^2_{H^1(\mathrm{R})} + \tfrac{\alpha}{2}\mathcal{R}(\mathrm{h}).$$

The forward operator F is defined via the solution of an elliptic partial differential equation and is well-defined for any deformation h stemming from the admissible set $\mathcal{H}_{\mathrm{ad}} \subset H^1(\mathrm{R})^d$. The reference potential $\mathrm{p}^{\mathrm{ref}}$ is computed from a given reference domain $\Omega^{\mathrm{ref}} \subset \mathrm{R}$, and the regularization term $\mathcal{R}(\mathrm{h})$ can be adapted to promote certain properties of the identified domain $(\mathrm{id} + \mathrm{h})(\Omega^{\mathrm{ref}})$, see section 7.3 for more details.

As mentioned before, the domain of interest is a complex three-dimensional geometry and from the discussion in section 7.3 we infer that the reference domain Ω^{ref} should in some sense be close to the desired shape. Further, we need to provide a regular mesh representing such a geometry.

For convenience, we present a different strategy here. First of all, we restrict ourselves to the lower part of the blood vessel, i.e. the region before the bifurcation bounded by the cross-sections shown in the upper half of Figure 4.3. For such a shape, we can divide the three-dimensional problem into a series of two-dimensional sub-problems.

Identification of cross-sections. In order to reconstruct a volumetric representation of the blood vessel, we apply the domain identification method described in part II to a series of cross-sections. The advantage of such an approach is twofold. Clearly, the two-dimensional sub-problems are much smaller and therefore less computational intensive. Further, this enables us to use the same two-dimensional reference mesh for the identification of the single cross-

sections. In order to obtain a three-dimensional representation, we can directly generate a prism mesh from the resulting two-dimensional triangular meshes.

From Figure 4.3, we see that the the cross-section in the lower part of the blood vessel is approximately circular. Therefore, we use a circular reference domain Ω^{ref} with radius 3.5 mm and a surrounding box R of size 25 mm. We use a triangular mesh with 3458 vertices and 6738 triangles on R. The embedded mesh representing the reference domain has 531 vertices and 932 elements. For the identification, we use a mesh which is refined around the boundary $\partial\Omega^{\text{ref}}$.

Let us start with the identification of the lowest available cross-section. As regularization term, we use here $\mathcal{R}(h) = \|\nabla h\|^2_{L^2(R)}$ and regularization parameters $\alpha = 0.005$ and $\tilde{\alpha} = 0.05$, see section 8 for more details on the choice of the parameters. We show the result in Figure 4.4 together with the corresponding velocity in z-direction along the artery interpolated from the measurements.

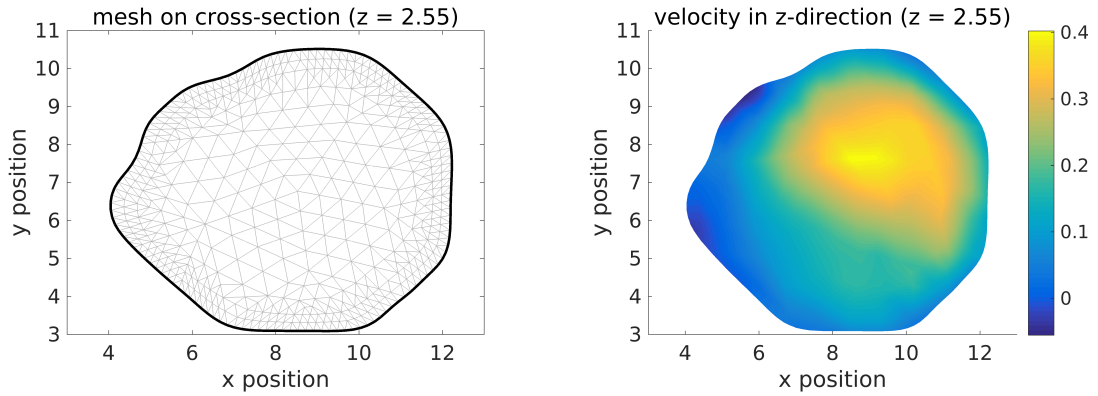

Figure 4.4 The identified mesh for the lowest available cross-section of the carotid artery. On the right, we depict the interpolated velocity in z-direction perpendicular to the image plane.

The deformed reference mesh results in an approximately circular representation of the vessel cross-section. Further, we obtain a mesh with regular triangles, since only small deformations of the reference domain were necessary.

For further evidence of the successful identification of the cross-section, we depict a component of the interpolated velocity data on the right side of Figure 4.4. The flow velocity is directed in z-direction here, i.e. perpendicular to the shown image plane. We observe that the velocity is close to zero at the identified boundaries. This additionally indicates that the identified geometry is a good approximation of the vessel cross-section.

Iterated application. We apply a similar procedure for the identification of the subsequent cross-sections. Recall that we use the same reference mesh in order to obtain a three-dimensional prismatic mesh from the combination of the different slices.

From section 7.3, we have that the penalization of the gradient of h ensures the mesh quality for the two-dimensional reconstruction in this case. In order to obtain a regular prism mesh, we further require the node positions of neighboring cross-sections to be close to each other regarding the distance in the $x-y$-plane. Therefore, we use an adapted regularization term of the form

$$\mathcal{R}(\mathrm{h}) = \|\nabla \mathrm{h}\|^2_{L^2(\mathrm{R})} + \|\mathrm{h} - \mathrm{h}_{old}\|^2_{L^2(\mathrm{R})},$$

where h_{old} denotes the deformation computed for the previous cross-section. Such a term additionally ensures that the deviation of the node positions compared to the previous mesh is controlled. We also utilize h_{old} as initial value for the iterative approximation of a minimizer.

For the subsequent cross-sections, we proceed as above, using the same reference mesh. We show a cross-section directly before the bifurcation in Figure 4.5.

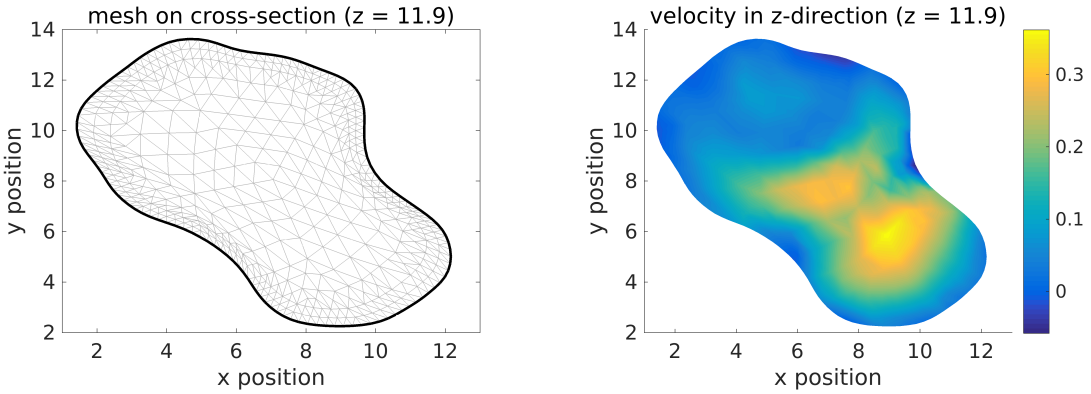

Figure 4.5 The identified mesh for a cross-section close to the bifurcation of the carotid artery. On the right, we depict the interpolated velocity in z-direction.

From the velocity profile on the right side of Figure 4.5, we observe that the flow profile already is separated in this region to enter the two distinct arcs. The splitting of the geometry is also indicated by the shape of the cross-section. Also for this strongly deformed shape we have a good mesh quality of the two-dimensional mesh.

In order to obtain a representation of the blood vessel, the identified cross-sections are combined to a prismatic mesh. We show a visualization of the complete three-dimensional mesh from two different perspectives in Figure 4.6.

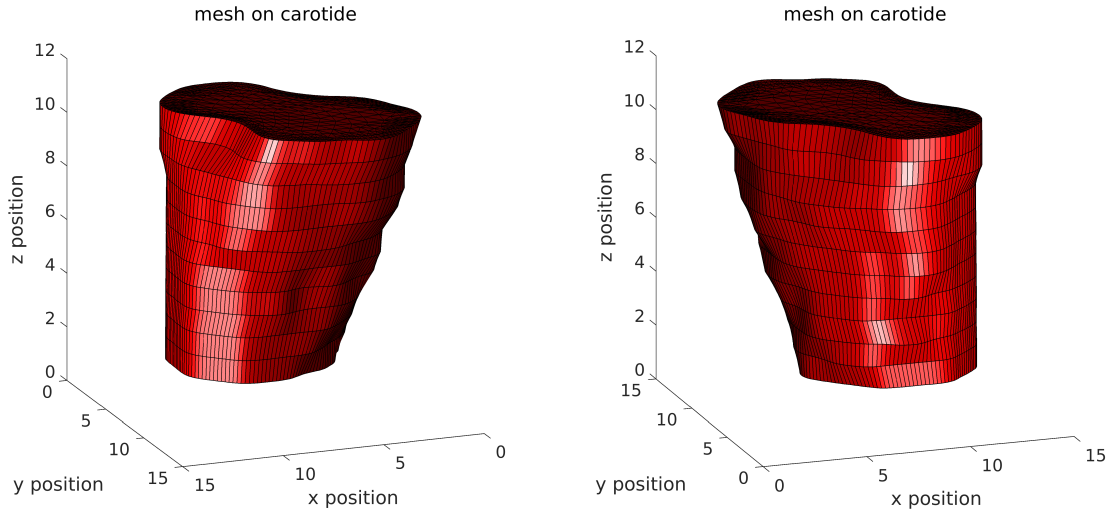

Figure 4.6 The lower part of the blood vessel identified from the MRT magnitude.

From the reconstruction, we see that the approximately circular blood vessel deforms along the z-direction. In the upper part, we can already see the beginning of the separation into two distinct arcs.

The bifurcation. Let us finally comment on the treatment of the bifurcation of the blood vessel which is not shown here. Above, we extensively made use of the fact that a distinguished direction exists along which the geometry does change only slightly. However, from the pictures in Figure 4.3, we see that this is no longer the case at the bifurcation. Therefore, treating single cross-sections is not directly transferable to this case. Further, note that the domain representing the cross-section changes its topology here.

This makes the treatment using a three-dimensional reference domain the better choice in this case. While the domain identification method discussed in part II is independent of the dimension, the difficulty in this case is to provide a suitable reference mesh. However, if such a construction is available, we may proceed in the same fashion as for the two-dimensional problems above.

14 Reconstruction of the flow velocities

As a final step of the proposed data enhancement procedure, let us discuss the reconstruction of the flow velocities and the pressure field in the blood vessel. For that purpose, we apply the fluid-dynamically consistent filter discussed in part III to the available velocity measurements. We denote by Ω the identified domain computed in section 13 and by u^δ the interpolated velocity data available from the measurements. For convenience, we compute a reconstruction on a subsection of the identified blood vessel only. Therefore, we select a part of the obtained prism mesh of length 3.4 mm. In order to apply the finite element method discussed in section 11, we use a tetrahedral mesh obtained from the prism mesh constructed in section 13. Since time-dependent measurements are available, we show examples for the reconstruction at two different time-points.

Recall that the fluid-dynamically consistent filter was formulated in section 10 as the optimal control problem

$$\min_{f,g,h} \|u(f,g,h) - u^\delta\|^2_{L^2(\Omega)} + \alpha \mathcal{R}(f,g,h),$$

where

$$\mathcal{R}(f,g,h) = \|f - f^*\|^2_{L^2(\Omega)} + \|g - g^*\|^2_{H^1(\partial\Omega_{in})} + \|h - h^*\|^2_{L^2(\partial\Omega_{out})}$$

and the flow velocities $u(f,g,h)$ and the corresponding pressure field $p(f,g,h)$ denote the unique weak solution of a linearized flow model of the form

$$\begin{aligned} -\nu\Delta u + \tfrac{1}{2}u^\delta \cdot \nabla u + \tfrac{1}{2}\mathrm{div}(u \otimes u^\delta) + \nabla p &= f \quad \text{in } \Omega, \\ \nabla \cdot u &= 0 \quad \text{in } \Omega, \end{aligned}$$

with boundary conditions

$$\begin{aligned} u &= g \quad \text{on } \partial\Omega_{in}, \\ u &= 0 \quad \text{on } \partial\Omega_{wall}, \\ (-\nu\nabla u + \tfrac{1}{2}u \otimes u^\delta + pI) \cdot n &= h \quad \text{on } \partial\Omega_{out}. \end{aligned}$$

A first necessary step will be to determine suitable boundary conditions and model data which are necessary for the formulation of the filter. Afterwards, we apply the proposed filtering technique to the available data.

14.1 Choice of boundary conditions and model data

The choice of boundary and model data is a crucial ingredient for the successful identification of flow velocities and the pressure field. Recall that the reference functions f^*, g^* and h^* are present in the error estimates for the reconstruction error, see section 10.2.

The background velocity. As discussed in section 10.3 and demonstrated by the numerical results in section 12, an iterated filtering can drastically reduce the resulting error. Further, we expect a high data error for the available velocity data due to the low resolution.

In order to obtain a reasonable reconstruction from the fluid-dynamically consistent filter, we do not directly use the measurements u^δ a background velocity here. Instead, we apply a pre-filtering strategy in order to obtain a smoothed and divergence-free velocity field which we use for that purpose. More precisely, we apply a smoothing solenoidal filter as described in section 10.4 with $\alpha = 0.01$, where we additionally employ a no-slip condition for the velocity on the wall of the blood vessel. We denote the pre-filtered velocity field by $\tilde{u}^\delta$.

Boundary conditions. Let us define the boundaries $\partial\Omega_{in}$, $\partial\Omega_{wall}$ and $\partial\Omega_{out}$ first. We denote by $\partial\Omega_{wall}$ the wall of the blood vessel. We set $\partial\Omega_{in}$ in this case to be the lowest cross-section of the reduced vessel geometry, where the blood is usually pumped in by the heart. Similar the topmost cross-section where the blood flows out will be denoted by $\partial\Omega_{out}$, see also Figure 4.6.

For the reference function f^*, we set, for lack of better knowledge, $f^* = 0$. The choice of the inflow and outflow boundary conditions is a little bit more delicate. Clearly, the choice $g^* = 0$ is not a good approximation of the actual flow conditions.

Therefore, we utilize again the smooth pre-filtered velocity field $\tilde{u}^\delta$ and compute an approximation of the boundary conditions g^* and h^*. More precisely, we set

$$\begin{aligned} g^* &= \tilde{u}^\delta_{|\partial\Omega_{in}}, \quad \text{and} \\ h^* &= \big(-\nu\nabla\tilde{u}^\delta + \tfrac{1}{2}\tilde{u}^\delta \otimes \tilde{u}^\delta \big)_{|\partial\Omega_{out}}. \end{aligned}$$

For illustration, we show the approximated inflow velocity profile in z-direction on $\partial\Omega_{in}$ for two different time-points in Figure 4.7.

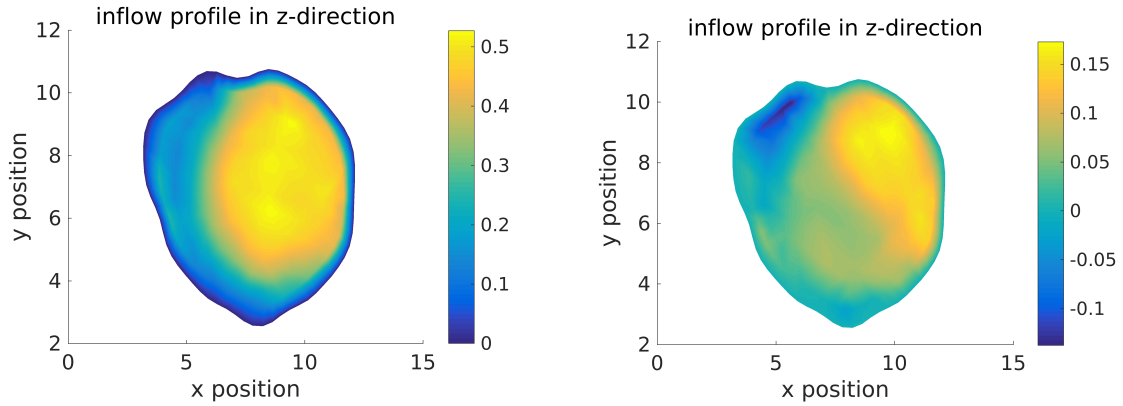

Figure 4.7 The inflow profile on $\partial\Omega_{in}$ computed from a smoothing solenoidal filtering approach for two different time points. We have a much faster inflow for the Systole (left) than for the Diastole (right) where a more disturbed velocity profile evolves.

The viscosity parameter. As a last step, we need to fix the viscosity parameter ν. Since blood is a non-Newtonian fluid, we expect a certain modeling error due to the fact that we use a Newtonian flow model. As discussed in part III, such unmodeled effects are in principle taken care for by the identified residual f in the fluid filter. Since for non-Newtonian fluids the viscosity can depend on the flow velocity, such an effect contributes to the modeling error.

In order to determine a constant viscosity parameter which delivers the "best" approximation of the present flow conditions, we proceed in a similar fashion as in [24]. We compute a solution of the forward problem when using the reference functions f^*, g^* and h^* and compare the residuals $\|u - u^\delta\|$ for different values of ν in Table 4.1. For comparison, we use again the data stemming from two different time-points which represent the Systole and Diastole.

	ν	1	0.05	0.008	0.005	0.001	0.00001
Diastole	$\|u_\alpha - u^\delta\|_{L^2}$	1.2079	0.9446	0.8724	0.8730	0.9221	1.9136
Systole		0.6242	0.5841	0.4810	0.4811	0.5173	0.6164

Table 4.1 Data residuals $\|u_\alpha - u^\delta\|_{L^2(\Omega)}$ for different forward solves with viscosity ν.

The results in Table 4.1 indicate that a value of approximately $\nu \approx 0.008$ is the most reasonable choice here. This also indicates that the change in the viscosity due to different flow conditions is not very strong here.

14.2 Results for the fluid-dynamically consistent filter

We are now ready to apply the fluid-dynamically consistent filter to the available measurements. We compute the three-dimensional reconstruction on the domain identified in section 13. As motivated above, we use the viscosity parameter $\nu = 0.008$ in both cases and the background velocity and boundary data computed from the solenoidal reconstruction.

From Lemma 10.3 in section 10.2, we have that the residual decreases for $\alpha \to 0$. From this fact and from the numerical results in section 12, we expect to recover the measurements in some sense for small α. We show an exemplaric reconstruction with $\alpha = 0.001$ in Figure 4.8. We obtain a noisy reconstruction which

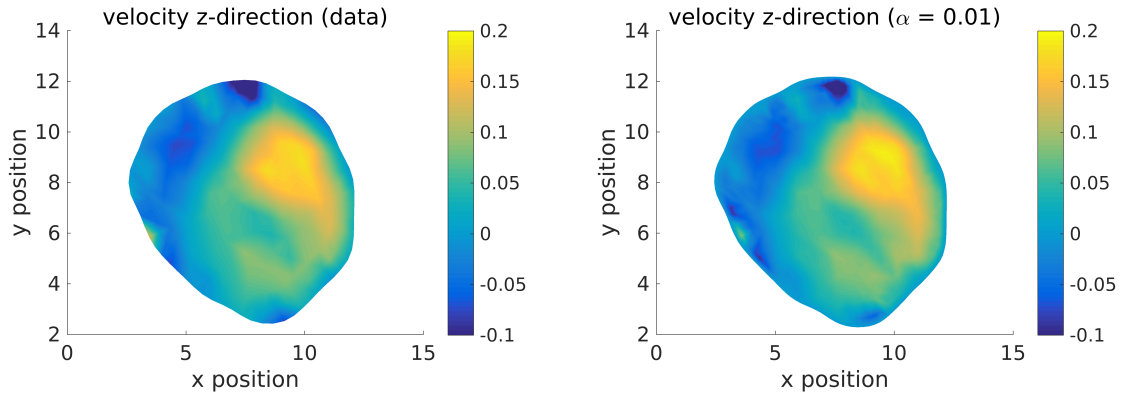

Figure 4.8 The velocity profile in z-direction interpolated from the measurements at a cross-section at height $z = 7.65$ mm (left). On the right, we show the reconstructed velocity for $\alpha = 0.01$.

is comparable to the data except for the boundary condition. Note, however, that the discrete divergence of the reconstruction is zero here.

As demonstrated in section 12, we expect to obtain the forward solution with data f^*, g^* and h^* if the regularization parameter is chosen large enough, which is not shown here. Instead, we show the reconstruction using the fluid-dynamically consistent filter with regularization parameter $\alpha = 100$ here. For illustration, we show the resulting velocity profile and pressure distribution on a cross-

section at height $z = 7.65$ mm for two different time points. The time points chosen correspond to the velocity profiles shown in Figure 4.7. We differentiate between the *Systole*, where the heart is actively pumping blood through the vessel resulting in a comparably fast flow, and the *Diastole*, where the heart is relaxing again and the flow is dominated by inertial effects.

Systole. We show results of the fluid-dynamically consistent filter for a time-point stemming from the Systole first. We depict the reconstructed velocity components and the pressure field of a cross-section in Figure 4.9.

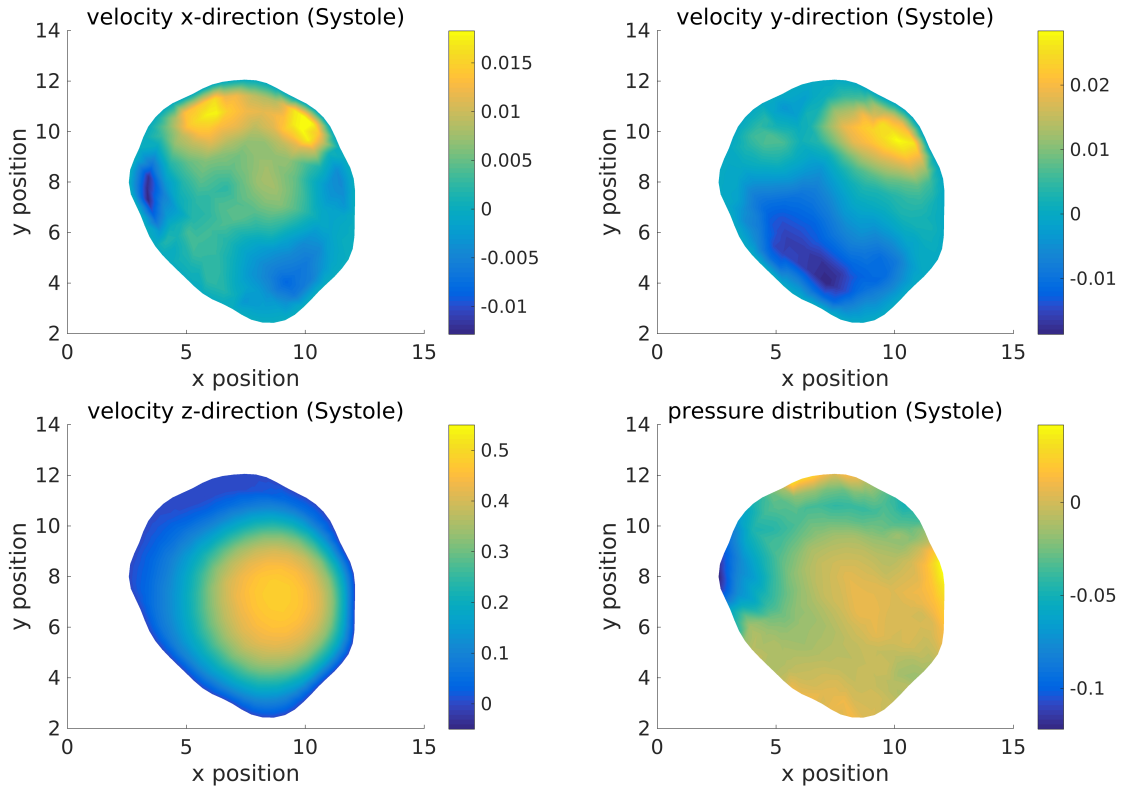

Figure 4.9 The reconstructed velocity profile at the Systole at a cross-section at height $z = 7.65$ mm and the corresponding pressure distribution.

In the Systole, the heart is actively pumping blood through the blood vessel and therefore, we observe an approximately parabolic velocity profile in z-direction. The transversal velocity components indicate some sort of rotational flow. The pressure distribution in the cross-section shows some variations with pressure peaks in some corners of the blood vessel.

Diastole. For comparison, we show the results for the reconstruction at a time point in the Diastole. We depict again the reconstructed velocity components and the pressure field of the same cross-section as before in Figure 4.10.

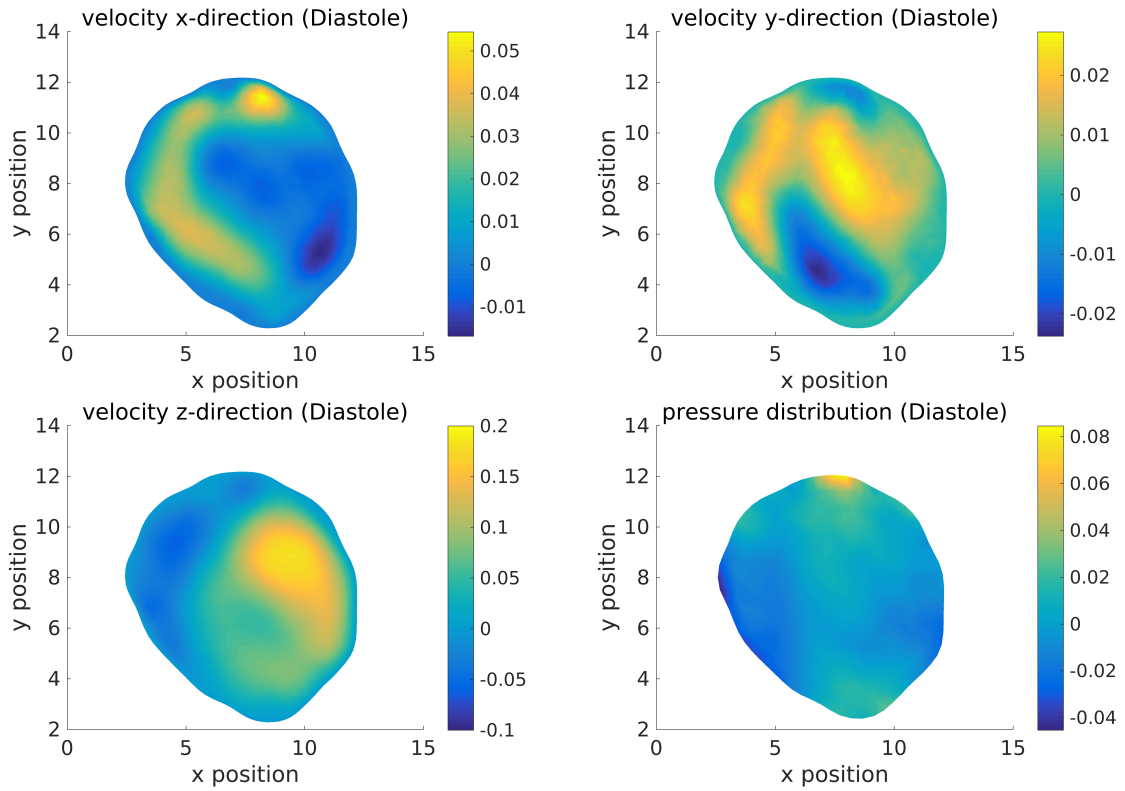

Figure 4.10 The reconstructed velocity profile at the Diastole at a cross-section at height $z = 7.65$ and the corresponding pressure distribution.

In this phase, the blood is not pumped actively by the heart, but the flow rather evolves from inertial effects. This results in much smaller velocities in z-direction here. Further, due to the missing pushing force the flow seems much more turbulent here. The rotational flow already observed during the Systole is still present, but much more vivid in some sense. The pressure distribution is approximately constant here, but some pressure peaks can still be observed, however in different corners of the cross-section.

Summary. Our results demonstrate that the domain identification and flow reconstruction procedures introduced in this thesis can be used for applications with in-vivo data. Even though some pre-processing is necessary, we were able to reconstruct the velocity and pressure distribution in a blood vessel from measurements obtained by magnetic resonance velocimetry.

Conclusion and outlook

In this thesis we proposed and analyzed problem adapted methods for the geometry identification and data enhancement of distributed flow measurements. As an application we used here measurements given from magnetic resonance velocimetry, however, the procedures are in principle also applicable for other non-invasive distributed measurement techniques.

The problem formulations as optimal control problems with partial differential equations, or the Tikhonov regularization for suitable inverse problems respectively, have a more or less generic character. However, the actual methods are clearly problem adapted, since we extensively used the available data as part of the problem formulations.

Our results show that such specialized formulations do indeed pay off in form of e.g. additional information which would not be available with a more general approach. In this sense the additional work which has to be done for the modelling and also the analysis of the resulting problems can be considered reasonable.

Further directions. The ideas discussed here are clearly only a first step in the direction of a fully automatic evaluation of complex measurements. Compromises were made especially for the choice of the model equations in order to develop fully analyzable methods. On the other hand, the general methodology may be feasible for a large class of problems involving distributed measurements. However, the availability of a comparable analysis to the one presented here will clearly depend on the desired models for the underlying physics.

In the context of data enhancement the approach to use the available distributed measurement data for a suitable linearization of the model equations is clearly applicable to a wider class of problems. In some sense such a procedure may be generalized is various ways, however, an estimate for the linearization error has to be available.

A further step, which was not discussed here, is the rigorous experimental validation and verification of the results. For that, experimental setups will have to be constructed, where a “ground truth” is available in form of highly resolved reference measurements or computations.

List of Figures

List of Tables

BIBLIOGRAPHY

[1] F. Abergel and R. Temam. On some control problems in fluid mechanics. *Theoret. Comput. Fluid Dynamics*, 1:303–325, 1990.

[2] Robert A. Adams. *Sobolev spaces*. Academic Press, New York, 1975.

[3] H. T. Banks and K. Kunisch. *Estimation techniques for distributed parameter systems*, volume 1 of *Systems & Control: Foundations & Applications*. Birkhäuser, 1989.

[4] G. K. Batchelor. *An Introduction to Fluid Dynamics*. Cambridge University Press, Cambridge, 1967.

[5] D. P. Bertsekas. On the goldstein-levitin-polyak gradient projection method. *IEEE Trans. Automat. Control*, AC-21:174–184, 1976.

[6] B. Blaschke, A. Neubauer, and O. Scherzer. On convergence rates for the iteratively regularized gauss-newton method. *IMA Journal of Numerical Analysis*, 17:421—436, 1997.

[7] D. Boffi, F. Brezzi, L. F. Demkowicz, R. G. Durán, R. S. Falk, and M. Fortin. *Mixed finite elements, compatibility conditions, and applications*, volume 1939 of *Lecture Notes in Mathematics*. Springer-Verlag, Berlin, 2008.

[8] D. Boffi, F. Brezzi, and M. Fortin. *Mixed Finite Element Methods and Applications*, volume 44 of *Springer Series in Computational Mathematics*. Springer Berlin Heidelberg, 2013.

[9] J. U. Brackbill. An adaptive grid with directional control. *J. Comput. Phys.*, 108:38–50, 1993.

[10] D. Braess. *Finite Elemente: Theorie, schnelle Löser und Anwendungen in der Elastizitätstheorie*. Springer Spektrum, 1992.

[11] F. Brezzi. On the existence, uniqueness and approximation of saddle-point problems arising from lagrangian multipliers. *R.A.I.R.O.*, 1974.

[12] R.W. Brown, Y. C. N. Cheng, E. M. Haacke, M. R. Thompson, and R. Venkatesan. *Magnetic Resonance Imaging: Physical Principles and Sequence Design*. Wiley, 2014.

[13] J. Busch, D. Giese, L. Wissmann, and S. Kozerke. Reconstruction of divergence-free velocity fields from cine 3D phase-contrast flow measure-

ments. *Magnetic Resonance in Medicine*, 69:200–210, 2013.

[14] F. Cao, J.-L. Lisani, J.-M. Morel, P. Muse, and F. Sur. *A Theory of Shape Identification*, volume 1948 of *Lecture Notes in Mathematics*. Springer-Verlag, 2008.

[15] J.A. Carlson, A. Jaffe, A. Wiles, Clay Mathematics Institute, and American Mathematical Society. *The Millennium Prize Problems*. American Mathematical Society, 2006.

[16] J. E. Castillo, S. Steinberg, and P. J. Roache. On the folding of numerically generated grids: Use of a reference grid. *Communications in Applied numerical methods*, 4:471–481, 1988.

[17] M. Choulli, O. Y. Imanuvilov, and M. Yamamoto. Inverse source problem for the navier-stokes equations. 2006.

[18] P.G. Ciarlet. *The Finite Element Method for Elliptic Problems*. North Holland, 1978.

[19] B. Dacorogna. *Direct Methods in the Calculus of Variations*, volume 78 of *Applied Mathematical Sciences*. Springer-Verlag, 1989.

[20] C. M. de Silva, J. Philip, and I. Marusic. Minimization of divergence error in volumetric velocity measurements and implications for turbulence statistics. *Exp. Fluids*, 54:1557, 2013.

[21] M. Desai and K. Ito. Optimal controls of Navier-Stokes equations. *SIAM J. Control and Optimization*, 32:1428–1446, 1994.

[22] F. Durst, H. Kikura, I. Lekakis, J. Jovanovic, and Q. Ye. Wall shear stress determination from near-wall mean velocity data in turbulent pipe and channel flows. *Exp. Fluids*, 20:417–428, 1996.

[23] H. Egger and M. Schlottbom. Analysis and regularization of problems in diffuse optical tomography. *SIAM J. Math. Anal.*, 42:1934–1948, 2010.

[24] H. Egger, T. Seitz, and C. Tropea. Enhancement of flow measurements using fluid-dynamic constraints. *J. Comput. Phys.*, 344:558 – 574, 2017.

[25] C. J. Elkins and M. T. Alley. Magnetic resonance velocimetry: applications for magnetic resonance imaging in the measurement of fluid motion. *Exp. Fluids*, 43:823–858, 2007.

[26] C. J. Elkins, M. Markl, N. Pelc, and J. K. Eaton. 4D Magnetic resonance velocimetry for mean velocity measurements in complex turbulent flows. *Exp. Fluids*, 34:494–503, 2003.

[27] H. W. Engl, M. Hanke, and A. Neubauer. *Regularization of Inverse Problems*. Kluwer Academic Publishers, Dordrecht, 1996.

[28] Dubsky et al. Computed tomographic x-ray velocimetry for simultaneous 3d measurement of velocity and geometry in opaque vessels. *Exp. Fluids*, 52:543–554, 2012.

[29] Matsumoto et al. Dynamic 3D-CT angiography. *AJNR Am. J. Neuroradiol*, 28:299–304, 2007.

[30] Lawrence C. Evans. *Partial differential equations*. American Mathematical Society, Providence, R.I., 2010.

[31] H. Fattorini and S. Sritharan. Existence of optimal controls for viscous flow problems. *Proc. Roy. Soc. London Ser. A*, 439:81–102, 1992.

[32] J.H. Ferziger and M. Peric. *Computational Methods for Fluid Dynamics*. Springer, 2002.

[33] R. Fletcher. *Practical methods of optimization*. A Wiley-Interscience Publication. Wiley, 2003.

[34] C. Foias and R. Temam. Structure of the set of stationary solutions of the Navier-Stokes equations. *Comm. Pure Appl. Math.*, 30:149–164, 1977.

[35] P. J. Frey and P.-L. George. *Mesh Generation: Application to Finite Elements*. Wiley, 2008.

[36] A. Fursikov. Control problems and theorems concerning the unique solvability of a mixed boundary value problem for the three-dimensional Navier-Stokes and Euler equations. *Math USSR Sb.*, 43:281–307, 1982.

[37] V. Girault and R.-A. Raviart. *Finite element approximation of the Navier-Stokes equations*, volume 749 of *Lecture Notes in Mathematics*. Springer-Verlag, Berlin, 1979.

[38] R. C. Gonzalez and R. E. Woods. *Digital Image Processing*. Prentice Hall, 2007.

[39] M. Gunzburger, L. Hou, and T. Svobodny. Analysis and finite element approximation of optimal control problems for the stationary Navier-Stokes

equations with Dirichlet controls. *Model. Math. Anal. Numer.*, 25:711–748, 1991.

[40] M. Gunzburger, L. Hou, and T. Svobodny. Boundary velocity control of incompressible flow with an application to viscous drag reduction. *SIAM J. Control Optim.*, 30:167–181, 1992.

[41] J. Hadamard. Sur les problèmes aux dérivées partielles et leur signification physique. *Princeton University Bulletin*, pages 49–52, 1902.

[42] J.V. Hajnal, D.L.G. Hill, and D.J. Hawkes. *Medical Image Registration*. CRC Press, 2001.

[43] M. Hanke and O. Scherzer. Error analysis of an equation error method for the identification of the diffusion coefficient in a quasi-linear parabolic differential equation. *SIAM J. Appl. Math.*, 59:1012–1027, 1999.

[44] G. A. Hansen, R. W. Douglass, and A. Zardecki. *Mesh Enhancement: Selected Elliptic Methods, Foundations and Applications*. Imperial College Press, 2005.

[45] Toshiyuki Hayase. Numerical simulation of real-world flows. *Fluid Dynamics Research*, 47(5), 2015.

[46] S. F. Herrmann and K. Hinsch. Holographic particle image velocimetry. *Meas. Sci. Technol.*, 15:1–9, 2004.

[47] R. Herzog and K. Kunisch. Algorithms for pde-constrained optimization. *GAMM-Mitteilungen*, 33:163–176, 2010.

[48] F. Hettlich and W. Rundell. Recovery of the support of a source term in an elliptic differential equation. *Inverse Problems*, 13:959–976, 1997.

[49] F. Hettlich and W. Rundell. Identification of a discontinuous source in the heat equation. *Inverse Problems*, 17:1465–1482, 2001.

[50] M. Hinze and K. Kunisch. Second order methods for optimal control of time-dependent fluid flow. *SIAM J. Control Optim.*, 40:925–946, 2001.

[51] M. Hinze, R. Pinnau, M. Ulbrich, and S. Ulbrich. *Optimization with PDE Constraints*, volume 23 of *Mathematical Modelling: Theory and Applications*. Springer, 2009.

[52] L. Hou and T. Svobodny. Optimization problems for the Navier-Stokes equations with regular boundary control. *J. Math. Anal. Appl.*, 177:342–367, 1993.

[53] W. Huang and R. D. Russel. Moving mesh strategy based on a gradient flow equation for two-dimensional problems. *SIAM J. Sci. Comput.*, 20:998–1015, 1999.

[54] V. Isakov. *Inverse Problems for Partial Differential Equations*, volume 127 of *Applied Mathematical Sciences*. Springer, 1998.

[55] T. Kailath, A. H. Sayed, and B. Hassibi. *Linear estimation*. 2000.

[56] B. Kaltenbacher. Some newton-type methods for the regularization of nonlinear ill-posed problems. *Inverse Problems*, 13:729–753, 1997.

[57] P. M. Knupp and S. Steinberg. *The fundamentals of grid generation*. CRC Press, 1993.

[58] K. Kunisch and X. Pan. Estimation of interfaces from boundary measurements. *SIAM J. Control and Optimization*, 32:1643–1674, 1994.

[59] J. A. Liburdy and E. F. Young. Processing of three-dimensional particle tracking velocimetry data. *Optics and Lasers in Engrg.*, 17:209–227, 1992.

[60] J. L. Lions. *Optimal Control of Systems Governed by Partial Differential Equations*. Springer-Verlag, Berlin, 1971.

[61] I. Macedo and R. Castro. Learning divergence-free and curl-free vector fields with matrix-valued kernels. Technical report, Instituto Nacional de Matematica Pura e Aplicada, 2008.

[62] C. P. McNally. Divergence-free interpolation of vector fields from point values - exact div$b = 0$ in numerical simulations. *Mon. Not. R. Aston. Soc.*, 413:L76–L80, 2011.

[63] A. Meister. *Numerik linearer Gleichungssysteme*. Numerische Mathematik. Vieweg+Teubner, 2011.

[64] J. Modersitzki. *Numerical Methods for Image Registration*. Oxford Science Publications, 2004.

[65] J. Nocedal and S. J. Wright. *Numerical Optimization*. Springer Series in Operations Research. 2006.

[66] F. Ong, M. Uecker, U. Tariq, A. Hsiao, M. T. Alley, S. S. Vasanawala, and M. Lustig. Robust 4D flow denoising using divergence-free wavelet transform. *Magnetic Res. in Med.*, 73:828–842, 2015.

[67] F. Pereira, M. Gharib, D. Dabiri, and D. Modarress. Defocussing digital particle image velocimetry: a 3-component 3-dimensional DPIV measurement technique. Application to bubbly flows. *Exp. Fluids*, 29:78–84, 2000.

[68] O. Pironneau. *Optimal Shape Design for Elliptic Systems*. Springer series in computational physics. Springer-Verlag, 1984.

[69] W. K. Pratt. *Digiatal Image Processing*. John Wiley & Sons, Inc., 2001.

[70] W. Ring. Identification of a core from boundary data. *SIAM J. Appl. Math.*, 55:677–706, 1995.

[71] H. Rui and M. Tabata. A second order characteristic finite element scheme for convection-diffusion problems. *Numerische Mathematik*, 92:161–177, 2002.

[72] A. H. Sayed. *Adaptive Filters*. Wiley-IEEE Press, 2008.

[73] O. Scherzer, M. Grasmair, H. Grossauer, M. Haltmeier, and F. Lenzen. *Variational Methods in Imaging*, volume 167 of *Applied mathematical Sciences*. Springer-Verlag New York, 2009.

[74] D. Schiavazzi, F. Coletti, G. Iaccarino, and J. K. Eaton. A matching pursuit approach to solenoidal filtering of three-dimensional velocity measurements. *J. Comput. Phys.*, 263:206–221, 2014.

[75] J. A. Sethian. *Level Set Methods and Fast Marching Methods*, volume 3 of *Cambridge Monographs on Applied and Computational Mathematics*. 2008.

[76] J. Sokolowski and J.-P. Zolesio. *Introduction to Shape Optimization*, volume 16 of *Springer Series in Computational Mathematics*. 1992.

[77] J. Spurk and N. Aksel. *Strömungslehre*. Springer-Verlag, 2010.

[78] E. Süli. Convergence and nonlinear stability of the lagrange-galerkin method for the navier-stokes equations. *Numerische Mathematik*, 53:459–483, 1988.

[79] M. Tabata and S. Uchiumi. A genuinely stable lagrange–galerkin scheme for convection-diffusion problems. *Japan Journal of Industrial and Applied Mathematics*, 33:121–143, 2016.

[80] R. Temam. *Navier-Stokes equations. Theory and numerical analysis*, volume 2 of *Studies in Mathematics and its Applications*. North-Holland Publishing Co., Amsterdam, third edition, 1984.

[81] H. Tennekes and J. L. Lumley. *A first course in turbulence*. MIT press, 1976.

[82] A. N. Tikhonov. Solution of incorrectly formulated problems and the regularization method. *Soviet Math. Dokl.*, 5:1035–1038, 1963.

[83] F. Tröltzsch. *Optimale Steuerung partieller Differentialgleichungen*. Vieweg+Teubner, 2009.

[84] C. Tropea, A. L. Yarin, and J. F. Foss, editors. *Springer Handbook of Experimental Fluid Mechanics*. Springer, 2007.

[85] B. W. van Oudheusden. PIV-based pressure measurement. *Meas. Sci. Technol.*, 24, 2013.

[86] C. Y. Wang, Q. Gao, H. P. Wang, R. J. Wei, T. Li, and J. J. Wang. Divergence-free smoothing for volumetric PIV data. *Exp. Fluids*, 57:15, 2016.

[87] F. Wassermann and S. Grundmann. Flow visualization of a staggered pin fin array using magnetic resonance velocimetry. In *15th ERCOFTAC-SIG15/IAHR Workshop*, October 2011.

[88] K. Yosida. *Functional Analysis*, volume 123 of *Die Grundlehren der mathematischen Wissenschaften in Einzeldarstellungen*. Springer-Verlag Berlin Heidelberg New York, 1971.

CURRICULUM VITAE

Tobias Seitz
Born: September 21, 1988 in Bamberg, Germany

Academic positions

05/'14 – 10/'17	PHD STUDENT, IRTG 1529, TU Darmstadt
09/'14 – 09/'17	ASSOCIATE MEMBER, GSC CE, TU Darmstadt
09/'15 – 03/'16	RESEARCH STAY, Waseda University, Tokyo, Japan

Education

03/2014	M.SC. in Technomathematics, Universität Bayreuth
11/2011	B.SC. in Technomathematics, Universität Bayreuth

Publications

H. Egger, T. Seitz, and C. Tropea. *Enhancement of flow measurements using fluid-dynamic constraints*, J. Comp. Phys. 344 (2017), pp. 558–574.